UNIVERSITY OF OKLAHOMA

GRADUATE COLLEGE

A STUDY OF THE ELECTRICAL, MICROPHYSICAL, AND KINEMATIC

PROPERTIES OF THE 29 MAY 2012 KINGFISHER SUPERCELL

A THESIS

SUBMITTED TO THE GRADUATE FACULTY

in partial fulfillment of the requirements for the

Degree of

MASTER OF SCIENCE IN METEOROLOGY

By

ELIZABETH DIGANGI
Norman, Oklahoma
2014

A STUDY OF THE ELECTRICAL, MICROPHYSICAL, AND KINEMATIC
PROPERTIES OF THE 29 MAY 2012 KINGFISHER SUPERCELL

A THESIS APPROVED FOR THE
SCHOOL OF METEOROLOGY

BY

_____
Dr. Donald R. MacGorman, Chair

_____
Dr. Michael Biggerstaff

_____
Dr. Conrad Ziegler

_____
Dr. Alan Shapiro

_____
Dr. Susan Postawko

This thesis is dedicated to John and Kim DiGangi, the best siblings a person could have.

Acknowledgements

Table of Contents

List of Figures

Abstract

A supercell thunderstorm formed as part of a cluster of severe storms near Kingfisher, OK on 29 May 2012 during the Deep Convective Clouds & Chemistry (DC3) experiment. This storm produced 5" hail, an EF-1 tornado, and copious lightning over the course of a few hours. For part of the storm's lifetime, observations were obtained from mobile polarimetric radars and a balloon-borne electric field meter (EFM) and particle imager, while aircraft sampled the chemistry of the inflow and anvil. In addition, the storm was within the domain of the 3-dimensional Oklahoma Lightning Mapping Array (LMA), and the National Weather Service's KTLX WSR-88D radar.

This study focuses on a one-hour interval during which multi-Doppler coverage was available, and a balloon carrying an electric field meter (EFM), radiosonde, and particle imager flew through the storm. Data from KTLX are used to supplement mobile radar data. Flash rates, mapped very high frequency (VHF) source densities, and charge analyses are examined to give an overview of the storm's electrical nature and evolution during that period. The charge inferred from lightning is compared to the charge inferred from EFM measurements to test how well the lightning-inferred charge analysis can be expanded to the whole storm.

After an initial overview of the storm's lifetime and the environment in which the storm formed, the evolution of the flash size distribution as it relates to the kinematics and microphysics of the storm is examined at three analysis times spanning the approximately 40 minute period during which triple-Doppler data were acquired. Flash rates increased rapidly during this time. Lightning flash density, the horizontal

areas (i.e., footprints) of flashes, VHF source density, and the locations of flash initiations are then compared to storm microphysics and kinematics as observed by radar and retrieved by a diabatic Lagrangian analysis of the synthesized three-dimensional winds and reflectivity. The inferred charge structure of the storm and its evolution are also compared to these flash parameters and to the storm's microphysics and kinematics. When the storm matured, flashes in an around the updraft were typically small. Flash sizes tended to increase as distance from the updraft increased; as the storm strengthened, the overall size of flashes in the storm decreased.

Lightning flashes in the anvil, particularly those flashes that occurred several tens of kilometers from regions of deep convection, are also analyzed relative to radar reflectivity, ground strike points (provided by the National Lightning Detection Network), and inferred charge structure, to test hypotheses concerning how the flashes were initiated and why they propagated along certain paths. A region of convection strong enough to initiate lightning developed in the anvil during the analysis time and eventually propagated beyond the anvil. Its formation was consistent with being produced by evaporating virga falling from the anvil, as has been suggested previously.

Chapter 1: Introduction

The relationships between lightning and thunderstorm structure, microphysics, and kinematics have been a subject of intensive study for many decades. A number of mechanisms for storm electrification have been proposed in the past, and virtually all observational, modeling, and laboratory experiments seek evidence that one or all of the accepted theories is correct. Saunders (1993) reviewed the thunderstorm electrification processes believed to take place in convective storms as follows:

The convective mechanism involves a storm updraft drawing positive ions from beneath the cloud base into the cloud, where they are captured by water droplets and transported upward; then, negative ions are attracted downward from above the cloud and are captured by ice particles, forming a screening layer which descends via entrainment processes at the cloud tops. The creation of these two charge layers thus generates an electric field. The inductive charging mechanism relies initially on the ambient vertical electric field outside of a cloud inducing polarization charges in particles. When a smaller particle bounces off the lower surface of a larger particle, charge at the contact point is partially neutralized, thereby leaving each particle with a net charge of the polarity on the surface opposite to the contact point. Thus, the polarity of charge gained by each particle is opposite to that of the other. The noninductive charging mechanism involves particle collisions which allow charge transfers independent of local electric field strength; the most charge is transferred when ice crystals interact with graupel in the presence of supercooled water droplets.

For both the inductive and noninductive mechanisms, the smaller, less dense ice particles are then lofted above the graupel by the updraft, which creates large regions of

opposite charge adjacent to each other, thus generating an electric field. Since the noninductive mechanism has been shown to generate enough charge to electrify a thunderstorm on its own, the inductive mechanism is thought to act as a means of enhancing the electric fields originating from noninductive charging (MacGorman and Rust 1998). The polarity of charge layers generated by noninductive charging and by the subsequent macroscopic charge separation in the updraft depends on the supercooled water content present and the temperature of the region in which rebounding particle collisions occur (e.g., Takahashi et al. 1978; Bruning et al. 2010), though the details of how exactly these properties affect the charge polarity generated are still uncertain (e.g. Takahashi and Miyawaki 2002; Saunders et al. 2006).

The general charge structure of a thunderstorm was first thought to be a dipole, with a lower negative charge layer and an upper positive charge layer, based on early measurements of electric fields from the ground (e.g. Wilson 1916, 1925). Subsequent studies based on in-situ measurements later showed that a second positive charge region is typically beneath the negative region, and thus that thunderstorms generally have a tripole charge structure (e.g. Simpson and Scrace 1937; Simpson and Robinson 1941; Williams 1989). As charge is generated microscopically and separated macroscopically, electric fields form, and are strongest between the charge regions.

If the electric field reaches the dialectric breakdown threshold, then flash initiation will occur (MacGorman and Rust 1998). From the initiation point, stepped leaders branch out into the different charge regions (Kasemir 1960; Mazur 1989; MacGorman and Rust 1998); a negatively charged leader traverses the positive charge, and a positively charged leader traverses the negative charge. This process dissipates

the charge regions that caused the dielectric breakdown to begin with (MacGorman et al. 1981), and the storm may have to recharge before another lightning flash can occur. If breakdown and flash initiation occurs between the lowest layer of charge and the central layer of charge in the tripole paradigm, the flash can be either a cloud flash or a cloud-to-ground flash. Typically, a flash will continue to ground (i.e., will be a cloud-to-ground (CG) flash) if the negatively charged leader propagating downward toward the lower positive charge reaches too little charge to balance the charge the positive leader taps in the negative region (Kasemir 1960; Mazur 1989; Rison et al. 1999). Many investigators have confirmed this conceptual model of lightning, suggesting that the lower charge region is not a sufficient condition, but is a necessary condition, for initiating CG flashes in many situations (e.g. Weins et al. 2005; Kuhlmann et al. 2006; Tessendorf et al. 2007a).

Warm-season storms in many regions of the United States typically take 5-10 minutes from the onset of lightning to produce CG lightning. MacGorman et al. (2011) found that, in Oklahoma and north Texas, 50% of storms from May-August 2005 produced a CG flash within 5-10 minutes of the onset of lightning, but only 10% failed to produce one within the first hour of lightning activity in a storm, and that these percentages varied across the United States. In the High Plains, for example, it took 30 minutes to reach the 50% threshold and only 80% of storms produced a CG flash within 1 hour. They attributed the longer elapsed times on the High Plains to the tendency for the electrical structure of these storms to have inverted vertical polarity (e.g., storms with a central positive charge layer and upper and lower negative charge layers in the tripole model) and for their CG lightning flashes to deposit positive charge at the

ground instead of the usual negative charge (Rust and MacGorman 2002; Lang et al. 2004; MacGorman et al. 2005; Weins et al. 2005).

The first attempts to map in-cloud lightning in three dimensions made use of the acoustics of thunder. For example, MacGorman et al. (1981) showed with acoustic reconstructions of lightning that lightning propagated predominantly in horizontal layers at altitudes above the freezing level. Subsequent strides made in the field of lightning detection, such as the advent of ground-based very high frequency (VHF) radiation mapping systems (e.g. Lightning Mapping Arrays, Thomas et al. 2004), enabled much more detailed analyses of lightning discharges. Additionally, field experiments that include flying balloon-borne electric field meters through various sections of thunderstorms have shed great insight into the complex charge structures of thunderstorms (e.g., The Severe Thunderstorm Electrification and Precipitation Study (STEPS), Lang et al. 2004; The Thunderstorm Electrification and Lightning Experiment (TELEX), MacGorman et al. 2008). Total lightning measurements reveal that, typically, thunderstorms produce considerably more IC lightning than CG lightning (e.g., Boccippio et al. 2001, MacGorman et al. 2011).

Marshall et al. (1989) and Marshall and Rust (1991), among others, have pointed out the various shortcomings of the tripole paradigm for thunderstorm charge structure. Several studies (e.g. Marshall and Rust 1991; Stolzenburg et al. 1998; Weins et al. 2005; Weiss et al. 2008; Bruning et al. 2010) have shown that many storms, particularly supercells, have much more complex charge structures than that of the tripole paradigm. To better illustrate the truly complex nature of thunderstorm charge structures, Stolzenburg et al. (1998) synthesized the data from almost 50 electric field
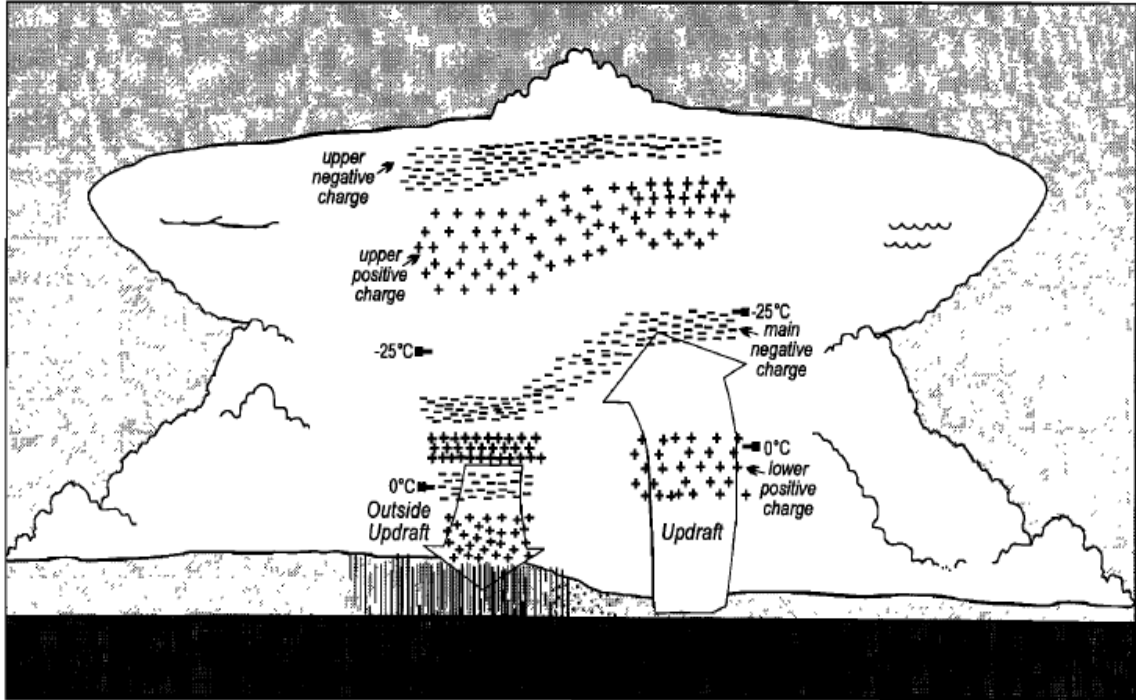
Figure 1. Model of charge distribution in a supercell thunderstorm. From Stolzenburg et al. (1998).

soundings through convection of various modes and found that convective storms have

an average of four charge layers within the updraft and at least six outside of it, with the

lowest in both regions being positive; this model is shown in Figure 1. For supercell

updrafts, the height of the center of the main negative charge region is approximately

9.12 km (-22°C), and a stronger updraft typically means the altitude of the center of this

mid-level charge region tends to be higher. MacGorman et al. (2005) found that charge

structures in supercell updrafts were consistent with the noninductive charging

mechanism dominating the electrification of two storms observed during STEPS. They

concluded that inductive charging mechanisms and charge deposition by lightning were

responsible for the generation of extra charge layers outside the updraft in the low

levels, and hypothesized that the inverted-polarity charge structure of the observed

storms could be due to a larger than usual graupel rime accretion rate in the presence of

a strong updraft. Related to the issues of the tripole paradigm, Bruning et al. (2012) noted that the terms "normal" and "inverted" charge structure are only adequate to describe the distribution of charge in a thunderstorm in the most basic sense, and that those terms do not demonstrate charge structure complexity any better than the tripole paradigm.

Another prominent theme in lightning research is to determine where and when lightning occurs relative to storm kinematics, microphysics, and dynamics, and the most common method of drawing conclusions about these relationships is by comparing lightning data with radar data. For example, Ray et al. (1987) found that, for a supercell thunderstorm, lightning tends to occur above and downshear of reflectivity cores, and that VHF source points tend to be concentrated in regions of 30-40 dBZ while being uniformly distributed with respect to updraft speed. They concluded that the location of lightning is most directly determined by the wind field relative to reflectivity and updraft cores. Wiens et al. (2005) investigated the lightning and charge structure of the 29 June 2000 supercell observed during STEPS and found (1) that almost 90% of CG flashes lowered positive charge (+CGs) to ground and (2) that the charge structure during the storm's mature phase was roughly an inverted tripole. They found that +CG occurrence was linked with surges in updraft strength, hail production, and total flash rate, and that all CGs tended to strike in or immediately adjacent to the storm's precipitation core. Weiss et al. (2008) found that, for a multicell storm sampled during STEPS, the cells with the most complex charge and lightning structures were the cells with the highest reflectivity and the deepest reflectivity cores. As the vertical extent and maximum reflectivity values of cores decreased, so did the IC flash rates.

Studies have also found that kinematic features may affect the characteristics of flashes associated with them. For example, Calhoun et al. (2013) found that flashes near the core of the 29-30 May 2004 Geary supercell storm during TELEX tended to be frequent but small in horizontal extent and of short duration, while flashes closer to the edges of the storm were less frequent but tended to be much larger, sometimes propagating far into the anvil in roughly horizontal layers. They hypothesized that the charge regions in the storm core consisted of small pockets of charge rather than the broad layers of charge found in the anvil. The storm had extremely high flash rates, which were the result of a consistently strong updraft and large concentrations of hydrometeors. The strong and large updraft also contributed to the development of a lightning hole and discharges in the overshooting top. To investigate the relationship between flash rate and flash size more quantitatively, Bruning and MacGorman (2013) analyzed gridded flash variables derived from LMA data, including mean flash area, flash extent density, and flash origin (or initiation) density. They found that the mean flash area tended to be larger in regions in which flash origin density was smaller and vice versa. By developing a non-dimensional parameter involving the energy dissipated by a flash and the horizontal area of the flash, they showed that flashes occurring over 10-minute periods had a 5/3 dependence on linear extent similar to the dependence of turbulent spectra and so suggested that the inverse relationship between size and flash rate was related to the energetics of turbulence.

Comparing flash behavior with cloud microphysics has become more feasible with the availability of polarimetric radar data. For example, Lund et al. (2009) found that, for multiple cells embedded within a mesoscale convective system (MCS)

observed during TELEX, lightning was initiated in or near regions containing graupel.

One region of lightning initiations (between 7-10 km AGL) was situated above a region

of inferred graupel and below a region of inferred ice crystals. Another region of

lightning initiations (between 3-6 km AGL) was in the upper part of the melting layer,

near a region of graupel production (as inferred from the presence of a ZDR column).

These findings are consistent with the microphysics of the noninductive charging

mechanism. Bruning et al. (2007) analyzed a multicell storm with a complex charge

structure from the TELEX campaign, and noted that a leader from the storm's first flash

avoided a region containing wet hail growth (as inferred from polarimetric radar data),

since wet hail is not conducive to hydrometeor charging. Additionally, the time varying

flash initiation points for flashes that propagated into the upper positive charge layer of

the storm tracked the descent of a polarimetric graupel signature. Emersic et al. (2010)

also observed that, for a hail-producing storm, total flash rates increased during surges

in updraft strength except when wet hail growth occurred in the updraft, at which time

total flash rates decreased instead. They suggested that, by inhibiting rebounding, wet

hail growth processes contributed to the development of a lightning hole, or a localized

region of low lightning density, in the absence of a mesocyclone. The charge structure

of the observed storm was initially termed a standard tripole, but reversed to an inverted

tripole during the same updraft surge associated with a decrease in flash rates and wet

hail growth, and so attributed the inverted polarity structure to the large amounts of

liquid water content in updraft regions. Concurrent with the formation and later

intensification of the storm's updraft and growth of the overshooting top, they also

observed episodes of continual VHF sources between 13-15 km that were not associated with typical flashes.

A strong motivation for improving understanding of the microphysics, kinematics, and dynamics of storms as they relate to lightning is to develop applications of lightning to forecasting operations. Specifically, there have been many investigations into the connections between thunderstorm intensification and flash rates, as well as changes in lightning activity preceding severe weather events (e.g. tornadoes and hail). It has been shown that, in general, total lightning activity is more correlated to storm intensity and severe weather events than CG lightning activity alone (e.g., Steiger et al. 2007). The majority of such studies are case studies, or multi-case studies. For example, Carey and Rutledge (1996) discovered a strong correlation between updraft graupel volume and the IC lightning flash rate in a multicell storm, and between maxima in the hail rate and maxima in the CG flash rate, which are both consistent with the noninductive charging mechanism.

More recently, researchers have statistically analyzed total lightning in large numbers of storms to try to develop algorithms using lightning characteristics to create automated guidance for forecasters. In a study of 711 storms form various regions of the United States, Schultz et al. (2011) showed that jumps in total flash rates usually preceded severe weather and could be used to improve warnings of severe weather events. Herzog (2013) performed a statistical analysis of 5 years of nationwide thunderstorm data using the Warning Decision Support System - Integrated Information (WDSS-II) platform in order to examine relationships between a wide array of radar-derived and lightning attributes for different regions and different storm types in an

9

attempt to find markers capable of distinguishing between hazardous versus non-hazardous weather, and to find relationships between the lightning and radar attributes. They concluded that, in general, hazardous (severe or supercell) thunderstorms produced substantially more lightning than non-hazardous storms. Additionally, they found that most radar attributes had a moderate to strong correlation with lightning attributes, and that these radar attributes (e.g. maximum reflectivity at -20°C and 40 dBZ echo tops) could be estimated using probability distributions based on the lightning attributes, thus providing forecasters with a proxy for radar data between radar volume scans.

Lightning that occurs in anvils has been of particular concern, both because of its implications to understanding of electrification processes and because it poses a hazard to life and property tens of kilometers from deep convection. Most flashes that have been observed in anvils were initiated in or near deep convection and propagated up to 30 km into anvils, as observed, for example, by Dye and Willett (2007) and Tessendorf et al. (2007b). From their aircraft measurements, Dye and Willett (2007) noted that charge and strong electric fields decayed more slowly than would be expected for isolated particles. They speculated that the observed range of ice particle sizes would allow ice-ice particle collisions to generate additional charge within the anvil, especially if combined with strong (> 10 kV m^{-1}) preexisting electric field.

In addition to lightning propagating into anvils from deep convection, recent studies have found that lightning can be initiated in anvils up to 100 km from the nearest 30 dBZ contour and can propagate back toward storm cores. Kuhlman et al. (2009), the first to report this phenomenon, observed that such flashes were initiated at

or near the boundary between the anvils of two adjoining supercell storms. Like Dye and Willett, they suggested that the presence of lightning many tens of kilometers from strong updrafts meant that a charging mechanism within the anvil itself was contributing charge. They noted that the two anvils had opposite polarities of charge at the same altitude and suggested that this created electric fields strong enough to initiate some of the observed anvil flashes. However, some flashes were initiated later, after the northern anvil no longer contained lightning, so they suggested that charge was produced within anvils in much the same way it is produced in the stratiform regions of mesoscale convective systems.

In extending this work, Weiss et al. (2012) found that anvil flashes could be initiated in more than one scenario: in or near a local reflectivity maximum, between the a screening layer charge and a charge layer within the anvil, or in a region in which there are anvil interaction between adjacent storms. The reflectivity maxima associated with initiations often had tendrils extending downward below the 0°C isotherm and produced ground flashes that struck ground below the local maxima far out in the anvil. Weiss et al. suggested that the lightning initiations associated with tendrils of reflectivity maxima extending below the melting level indicated the development of convection by a mechanism in anvils suggested by Knight et al. (2004). Knight et al. noted that convection could be initiated by the generation of local instability as ice particles fall below the 0°C isotherm, melt, and thus cool and moisten the air via evaporation. The weak updrafts generated this way are thought to generate supercooled cloud water and graupel within the anvil. However, in order for the instability generated by evaporative cooling to overcome the downward momentum of that descending

cooled air, Weiss et al. (2012) noted that these processes must take place in a region of preexisting weak updraft.

The improved understanding of electrification mechanisms and lightning have led to the development of numerical cloud models that incorporate electrification and lightning parameterizations to study relationships with other storm parameters in more detail. MacGorman et al. (2001) and Mansell et al. (2002, hereafter referred to as "M02") developed lightning parameterizations with various thresholds for the electric field magnitude required for flash initiation. In both parameterizations, flashes continue propagating into regions in which the electric field magnitude is small, as long as either the potential difference or the field due to the channel itself is large enough. Simulations performed with these parameterizations produce flash structures similar to those of observed flashes. However, the M02 parameterization is based on a branched-channel discrete breakdown model and thus produces much more detailed lightning structure. Several studies have used one of these parameterizations. For example, Kuhlman et al. (2006) used the M02 parameterization to model electrification and lightning in the 29 June 2001 STEPS supercell and found that the total flash rate was well correlated with updraft volume, updraft mass flux, and graupel volume, though the maximum updraft speed was not correlated with flash rate. They concluded that the lightning parameter that best represents storm intensity is total flash rate.

1.1 Research Goals

This study investigates a supercell storm observed on 29 May 2012 during the Deep Convective Clouds and Chemistry experiment (DC3), a collaborative field research program carried out by several organizations and federal agencies. DC3 took place from

15 May - 30 June 2012 in thee domains: northern Alabama, central-southwest Oklahoma and northwest Texas, and eastern Colorado. The principal motivation for DC3 was to investigate the impact of deep midlatitude convection, including dynamic, microphysical, and lightning processes on the chemistry of the upper troposphere, the evolution of upper tropospheric chemistry for 24-48 hours after storms, and the processes affecting lightning characteristics. Storms from each domain were sampled by instrumented aircraft and ground support crews.

This study investigates several aspects of the 29 May 2012 Kingfisher supercell storm observed during the Deep Convective Clouds and Chemistry experiment:

1. We will examine the trends in total and CG lightning as they relate to each other and to other storm parameters, such as updraft intensity (where available) and severe storm reports over the course of the storm lifetime.

2. For three times during which triple-Doppler data and some in-situ electric field data were available, we will analyze the storm's kinematic, microphysical, and electrical characteristics (including charge structure) in detail.

3. We will analyze how anvil lightning relates to the electrical characteristics of the storm's anvil and to the development of secondary convection within the anvil.

All of these analyses will be performed with the intent of discovering or confirming relationships between various electrical, kinematic, and microphysical storm characteristics.

Chapter 2: Data and Methods

Several datasets were used in our analysis of the 29 May Kingfisher supercell: total lightning, cloud-to-ground lightning, mobile radar, NEXRAD radar, in-situ and environmental soundings, and storm reports. Total lightning data were supplied by the Oklahoma Lightning Mapping Array (OK LMA), as the storm was in the three-dimensional LMA range for its entire lifetime. Cloud-to-ground lightning data were supplied by the National Lightning Detection Network (NLDN) operated by Vaisala (e.g., Cummins and Murphy 2009). One X-band and two C-band mobile radars sampled the Kingfisher supercell as a part of DC3 operations and provided triple-Doppler coverage of the Kingfisher storm for a portion of its lifetime. Data from KTLX, the Oklahoma City Next Generation Radar (NEXRAD) radar, were used to supplement the mobile radar data. For microphysical analysis, the triple-Doppler analyses and environmental soundings were used to run a diabatic Lagrangian analysis (DLA, Ziegler 2013a, 2013b), which calculates water vapor and hydrometeor mixing ratios, potential temperature, and several other parameters throughout the analysis grid. Ground support crews for DC3 launched environmental soundings as well as in-situ soundings. The latter bore electric field meters and particle imagers in addition to radiosondes. Storm reports were used to compare lightning characteristics to documented severe weather events (e.g., hail and tornadoes) associated with the Kingfisher storm. This section will discuss each of these datasets, as well as the processing and analysis procedures used for each.

2.1 Lightning analysis

The primary source of lightning data was the OK LMA, although NLDN data were used to supplement the LMA data to identify which flashes struck ground in the anvil. The LMA is a network of ground-based sensors which detect very high frequency (VHF) emissions from lightning channels. Each emission is referred to as a VHF source. Within the range of the 3D-LMA (roughly 120 km from the center of the network), the sensors can determine the location of a VHF source in three physical dimensions (longitude, latitude, and altitude) and in time. Within the range of the 2D-LMA (roughly 200 km from the center of the network), the sensors can detect the time and plan location at which a VHF source was radiated. This results in detailed mapping of individual flashes, which can be used to analyze a storm's electrical structure and development. These data are referred to as total lightning data, because the VHF sources mapped by the LMA are for all of the lightning occurring in a storm or storm system, not just for cloud-to-ground lightning. The LMA locates VHF sources with an uncertainty of 6-12 m in the horizontal and 20-30 m in the vertical, within the perimeter of the network. The associated uncertainty in arrival time measurements is 40-50 ns RMS (Thomas et al. 2004).

NLDN data were obtained for the whole Oklahoma-Texas domain. The date, time, latitude, longitude, location error, estimated peak current, polarity, and number of return strokes for each flash are supplied. The network has an overall detection efficiency > 95% and event timing precision of 1 microsecond (Vaisala 2014).

To restrict our analysis to the subject storm, polygon boxes bounding the storm were used to eliminate as many flashes from surrounding storms as possible. The boxes

for the storm during each radar volume scan were determined from the position of the storm depicted by KTLX low-level reflectivity data. After 00:00 UTC, the storm became increasingly difficult to isolate, as it was part of a complex of multiple storms and fully merged with one of them, so there is some overlap with the edges of nearby cells, but the resulting uncertainties were too small to affect the direction of trends in flash rates.

LMA data were processed and analyzed within three software platforms for this case: XLMA, Warning Decision Software System: Integrated Information (WDSS-II, Lakshmanan et al. 2007), and an lmatools package (Bruning and MacGorman 2013). XLMA was developed by researchers at New Mexico Tech for the purpose of viewing, processing, and analyzing LMA data. WDSS-II was developed by scientists at the National Severe Storms Laboratory (NSSL) and the Cooperative Institute for Mesoscale Meteorological Studies (CIMMS) to allow researchers and National Weather Service forecasters to view various types of data, in real-time or otherwise. When efforts to include total lightning in nowcasting and forecasting began, algorithms were developed to ingest LMA data into WDSS-II and to generate various lightning products for analysis, including flash initiation points and total lightning density. The lmatools program package was developed by Eric Bruning to calculate various flash statistics (e.g., flash rates, flash density, and average flash area) after gridding the data.

For the 29 May case, the 10-minute LMA data files were first loaded into XLMA, and noise points were eliminated by excluding anything detected by fewer than seven stations or with a χ^2 value greater than 2. Sources detected above 20 km in altitude were eliminated in preprocessing, because they were at least a few kilometers above the

16

maximum storm height detected by radar. To isolate the cell of interest within each file, a polygon was drawn manually around it in XLMA, and data outside the polygon were deleted. Though necessary for the sake of obtaining a quantitative flash count for the storm, trimming could introduce errors in flash counts because of its effect on automatic criteria for identifying flashes when the flashes propagated between storms. The trimming could introduce errors, either by cutting flashes in two or by incorrectly reducing the number of VHF sources below the criteria for acceptance as a flash. However, a very small percentage of flashes in the subject storm would be affected during most of the period. It may have had a larger, though still small, effect as two storms merged toward the end of the analyzed period, but as the merged storm approached, it was quickly included in the flash counts for the subject storm. Note that the flashes used for gridded flash statistics, described below, were calculated from all VHF sources, before unwanted grids were trimmed, so errors were not introduced in the gridded flash statistics by the trimming.

Once unwanted sources from noise and other storms were eliminated, the data were ingested into WDSS-II with the w2lma_ingest algorithm, which could superimpose total lightning data for one-minute periods on WSR-88D data. This algorithm also converts the space-delimited LMA text files into tabular data for use in other lightning algorithms (Herzog 2013). The second algorithm implemented was w2lmaflash, which sorts VHF sources into flashes and then calculates initiation points and other flash parameters. To be considered a flash for these algorithms, it had to consist of at least 10 sources, and each added VHF source had to be within 3km and 150ms of a previous source (MacGorman et al. 2008). There is no upper limit on the

number of sources in a flash, although all sequential sources in a flash must satisfy the time and space constraints. The flash initiations are calculated, as done by Lund et al. (2009), as the centroid of at least five VHF sources among the first 10 sources that that had a standard deviation of no more than 0.5km about the centroid.

To calculate flash density and flash area, the program package known as lmatools was utilized. The lmatools program sorts VHF sources into flashes using the same criteria as the w2lmaflash algorithm, but also requires flashes to have a horizontal dimension of at least 0.15 km. The package then derives four flash parameters and maps them onto a 2-D grid:

1. flash density, which is the number of flashes that pass through a grid column (this parameter is called flash extent density in much of the recent lightning literature, such as Herzog (2013) and Stano et al. (2014), but use of the term "flash density" avoids potential confusion with flash area, which is also calculated);

2. flash initiation density, which is the number of flash initiations in a grid column;

3. flash footprint, which is the average horizontal area of the flashes passing through a grid column, where the horizontal area, also called the footprint, being calculated for each flash is the horizontal convex hull that encompasses all the flash's VHF sources (Bruning and Macgorman 2013);

4. VHF source density, which is the number of VHF source points in a grid column.

Note that, for the flash parameters defined above, a flash was counted only once per grid column, no matter how many of the flash's VHF sources occurred in that column

The grid used with lmatools was the same as used by the triple-Doppler radar synthesis and by the DLA (sections 2.2 and 2.3, respectively), so that the results of

lmatools could be overlaid on the radar and Lagrangian analyses. The radar grid, in turn, was confined to the best region of triple-Doppler coverage. As noted above, all data in the LMA domain were processed by lmatools, and then the grid boundaries were set to exclude all results from lmatools outside the radar analysis region. These boundaries included parts of the cell to the north of the Kingfisher storm and excluded most of the anvil region.

The analysis of gridded lightning data used a 500m x 500m horizontal grid at 23:21, 23:39, and 00:00 UTC, three times that spanned intensification of the supercell storm during the period for which triple-Doppler and Lagrangian analyses were performed. Though the gridded lightning statistics were on a two-dimensional grid and so do not show vertical variability, they can still be overlaid with parameters from the radar and Lagrangian analyses for various altitudes. Each time in the gridded analysis computed parameters from 10 minutes of lightning data centered on the analysis time (+/- 5 min). A period of 6 minutes was tested, but trends in the data were clearer in 10 minute intervals. The flash density, flash footprint, and LMA source density grids were smoothed by replacing the value of each grid cell with the arithmetic average of that cell and the 8 cells surrounding it. During the smoothing process, if the grid cell for which the average was being calculated did not contain any VHF sources, it was skipped; this constraint prevented the smoothing code from spreading data into grid cells where there were no data.

Analysis of the storm's charge structure was performed by examining the temporal development and evolving source density for each flash. This is possible because negative leaders propagate more impulsively than positive leaders, and thus

produce many more VHF sources than positive leaders produce (Rison et al. 1999, Bruning et al. 2010). Negative (positive) leaders tend to spread outward through regions of positive (negative) charge (MacGorman et al. 1981, 2001), so where a negative (positive) leader is detected in the LMA data, a region of positive (negative) charge is inferred. A lightning channel propagating through negative charge typically produces a much smaller density of VHF sources (at least when detected by LMAs with station baselines >10 km), and often the sources detected in negative charge are produced by recoil leaders propagating from its outermost extremity back down the channel toward positive charge. This charge analysis was compared with the charge densities calculated as described by MacGorman and Rust (1998) from the vertical electric field measured by an in-storm balloon sounding that flew between 23:23 UTC and 23:57 UTC.

2.2 Radar analysis

The KTLX operational Weather Surveillance Radar 88 Doppler (WSR-88D, Crum and Alberty 1993) near Oklahoma City, OK provided long-period observations of the evolving 29 May Kingfisher supercell. At that time, KTLX had not yet received its scheduled dual-polarimetric upgrade, so only reflectivity and velocity data were available for analysis. Since KTLX transmits at S-band wavelength (approximately 10 cm), attenuation is not an issue for this storm. The KTLX data analyzed in this study are from a real-time dataset that was used during the 2012 Hazardous Weather Testbed (HWT) as displayed on the WDSS-II (Lakshmanan et al. 2007) platform (Kristen Calhoun, personal communication, 2014). Because of the real-time nature of the data

and the availability of better horizontal and vertical wind retrievals from the mobile Doppler analysis (described below), only reflectivity data from KTLX were used.

Three mobile ground-based radars were deployed on 29 May 2012, namely the two Shared Mobile Atmospheric Research & Teaching Radars (SMART-Rs, SR1 and SR2, Biggerstaff et al. 2005) and the NOAA X-Pol Radar (NOXP). Both SMART-Rs transmit at C-band wavelength (approximately 5 cm), and SR2 is dual-polarimetric. NOXP transmits at X-band wavelength (approximately 3 cm) and is also dual-polarimetric. Processing of polarimetric data was not completed in time for use in this study, although the diabatic Lagrangian analysis (described in section 2.3) provides unique estimates of cloud and precipitation particle concentrations and mixing ratios that are not obtainable directly from polarimetric radar using present analysis methods. Results from polarimetric data analyses will be included in future work with this case and with other DC3 cases.

Each of the three mobile radars completed a synchronized full volume scan every three minutes. The mobile radar data were edited using the SOLOII software (Oye et al. 1995) to eliminate noise, ground targets, second-trip echoes, range-folding, and velocity aliasing. Because these radars transmit at smaller wavelengths than the WSR-88Ds, rain attenuates their signals more strongly than it attenuates signals from WSR-88Ds. Thus, an attenuation correction scheme was applied as an additional essential radar editing step. The SMART-Rs have a higher Nyquist velocity than the NOXP, while NOXP has more signal attenuation and higher spatial resolution than the SMART-Rs due to its smaller wavelength (Biggerstaff et al. 2005). Applying the same attenuation correction scheme (ZPHI, e.g. Testud et al. 2000) to the data from all three

21

radars using the appropriate parameters for each radar wavelength improves the multi-Doppler reflectivity analyses.

The three sets of edited mobile radar data were each spatially interpolated to the radar analysis grid via a 2-pass Barnes interpolation (Majcen et al. 2008) that was optimized with a 2 km smoothing parameter to suppress poorly-resolved short-wavelength spatial variations. The 3-D winds were retrieved via a variational analysis that employed a weak anelastic mass continuity constraint (e.g., Sasaki 1970; Potvin et al. 2012) and a weak environmental sounding constraint (Daniel Betten, personal communication, 2014) that simultaneously imposed a smooth transition between the outer edge of the triple-Doppler wind analysis fields and the horizontal wind profile obtained from a storm-following sounding that was assumed to represent the storm's far environment. The earliest wind analysis at 2251 UTC was dual-Doppler (i.e., combining SR2 and NOXP observations), while analyses after 2300 UTC were triple-Doppler. Since the storm was far to the east of NOXP and SR2 and since SR1 stopped scanning at 0003 UTC, the last triple-Doppler wind analysis in the continuous 3-min interval time sequence was at 0000 UTC. Due to the storm's movement to the eastern edge of the triple-Doppler radar array, there is a small volume of possibly anomalous updrafts near the location of SR1 after 2351 UTC. The wind and reflectivity synthesis was performed within a fixed (ground-relative) 90 km x 60 km x 17 km grid domain with a 0.5 km x 0.5 km x 0.5 km grid spacing and vertical grid levels located between 0.20 km and 17.2 km AGL.

2.3 Diabatic Lagrangian analysis

A diabatic Lagrangian analysis (DLA) has been applied to the 29 May storm to recover the 3-D fields of potential temperature and mixing ratios of water vapor, cloud liquid water, and cloud ice and small snow crystals employing diagnosed rain and graupel/hail mixing ratio fields (Ziegler 2013a,b). The recent addition of cloud ice/snow to the DLA follows the general DLA microphysics algorithm (Conrad Ziegler, personal communication, 2014), wherein the new DLA ice processes follow Mansell et al. (2010). The DLA algorithm ingests multiple-Doppler radar-derived 3-D reflectivity and vector wind analyses. In brief, the analyzed reflectivity field is used to diagnose the rain and graupel/hail mixing ratios. The DLA is predicated on the integration of a set of predictive ordinary differential equations to calculate the time-varying Lagrangian temperature and non-precipitating water substance variables along ground-relative air trajectories that are calculated from the time-dependent 3-D wind fields. The four-dimensional vector airflow field from the multi-Doppler analysis (described in section 2.2) is modified slightly so that it satisfies a strong anelastic continuity constraint (e.g., Sasaki 1970; Ray et al. 1978).

The implementation steps of the DLA algorithm are described in more detail in the following discussion. The algorithm first calculates the field of time-dependent upstream parcel trajectories from the DLA gridpoints that each extend backward in time into the storm's inflow environment. At each parcel's initialization point, environmental sounding data are vertically interpolated to determine the potential temperature θ (K), the water vapor mixing ratio q_v (g kg^{-1}), and the ambient pressure (mb) for each parcel. The algorithm then integrates a system of first-order ordinary differential equations

23

forward in time along each trajectory from the Lagrangian initial conditions set at each parcel initiation point in the domain (Ziegler 2013a). The algorithm interpolates the reflectivity to each Lagrangian point during integration and calculates the time-varying Lagrangian values of rain water mixing ratio q_r (g kg^{-1}) and graupel/hail mixing ratio q_g (g kg^{-1}) for subsequent microphysical and thermodynamic Lagrangian calculations. The predicted Lagrangian variables are θ and q_v as well as the cloud water mixing ratio q_c (g kg^{-1}) and the cloud ice mixing ratio q_x (g kg^{-1}). Note that small rain water contents diagnosed above the -20°C level in updrafts (~ 7.20 km) or above the melting level in weak updrafts or downdrafts were negligible and thus ignored during analysis, while significant supercooled liquid cloud mixing ratios are analyzed through the -40°C level in the storm. In addition to the above parameters, an optional diagnostic algorithm may be employed to calculate additional quantities such as the instantaneous rain rate (mm hr^{-1}) and the air parcel origin height (km), though the latter parameters were not used in this study. Additional details describing how the algorithm was tested using an observing system simulation experiment (OSSE) with simulated storm data are given by Ziegler (2013a), while details describing its application with radar-observed wind and reflectivities are given by Ziegler (2013b).

The DLA is effected within a sub-domain of the volume containing the input radar analysis and also shares the same grid mesh (i.e., including identical grid point locations) as the radar analysis. The fixed (ground-relative) coordinate limits of the DLA sub-domain (i.e., x_{min}, x_{max}, y_{min}, y_{max}, z_{min}, z_{max}, with units of kilometer) with respect to the parent radar analysis grid are (15, 85, 5, 50, 0.2, 17.2). Synthetic 3-min input radar analyses were added during the period 2230-2248 by advecting the 2251

24

UTC storm analysis fields backward in time with assumed steadiness following the observed storm motion (Ziegler 2013b). This slight augmentation of the radar analysis time series assisted a few upstream trajectories that originated in the downstream anvil outflow in reaching their low-level storm inflow environment.

2.4 Storm reports

Reports of hail and tornadoes were obtained from the StormData dataset through the National Climactic Data Center (NCDC). There are inherent inaccuracies in these data because they are obtained from the general public. However, StormData is the most comprehensive and accessible source of data on the occurrence of hail and tornadoes (Herzog 2013), so we analyze the timing of the severe weather reported in this storm relative to trends in lightning characteristics over the course of the storm's lifetime.

Chapter 3: Results and Discussion

3.1 Storm overview

A dryline formed in western Oklahoma (OK) on 29 May 2012 (Fig. 2a).

Diffluence at 500 mb over OK increased throughout the day (Figs. 3a-b). By 21:00

UTC (4:00 pm CDT), several convective towers had formed ahead of the dryline bulge

(Fig. 2b) and were targeted for sampling by DC3 scientists. An environmental sounding

was launched in north-central OK, near but outside most influence of the convection, at
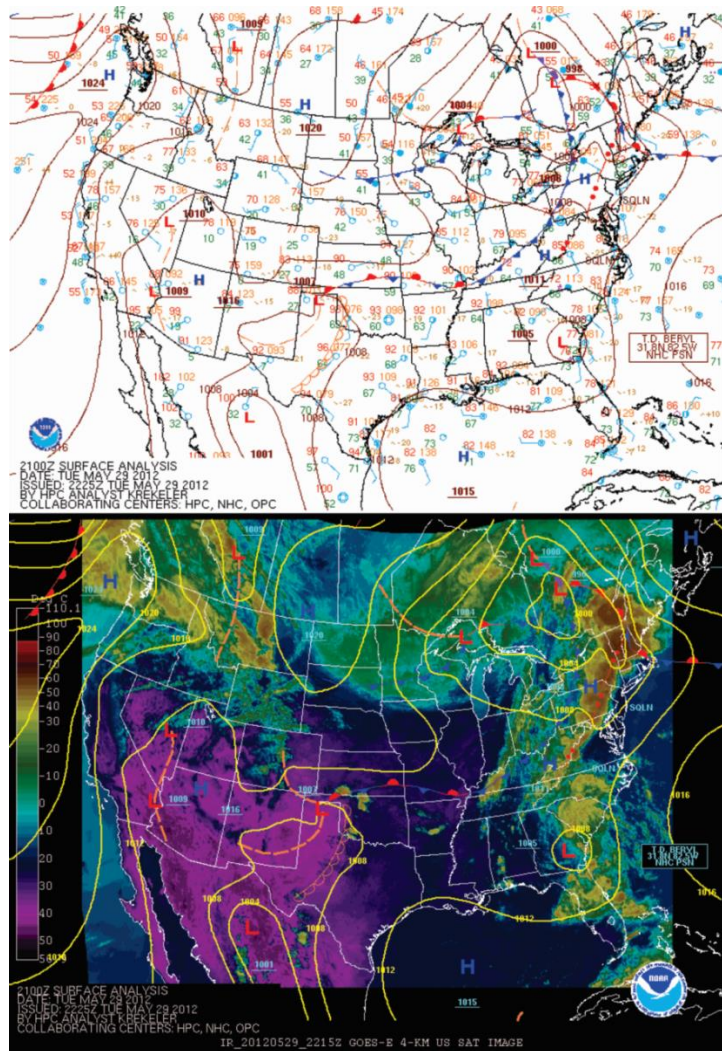
Figure 2. Surface analyses from the Hydrometeorological Prediction Center (HPC) archive, with overlaid a) ground observations and b) infrared satellite imagery.
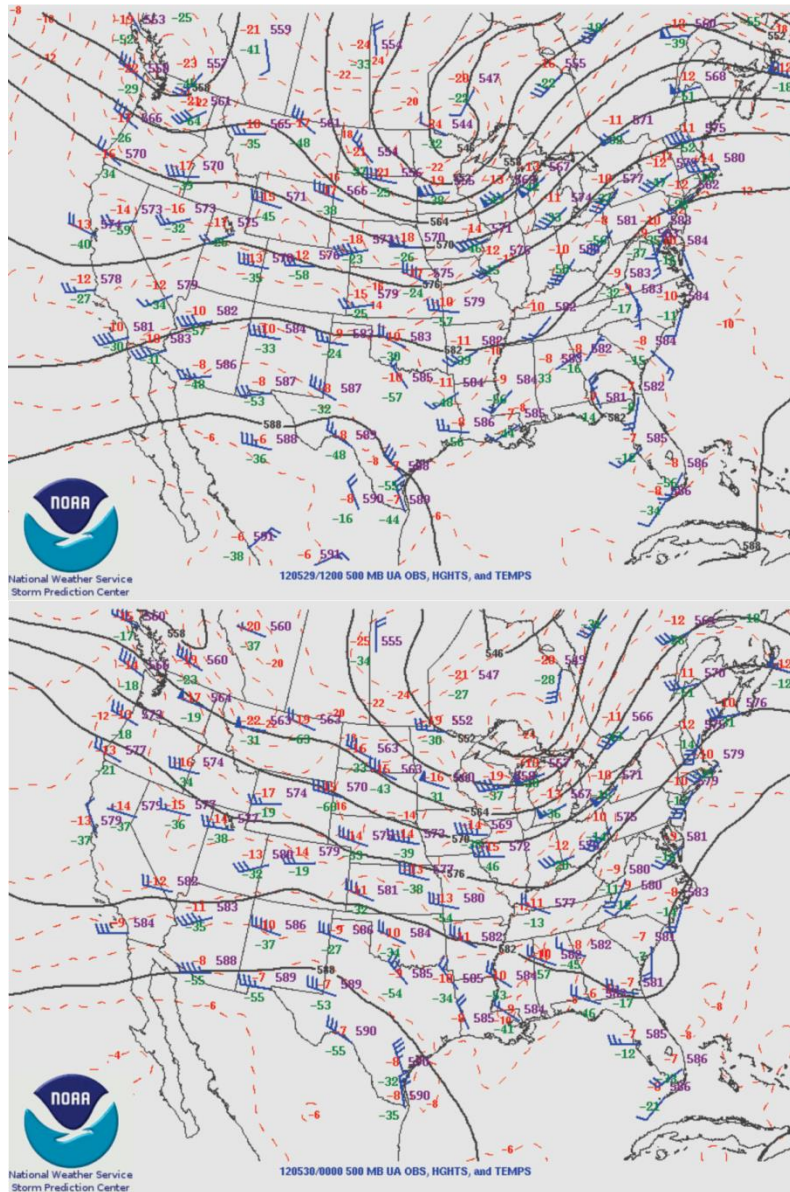
Figure 3. 500mb analyses from the Storm Prediction Center (SPC) archive for a) 29 May at 12:00 UTC and b) 30 May at 00:00 UTC.

22:55 UTC (Fig. 4). Mixed-layer convective available potential energy (MLCAPE) and 0-3 km storm-relative helicity (0-3SRH) calculated from the sounding were 2372 Jkg^{-1} and 271 m^{2}s^{-2}, respectively. A second environmental sounding, which was launched at 0020 UTC on 30 May and was more representative of the environment in which the storm underwent most of its intensification, had MLCAPE and 0-3SRH values of

Figure 4. Environmental sounding launched at 22:55 UTC.
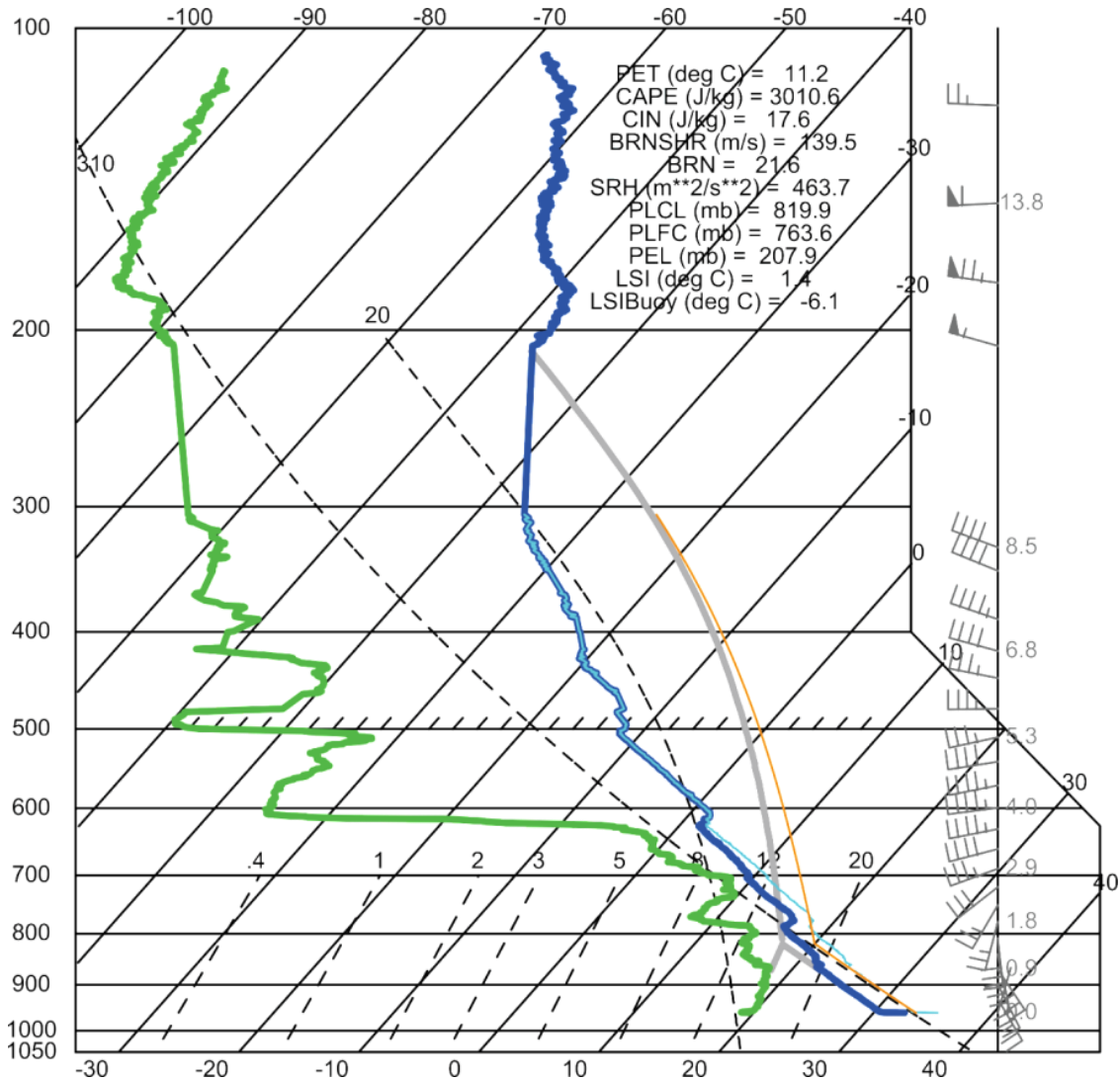
Figure 5. Environmental sounding launched at 00:20 UTC. Two critical parameters used in the diabatic Lagrangian analysis are the ambient environmental melting level (~ 4.1 km AGL) and the -15 C level in the moist-adiabatic main updraft (~ 7.7 km). The freezing level in the moist-adiabatic updraft is at ~ 5.2 km.
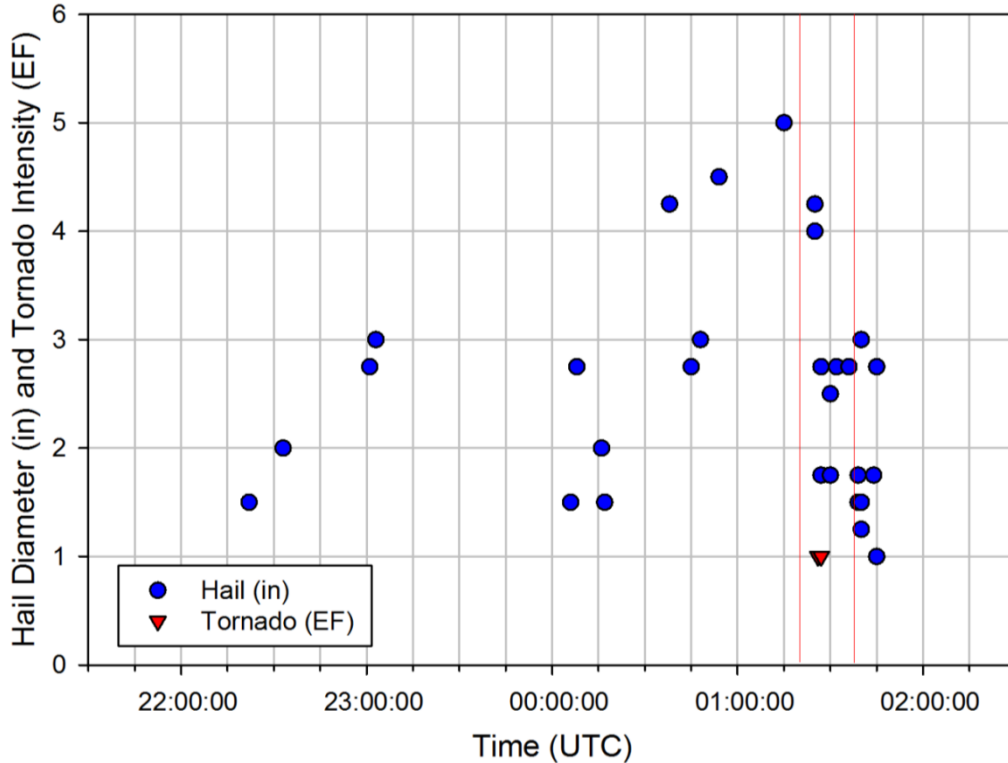
Figure 6. Severe event reports from the StormEvents database for the 29 May 2012 Kingfisher storm lifetime. The red lines indicate the period during which the merger took place.

3010.6 Jkg^{-1} and 463.7 m^{2}s^{-2} respectively (Fig. 5). Both soundings indicate that the environment was favorable for supercell thunderstorms.

The Kingfisher supercell storm began at approximately 21:00 UTC in north-central OK, when the first reflectivity echoes were detected at the lowest elevation angle of KTLX. The first lightning flash in the storm was detected by the OK LMA at 21:34 UTC (Fig. 7). By 22:00 UTC, the storm had transitioned into the supercell phase (A thunderstorm is termed a supercell when it has a quasi-steady rotating mesocyclonic updraft that may persist for tens of minutes to hours [Bunker et al. 2006]). The first CG flash detected in this storm by the NLDN was at 22:07 UTC.

For two hours after the onset of electrical activity, total flash rates remained low,
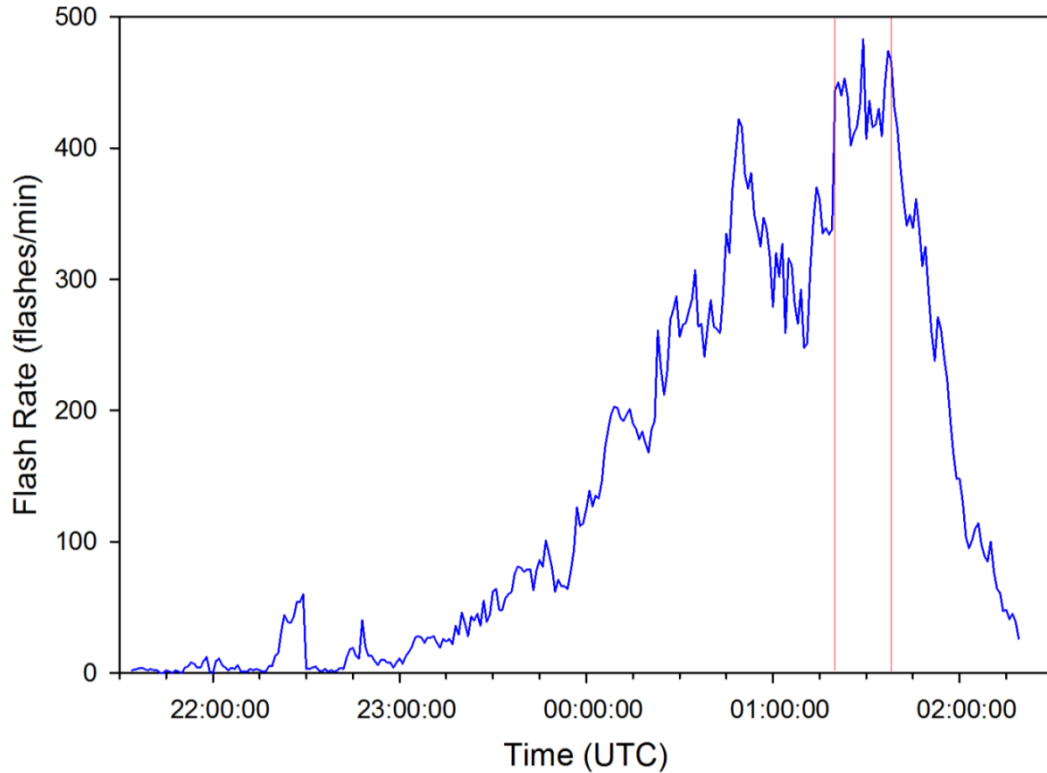
Figure 7. Total lightning flash rates for the storm lifetime. The red lines indicate the period during which the merger took place.

except for a 10-minute burst above 50 min^{-1} that began at 2218 UTC. This surge in flash

activity was concurrent with a storm split. The first report of severe hail from the storm

occurred at 2222 UTC, within minutes of the split (e.g., Fig. 6). By 22:30 UTC, the left

and right movers were completely separate at the lowest radar elevation angle, and

subsequent flashes were analyzed only if they occurred in the right mover, which is the

focus of this study. The same criterion was applied to CG flashes detected by the

NLDN.

A bounded weak lightning region (BWLR, (Ziegler et al. 2014), defined as a

region containing a prominent relative minimum in VHF source density, formed at

22:45 UTC and persisted until 00:40 UTC (as partially illustrated in results to be

presented) before subsequently filling in. The BWLR was collocated with a bounded

31
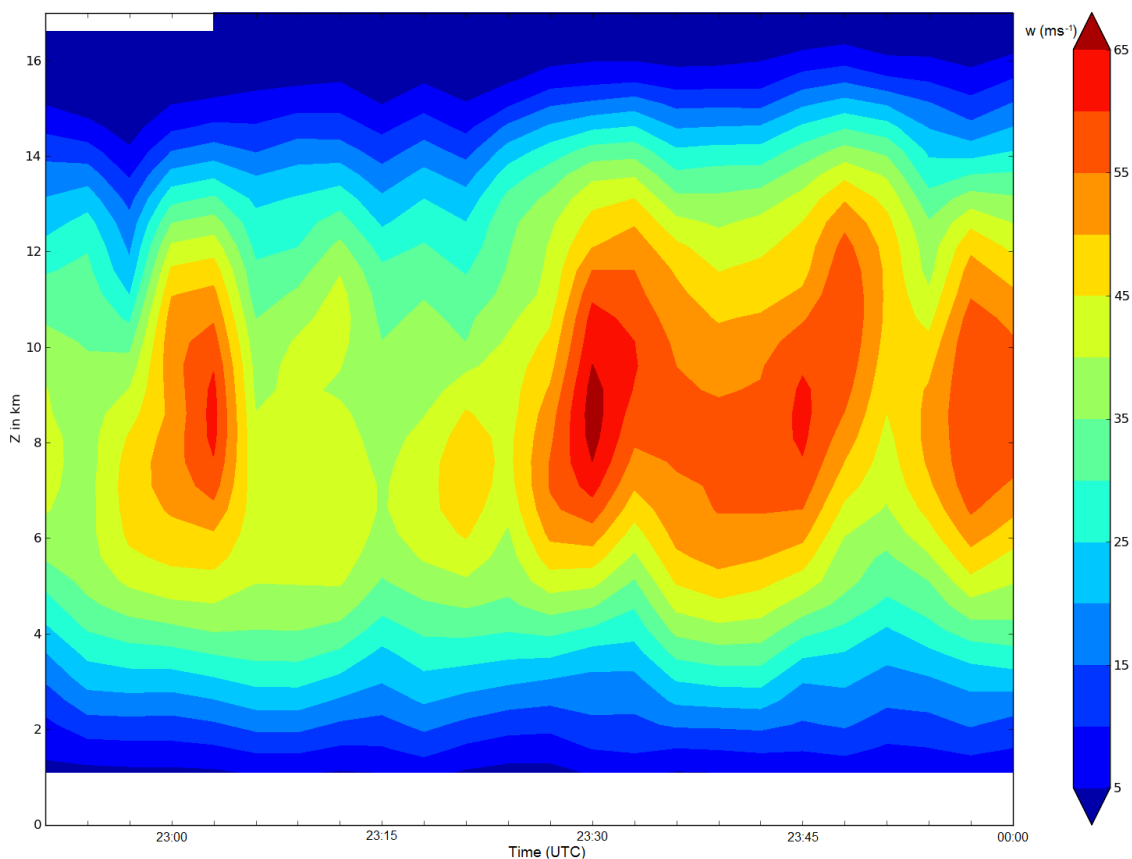
Figure 8. Time-height plot of maximum updraft in the storm core (figure courtesy of Dan Betten).

weak echo region (BWER) and part of the mesocyclone. Although the BWLR feature

has previously been termed a "lightning-weak hole" (e.g., Krehbiel et al. 2000) or

alternatively a "lightning hole" (e.g., Emersic et al. 2011), Ziegler et al. (2014)

introduced the BWLR terminology by analogy to the well-recognized BWER storm

feature. The BWLR terminology is also more generally applicable to e.g., cases where

a mantle of lightning activity overlies a localized lightning-free region.

The target storm began intensifying rapidly after 23:15 UTC, reaching a peak of

65 m s^{-1} at 23:30 UTC in triple-Doppler synthesized winds (Fig. 8), By 00:03 UTC on

30 May, total lightning flash rates had increased to well over 100 min^{-1} and the

maximum updraft speed was 55 m s^{-1} (e.g., Figs. 7 and 8, respectively). CG flash rates

32
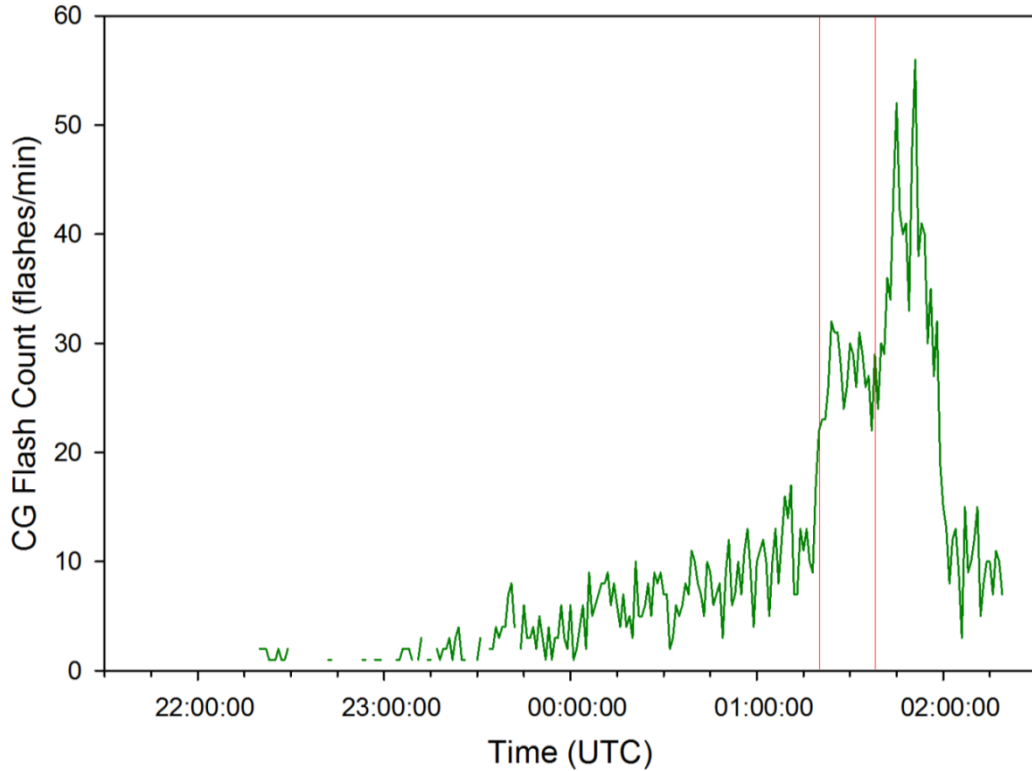
Figure 9. CG flash rates for the storm lifetime. The red lines indicate the period during which the merger took place.

also increased during this period, although less substantially (e.g., Fig. 9). After 00:03

UTC both total and CG flash rates continued increasing, and there were several reports

of severe hail and strong wind. The largest hail reported was 12.7 cm (5 in) in diameter

at 01:15 UTC. At 01:20 UTC, a merger commenced just west of Oklahoma City

between the target storm and another supercell, the left-mover from a split that occurred

near the southern Oklahoma-Texas border. At 01:20 UTC the two cells were no longer

distinguishable from one another in the LMA data, because the upper levels of the

storms were merging. An EF-1 tornado generated by the target cell was reported at

01:26 UTC, although it was visible in the radar data as early as 01:22 UTC. The

reflectivity signatures at lower levels merged completely at 01:38 UTC, and the tornado

dissipated shortly before that. There were several reports of hail, ranging from 2.5-10.2 cm (1-4 in) in diameter, while the merger was taking place (e.g., Fig. 6).

Prior to the merger, the target storm's flash rates peaked at 422 min^{-1} at 00:49 UTC. During the merger rates peaked at 483 min^{-1}, but this latter maximum may be partly an artifact of the sudden inclusion of flashes from another strong storm. After the conclusion of the merger, there was (1) an increase in the altitude of the maximum VHF source density, (2) a brief increase but overall downward trend in the mean altitude of flash initiations, (3) an increase in CG flash rates, and (4) a sharp decrease in total flash rates. Together, these suggest that the merger caused a significant shift in the microphysical and kinematic structure of the storm. Within 30 minutes of the merger's conclusion, the storm began dissipating. Flash rates dropped rapidly to near zero, and the reflectivity and mesocyclone both weakened and became disorganized. Thus, by merging, both supercells weakened. We speculate that the dissipation of the final merged storm was caused by the two updrafts interfering with each other and/or by the southern cell's downdrafts cutting off the warm inflow to the merged storm. Detailed characteristics of the merger and their effects on the merged storm will be the subject of future study.

Maxima in lightning parameters throughout the storm's lifetime may be directly related to incidents of severe hail (Figs. 6-7 and Figs. 9-11). The relationships between lightning activity and the tornado are less clear, because the tornado occurred during the merger, when there were complex interactions between the two storms for many processes. The first two hail reports occurred within minutes of the first surge in lightning activity. The third and fourth hail reports were concurrent with the start of the
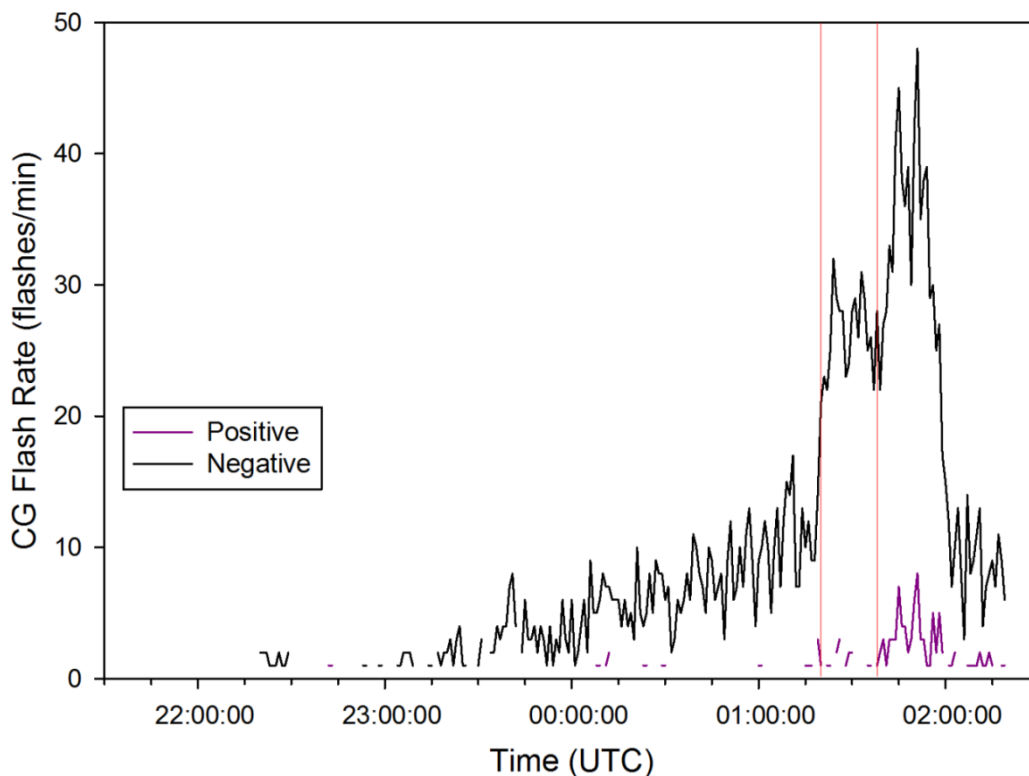
Figure 10. CG flash rates, separated by CG polarity, for the storm lifetime. The red lines indicate the period during which the merger took place.

storm's steady increase in total flash rates. After that, three clusters of hail reports were

associated with sharp increases in total flash rates, just before 00:00 UTC and 00:45

UTC, and again during the storm merger. Note that the increase in hail reports during

the merger is partly an artifact of the inclusion of the southern cell, but there were

several reports of hail in the Kingfisher storm during this time.

The CG flash rates exhibited a few distinct patterns through the course of this

storm's lifetime (Figs. 9-10). Beginning at 23:00 UTC (e.g., as the storm began to

intensify), the CG flash rates varied considerably minute-to-minute, but had an overall

upward trend. This trend was not as pronounced as the upward trend in total flash rates.

Before the merger, the CG flash rate peaked at 17 min^{-1}. During the merger, as was

observed with the total flash rates, there was a large abrupt increase in CG flash rates.

35

This is at least partially an artifact of the sudden inclusion of the lightning from a second storm. However, the trend observed in CG flash rates following the conclusion of the merger implies that some portion of the increased rates during the merger was not due to the merging process itself; after the merger concluded, the CG flash rate increased from 24 min^{-1} to a maximum of 56 min^{-1} in less than 15 minutes. This number may include a small amount of contamination from the surrounding storms, because it was nearly impossible to distinguish with complete confidence between multiple storms with overlapping small-reflectivity boundaries during the later portion of the Kingfisher storm's lifetime. However, these storms did not merge with the Kingfisher storm. The largest positive growth in CG flash rates occurred simultaneously with the decline in total flash rates observed after the merger was completed.

CGs throughout the storm's lifetime were of mixed polarity; negative CGs (i.e., CGs which lower negative charge to the ground) dominated the count, but positive CGs (which lower positive charge) were sprinkled throughout the analyzed period. After the merger, flash rates of positive CGs increased to a maximum of 8 min^{-1} (e.g., Fig. 10), but, as with the total and negative CG flash rates, those numbers may include a few flashes from other cells. CG flashes typically were initiated between the lowest significant charge region and the next highest charge region in the vertical charge distribution, in which case the polarity of the flash is the same as the polarity of the second charge layer. Thus, the presence of CG flashes of both polarities occurring within seconds of each other indicates that the charge structure of the storm varied horizontally and storm-relative shifts in CG locations probably also indicate variability in time. The charge structure of the storm in the first part of its lifetime will be

discussed in the next section. Its structure at times closer to the merger is not included in this study, but will be analyzed in future work.

Although we will not here analyze charge structure during and after the merger, we offer hypotheses which seem to offer likely explanations for the changes in flash rates and will be tested in a future study. The merger of two very electrically active supercells likely caused the sudden increase in CG flash rates by increasing the complexity of the charge distribution, particularly by bringing various polarities of the lowest-altitude charge close together, thereby increasing the low-level electric field and increasing the probability of CG flash initiation. CG flash rates may also have been enhanced by the widely observed tendency for CG flashes to increasingly dominate flash activity as a storm dissipates and the charge regions fall lower. The rapid decrease in total flash rates following the merger probably was caused by the overall weakening of the storms as the interactions of multiple updrafts, downdrafts, and cold pools resulted in a weaker vertical mass flux through the mixed phase region. These hypotheses are consistent with the overall reduction in maximum heights of flash initiations and of the 8-128 VHF source height contours in Figs. 11 and 13, along with the decreasing altitude of the bottom values for these parameters. As noted in the introduction, the tendency observed in other storms is for flash rates to increase with increasing updraft mass flux and particle interactions in the updraft and to decrease as updrafts weaken, thereby causing less charge generation by particle interactions in the mixed-phase region.

Time-height plots of VHF source density, VHF source percentile heights, and flash initiation points are shown in Figs. 11-13. The surge in flash rates beginning
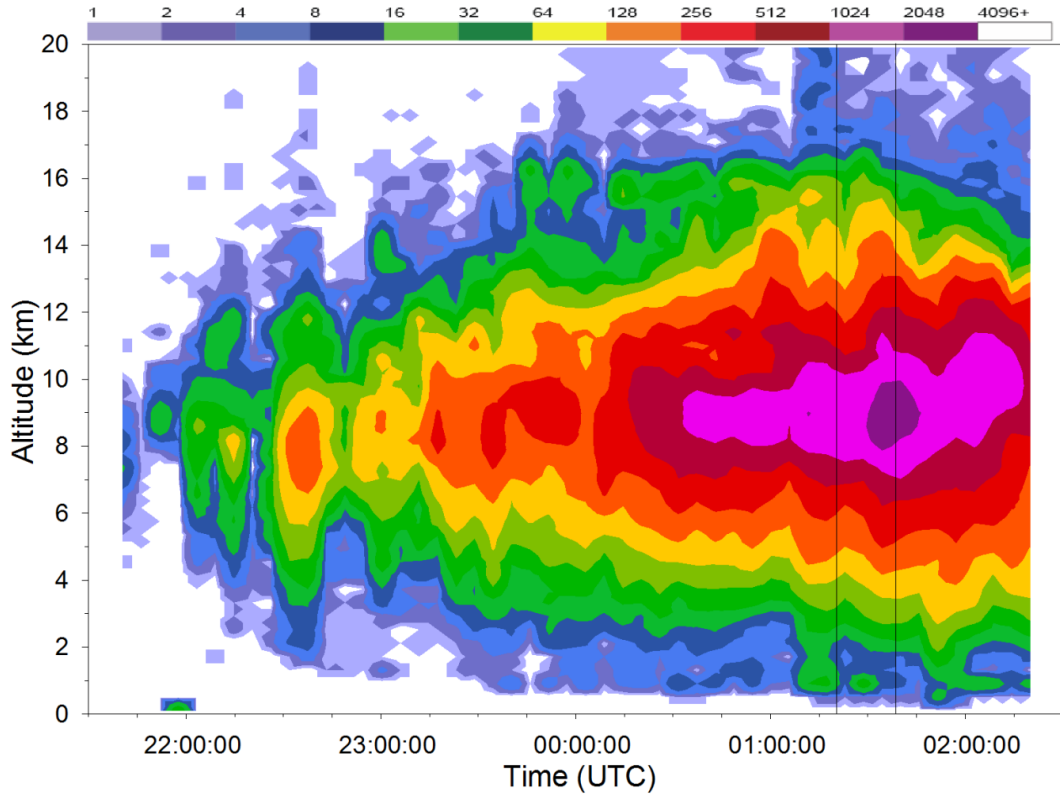
Figure 11. Time-height plot of VHF source densities for the storm lifetime. The black lines indicate the period during which the merger took place.

around 22:18 is reflected in the 99.99[th] VHF source percentile height and in the distribution of the heights of flash initiation points. An increase in VHF source density commenced at this time as well, though a maximum can be seen between 22:30 and 22:45 following the temporary increase in flash rates (Fig. 6a).

Four substantial surges in updraft strength during the period 22:51-00:00 UTC of 3-D multi-Doppler wind analyses (Fig. 8) were related to the storm's electrical structure. The first updraft surge to a maximum of 60 m s^{-1} began at approximately 22:57 UTC and was concurrent with the beginning of a steady rise in total flash rates (Fig. 7), an increase in maximum VHF source density (Fig. 11), a local maximum in VHF source density in the overshooting top, and an increase in mean flash initiation

38
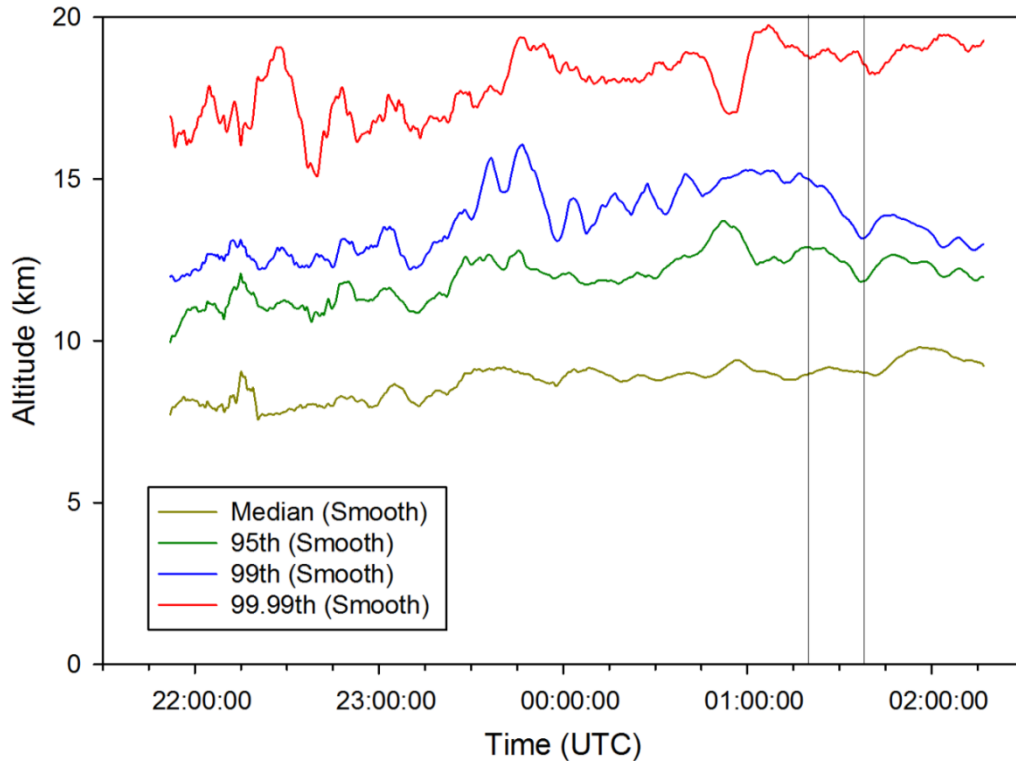
Figure 12. Time-height plot of VHF source percentiles for the storm lifetime. The black lines indicate the period during which the merger took place.

height (Fig. 13). A small surge in VHF source percentile heights is visible in all four percentiles at this time, but it is not substantial (Fig. 12). The second updraft pulse to a maximum of 65 m s^{-1} began at approximately 23:25 UTC, and was concurrent with a more rapid rise in total flash rates, a surge in the 99th VHF source percentile height, and an increase in mean flash initiation height. The third updraft pulse to a maximum of 60 m s^{-1} occurred before the second pulse had completely dissipated around 23:45 UTC, and was concurrent with increasing total flash rates, a maximum in VHF source density, a local maximum in VHF source density in the overshooting top, maxima in the 99th and 99.99th VHF source percentile heights, and a decrease in mean flash initiation height. The final observed updraft pulse to 55 m s^{-1} began at approximately 23:54 UTC following a brief decrease in total flash rate and was concurrent with a rapid increase in
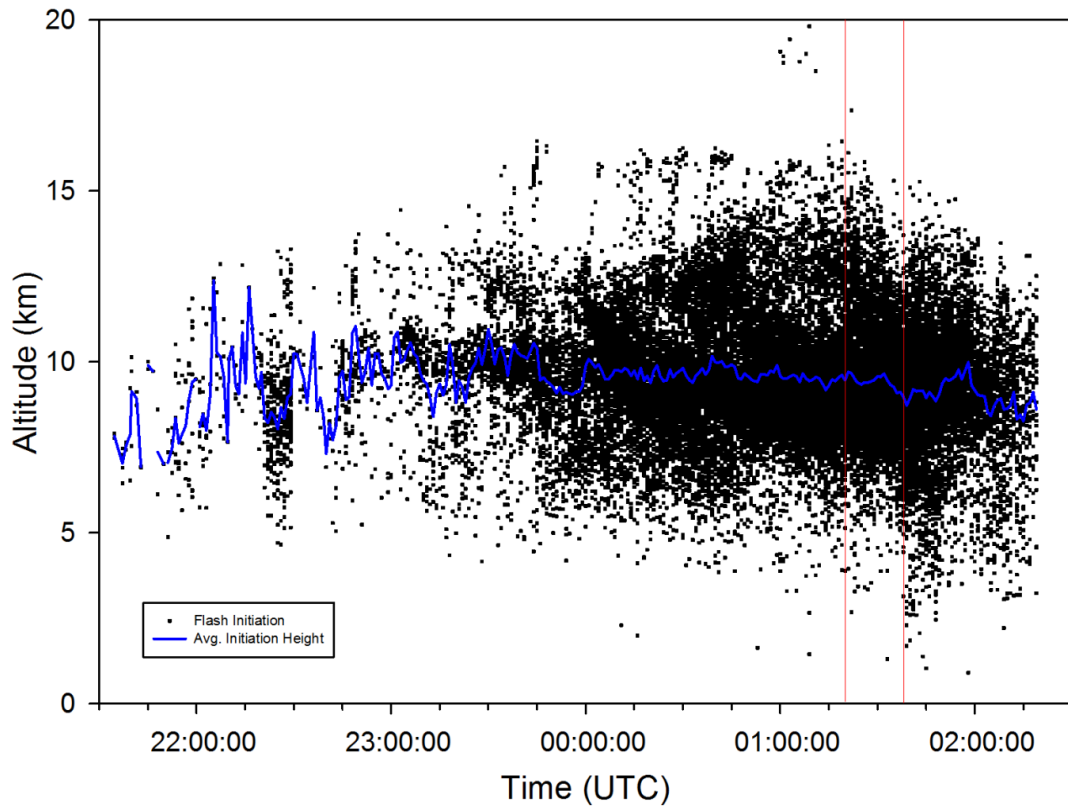
Figure 13. Time-height plot of flash initiations for the storm lifetime. The red lines indicate the period during which the merger took place.

total flash rate, an elevated local maximum in VHF source density, and a minimum in the 99th VHF source percentile height. In general, we can conclude from these observations that the total flash rate is the best proxy for the updraft intensity of a supercell storm, though the presence of elevated local VHF source density maxima also represents periods of updraft intensification well.

The WDSS-II w2segmotionll algorithm first detected secondary convection in the anvil at approximately 23:12 UTC. This convection began producing its own lightning at 23:41 UTC. Before that, several large flashes were initiated in the parent cell and propagated out to the secondary cell, probably due to charge advection into the anvil. One of these flashes occurred four seconds before the WDSS-II algorithm first

detected the secondary convection. Section 3 of this chapter addresses the anvil lightning and secondary convection in more detail. The secondary storm grew and propagated eastward out of the target storm's anvil by 00:00 UTC.

3.2 Gridded lightning and Lagrangian analysis variables

This portion of the study examines gridded values of various properties of the mapped lightning and compares them with storm properties inferred by a combination of the triple-Doppler radar analysis and the diabatic Lagrangian analysis (DLA) of various storm properties for three volume scans at 23:21, 23:39, and 00:00 UTC. Note the following in all DLA figures: (1) black X's indicate grid cells where there was at least one flash initiation; (2) NXP and SR1 were two of the mobile radar locations; (3) NS3 was the launch site for the in-storm balloon; and (4) scale is distance (km) to the north (y-direction) and east (x-direction).

3.2.1 Radar and lightning analyses and DLA (23:21 UTC)

At the first analysis time for this portion of the study, 23:21 UTC, most of the Kingfisher storm's lightning was within the DLA domain. There were three regions of high flash densities in the storm at this time: the southwest side of the BWLR, the northeast side of the BWLR, and the anvil southeast of the storm core (e.g. Figs. 14a-c). The former two high-density areas were concurrent with strong updraft gradients at 9.2 km AGL (the approximate altitude of maximum VHF source density in Fig. 11). The first was also concurrent with a maximum in graupel mixing ratio (q_g) at this altitude, whereas in the second there were low values of q_g (< 3.0 g kg^{-1}) and cloud ice/snow mixing ratio (1.0 g kg$^{-1} \leq q_x < 2.0$ g kg^{-1}) (e.g., Figs. 14b-c, respectively). A BWLR

41
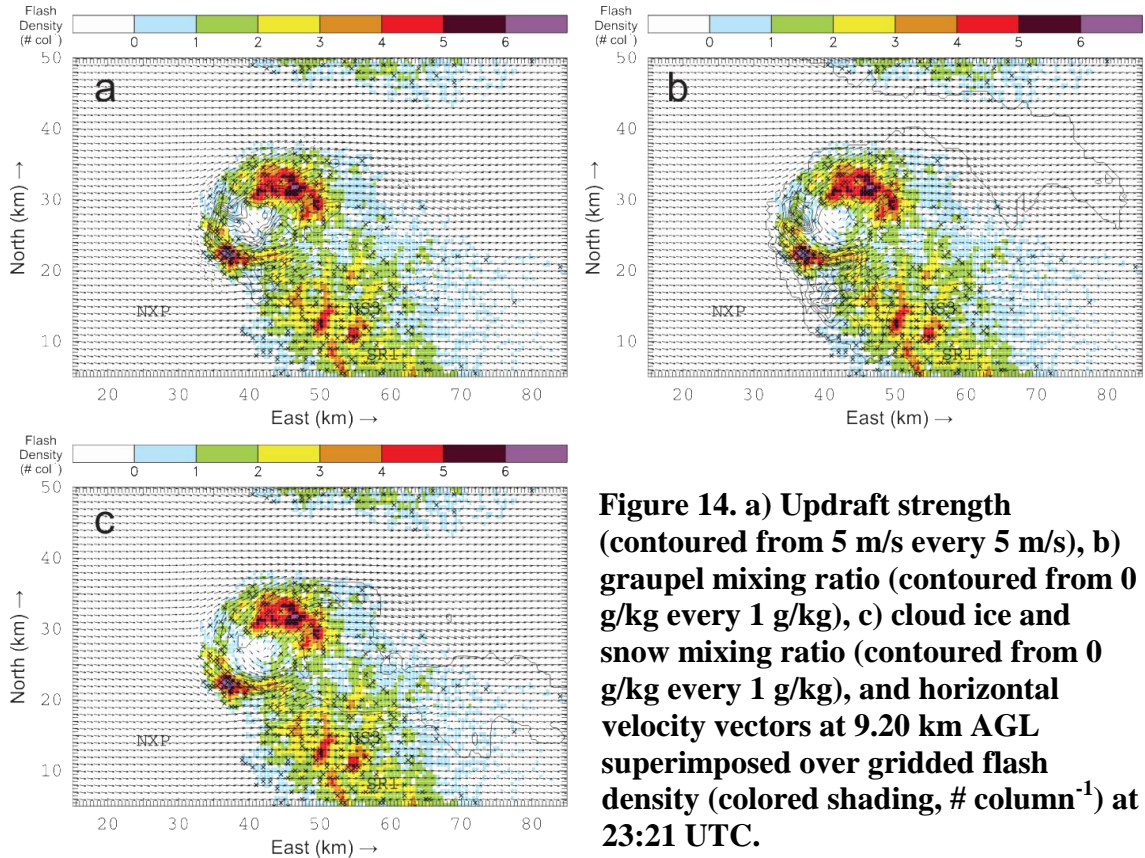
Figure 14. a) Updraft strength (contoured from 5 m/s every 5 m/s), b) graupel mixing ratio (contoured from 0 g/kg every 1 g/kg), c) cloud ice and snow mixing ratio (contoured from 0 g/kg every 1 g/kg), and horizontal velocity vectors at 9.20 km AGL superimposed over gridded flash density (colored shading, # column^{-1}) at 23:21 UTC.

existed in a region of low graupel content ($q_g < 1.0$ g kg^{-1}) and a secondary updraft core (30 m s$^{-1} \leq w < 35$ m s^{-1}) at 9.2 km AGL (Fig. 14a-b).

Most of the flash footprints at the 23:21 analysis time were ≥ 25 km^2 (e.g., Fig. 15a). Flash footprints tended to be smaller (<25 km^2) on the western edge of the BWLR, in and around the primary updraft core (35 m s$^{-1} \leq w < 40$ m s-1) and on the western edge of the anvil, well to the south of the updraft and BWLR. The majority of grid cells had a mean flash size ≥ 50 km^2, and the flashes with the largest sizes, those ≥ 200 km^2, were in the anvil. The region of high flash density southwest of the BWLR was characterized by relatively small flash footprints (< 50 km^2), whereas the high flash density region northeast of the BWLR was characterized by larger flash footprints (≥ 50 km^2).
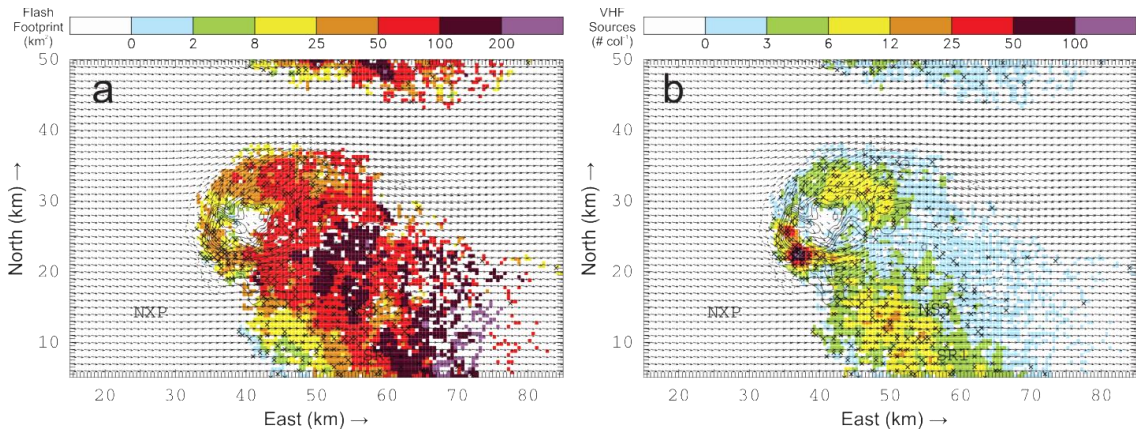
Figure 15. Updraft strength (contoured from 5 m/s every 5 m/s) and horizontal velocity vectors at 9.20 km AGL superimposed over a) gridded flash footprint area (colored shading, km² column⁻¹) and b) VHF source density (colored shading, # column⁻¹) at 23:21 UTC.

The densest clusters of flash initiations were south and west of the updraft core, in a region of large gradients in the updraft and overlapping a maximum in flash density (e.g. Fig. 14a). Initiation densities were somewhat less northeast of the BWLR and in the anvil, where flash footprints were larger, and tended to be much smaller in parts of the anvil with the largest footprints. There were two initiations on the interior edge of the BWLR, and none within either updraft core, though there were some surrounding the primary updraft core. These observations support the conclusion made by Bruning and MacGorman (2013) that grid cells containing high flash initiation densities close to the updraft tend to have smaller mean flash areas.

Overall, the VHF source density had a distinct maximum (>25 sources km⁻²) collocated with the flash density maximum southwest of the BWLR (e.g. Fig. 15b). The other two flash-dense regions in the storm had only a few scattered grid cells containing 12 - 24 sources as their local VHF source maxima. The parameters which distinguished the flash-dense region southwest of the BWLR from the other two flash density maxima

43
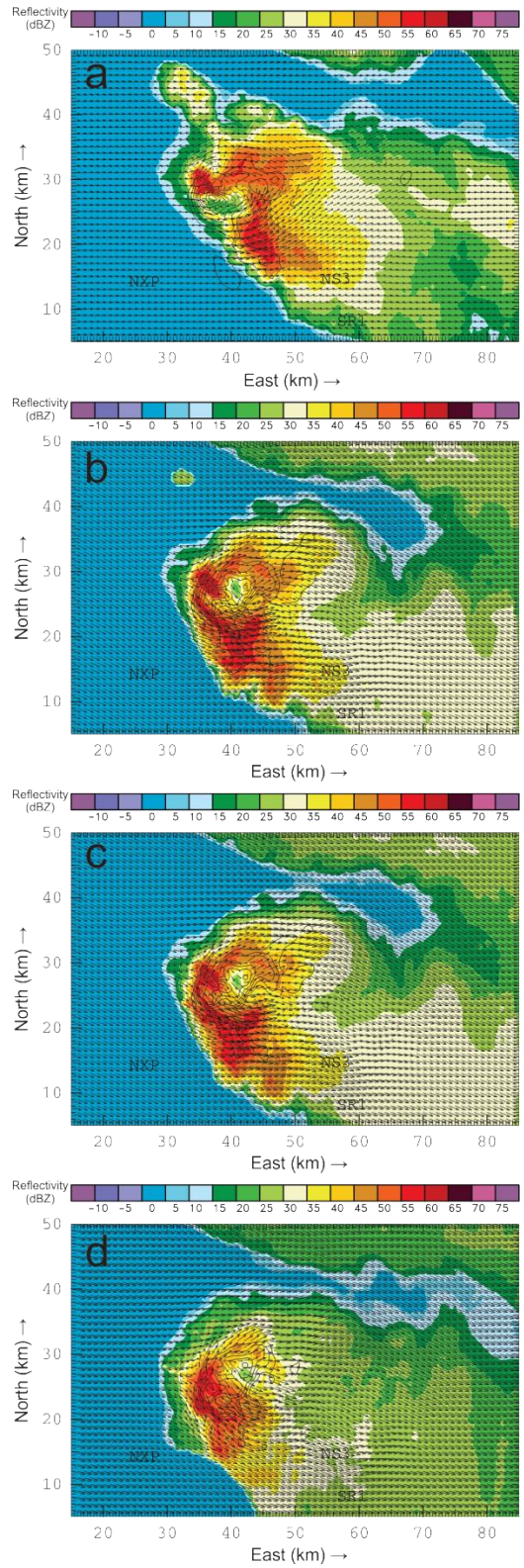
Figure 16: Reflectivity (color shading), updraft strength (contoured from 5 m/s every 5 m/s), and horizontal velocity vectors at a) 5.20 km AGL, b) 8.70 km AGL, c) 9.20 km AGL, and d) 11.20 km AGL at 23:21 UTC.

were the smaller mean flash footprint area, larger VHF source density, and updraft
cores in that region.

The reflectivity from the triple-Doppler analysis revealed a bounded weak echo
region (BWER, e.g., Markowski 2002) in approximately the same location as the
BWLR. The BWER was first visible at the 5.2 km grid level and extended up through
11.2 km (Figs. 16a-d). Though its position in the horizontal plane shifted northward as
the analysis moved up through the vertical, the BWER was located on the eastern side
of the primary updraft core. When a secondary updraft core became visible at 8.7 km,
the BWER was situated between the two updraft maxima, and remained so until the
BWER disappeared. The BWER was smaller than the BLWR in areal extent at the time
of the 23:21 UTC analysis, but it remained within the BWLR at all levels where it
existed.

Graupel existed in the storm from the lowest grid level, 0.2 km, through 15.2 km
(e.g., Fig. 17a-e). Since the calculation for q_g counts hail as graupel, high values of q_g at
or near the surface may be interpreted as hail. There was a likely hail core on the eastern
side of the BWLR from 0.7 km up to 2.2 km (maximum of 8.0 g kg^{-1} ≤ q_g < 9.0 g kg^{-1}
at 1.2 km). Aside from the hail core, pockets of high q_g existed through the lower half of
the storm in areas of low flash density (e.g., the northwest side of the BWLR and south
and east of the BWLR, extending into the anvil), and this pattern was particularly
visible just above the freezing level at ~ 4.4 km. At and above 7.2 km, higher values of
q_g began appearing in the region of high flash density on the southwest side of the
BWLR. Beginning at 11.2 km, almost all q_g ≥ 1.0 g kg^{-1} was concentrated there, and as
altitude increased, the q_g contours disappeared from everywhere in the domain except
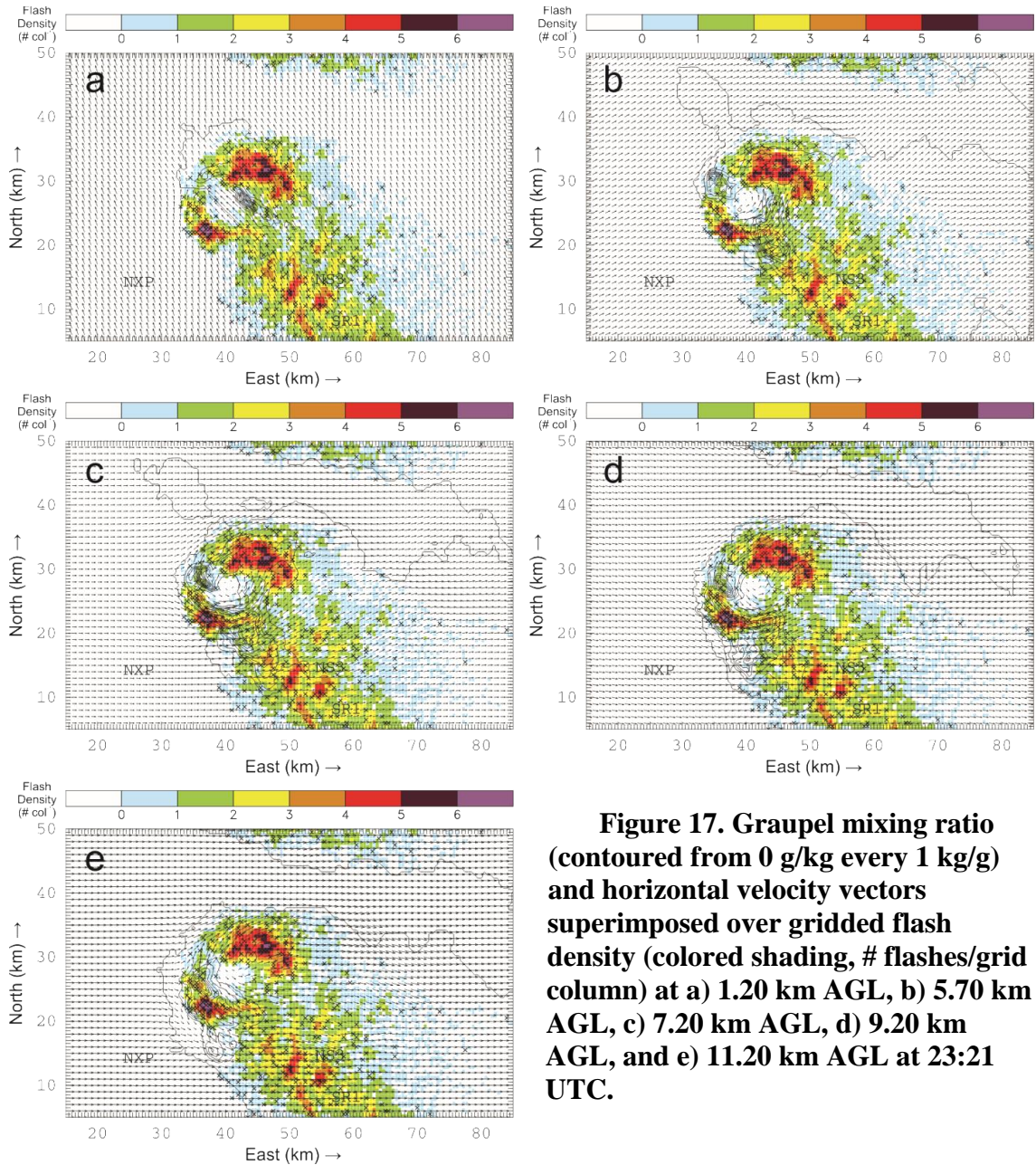
Figure 17. Graupel mixing ratio (contoured from 0 g/kg every 1 kg/g) and horizontal velocity vectors superimposed over gridded flash density (colored shading, # flashes/grid column) at a) 1.20 km AGL, b) 5.70 km AGL, c) 7.20 km AGL, d) 9.20 km AGL, and e) 11.20 km AGL at 23:21 UTC.

for that high flash density region. 15.2 km was the last altitude at which graupel was found by the DLA, and it only existed on the southwest side of the BWLR.

Cloud ice/snow (q_x) first appeared at 6.7 km in a small pocket of less than 1.0 g kg^{-1} in the eastern anvil (Fig. 18). At higher levels, more pockets of q_x appeared in the same region, as well as around the high flash density region northeast of the BWLR. By
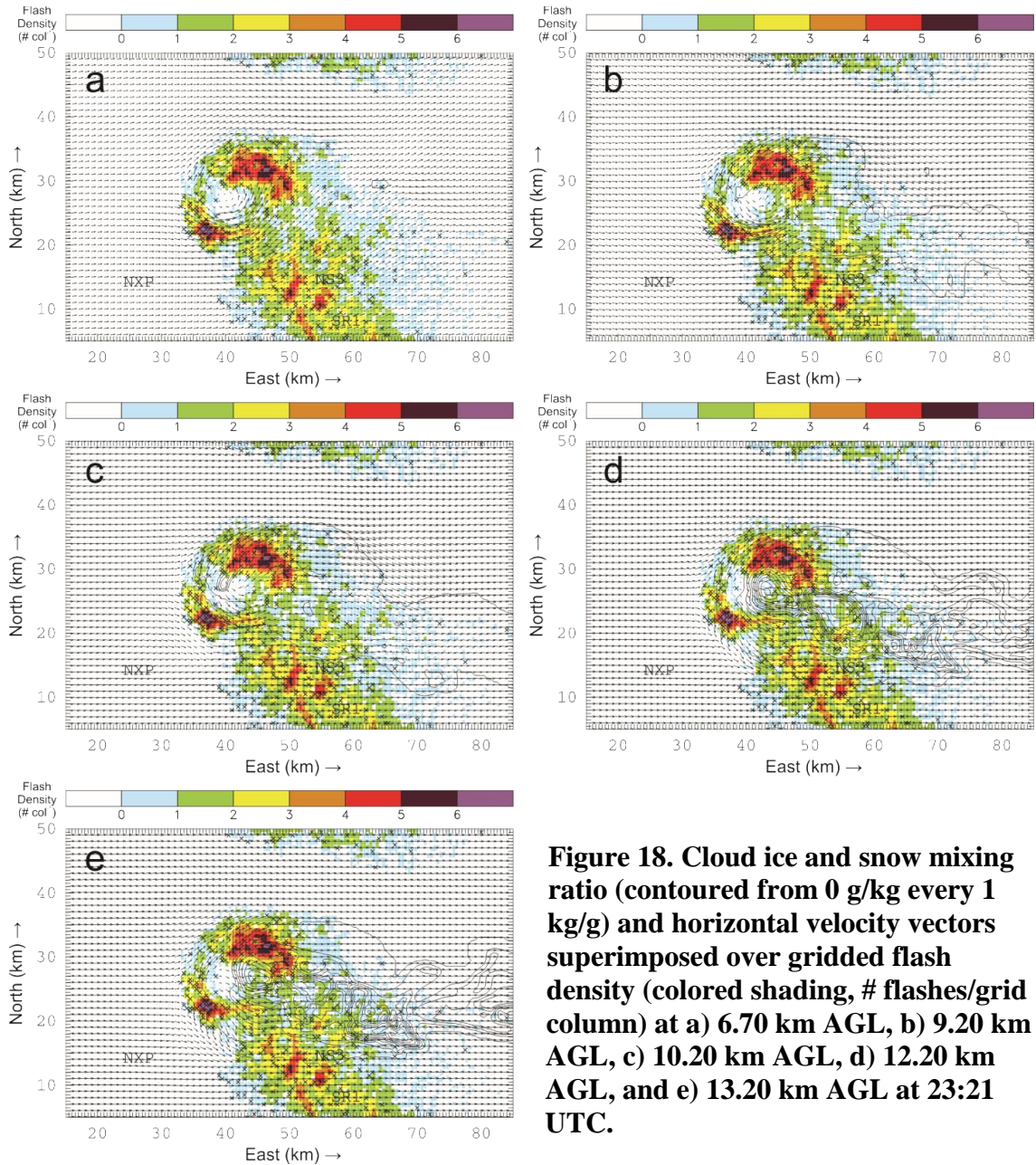
Figure 18. Cloud ice and snow mixing ratio (contoured from 0 g/kg every 1 kg/g) and horizontal velocity vectors superimposed over gridded flash density (colored shading, # flashes/grid column) at a) 6.70 km AGL, b) 9.20 km AGL, c) 10.20 km AGL, d) 12.20 km AGL, and e) 13.20 km AGL at 23:21 UTC.

10.2 km, q_x extended throughout the eastern anvil and storm core but was concentrated in and around the high flash densities northeast of the BWLR, and the maximum q_x values at this level existed in the BWLR ($6.0 \text{ g kg}^{-1} \leq q_x < 7.0 \text{ g kg}^{-1}$). That q_x core grew and centered on the eastern edge of the BWLR as altitude increased, with values
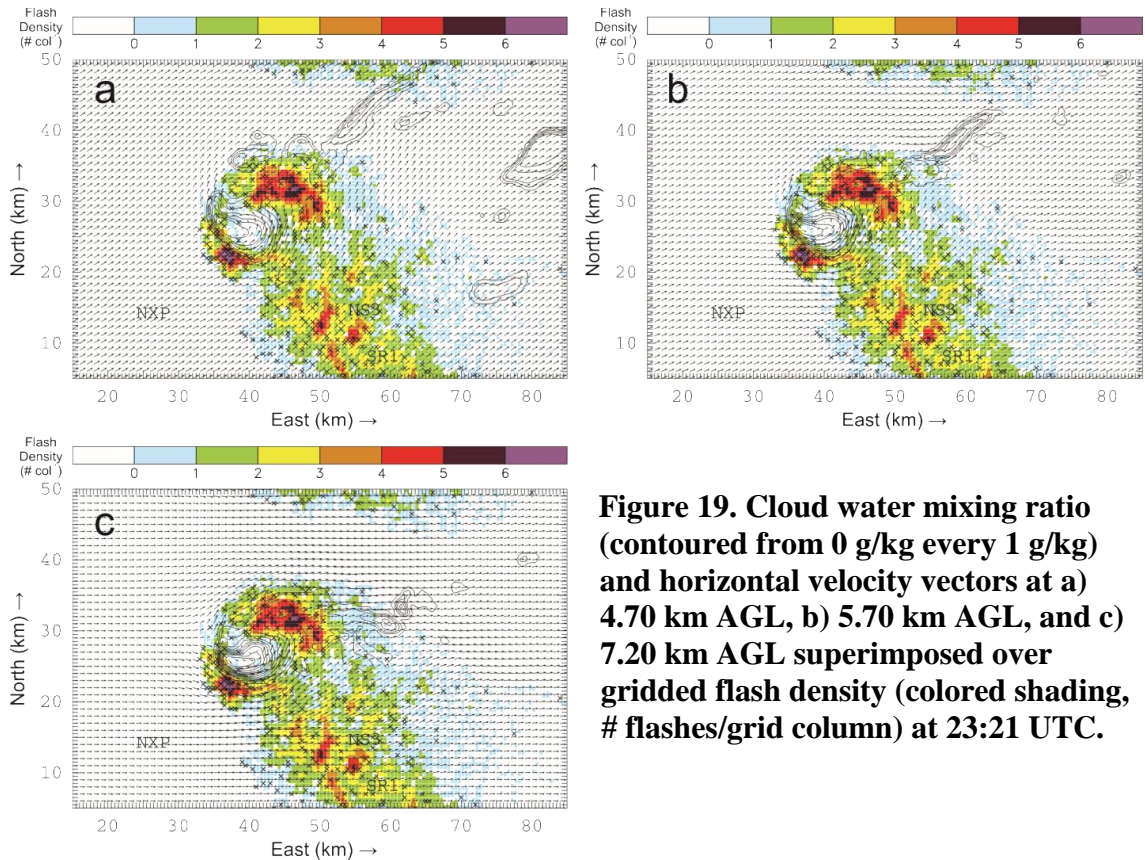
Figure 19. Cloud water mixing ratio (contoured from 0 g/kg every 1 g/kg) and horizontal velocity vectors at a) 4.70 km AGL, b) 5.70 km AGL, and c) 7.20 km AGL superimposed over gridded flash density (colored shading, # flashes/grid column) at 23:21 UTC.

increasing to 10.0 g kg^{-1} from 11.2 km to 12.2 km. In the eastern edge of the storm and in the eastern anvil, $q_x \geq 7.0$ g kg^{-1} between 11.7 km and 13.7 km with the maximum of 8.0 g kg$^{-1} \leq q_x < 9.0$ g kg^{-1} at 13.2 km. Above 13.2 km, q_x decreased as altitude increased southeast of the BWLR until it disappeared completely above 15.70 km (the last values in the anvil were visible at 14.2 km).

The two DLA liquid water content variables, cloud water mixing ratio (q_c) and rain water mixing ratio (q_r), were found throughout the mixed phase region above ~ 4.7 km (e.g., Figs. 19-20). Supercooled rain existed as high as ~ 7.2 km in the main updraft (due to size-dependent delayed drop freezing during upward motion) while supercooled cloud water was analyzed as high as ~ 11 km around -40°C in the main updraft. The maximum supercooled q_r was observed at 4.7 km (5.0 g kg$^{-1} \leq q_r < 6.0$ g kg^{-1}) and was

48
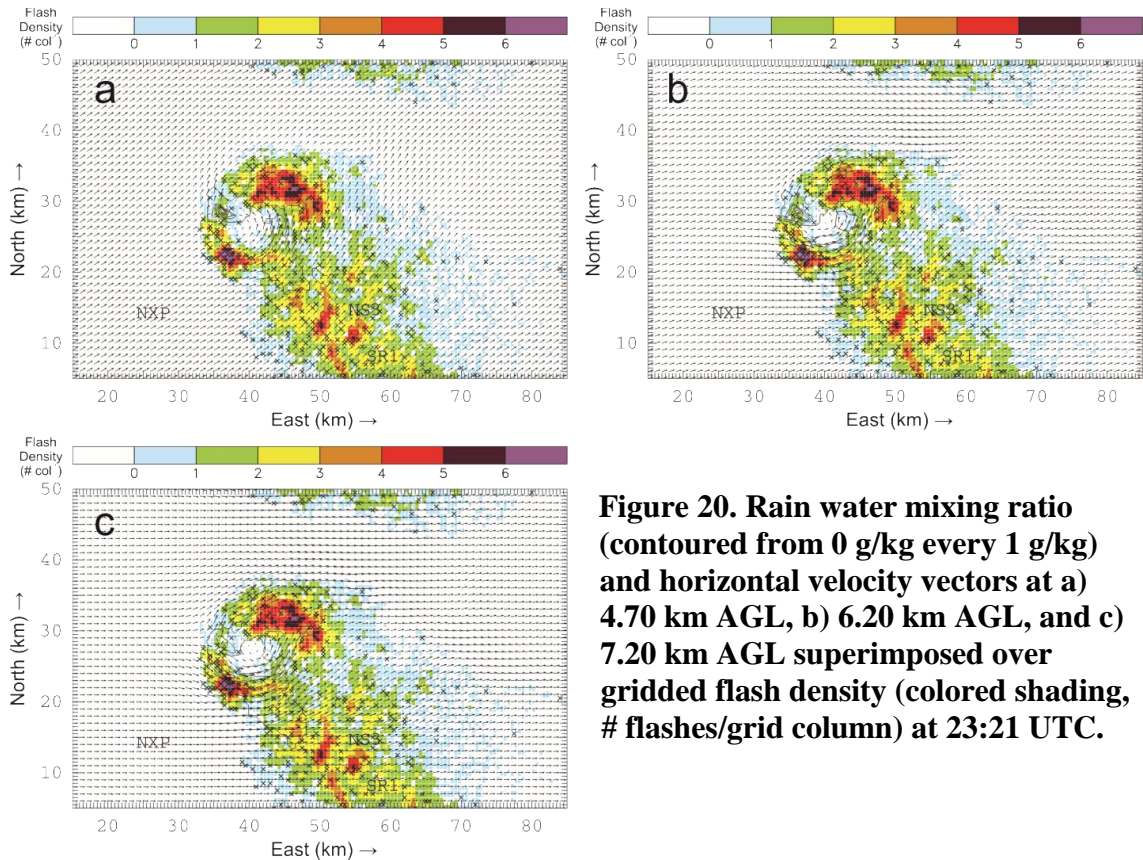
Figure 20. Rain water mixing ratio (contoured from 0 g/kg every 1 g/kg) and horizontal velocity vectors at a) 4.70 km AGL, b) 6.20 km AGL, and c) 7.20 km AGL superimposed over gridded flash density (colored shading, # flashes/grid column) at 23:21 UTC.

coincident with the region of low flash density and small flash footprints on the northwest side of the BWLR. The maximum supercooled q_c was observed at 7.2 km ($11.0 \text{ g kg}^{-1} \leq q_c < 12.0 \text{ g kg}^{-1}$) and was coincident with the BWLR.

Through the vertical extent of the storm at 23:21 UTC, the updraft core was positioned west of the BWLR and tilted toward the south with height (e.g., Fig. 21). Part of the updraft core remained consistently in or near a region of high flash density, high VHF source density, high flash initiation density, and relatively small mean flash footprint. At 12.2 km, there were multiple updraft cores. An examination of VHF source densities in the vertical during the period 23:16-23:26 UTC (i.e., the raw data that was gridded for the 23:21 analysis time) revealed that this dense region of small flashes peaked at ~12 km in the vertical, ~3 km above the horizontal layer containing
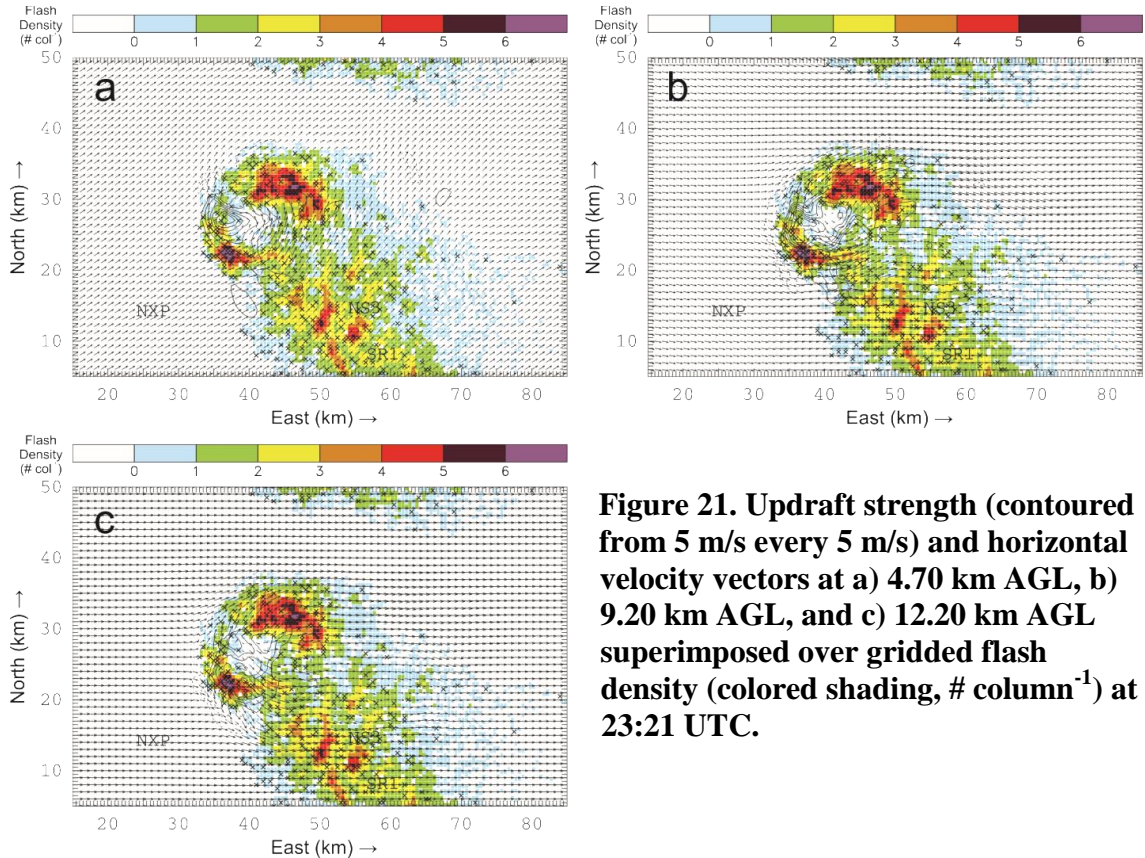
Figure 21. Updraft strength (contoured from 5 m/s every 5 m/s) and horizontal velocity vectors at a) 4.70 km AGL, b) 9.20 km AGL, and c) 12.20 km AGL superimposed over gridded flash density (colored shading, # column^{-1}) at 23:21 UTC.

the most VHF sources. The 12.2 km DLA level contained diverging horizontal winds with a maximum $7.0 \text{ g kg}^{-1} \leq q_g < 8.0 \text{ g kg}^{-1}$, collocated with the VHF-source-dense region. There was also a cluster of flash initiations at that height (e.g., Fig. 6c) consistent with the high flash initiation densities seen at that location in the two-dimensional gridded analysis. The larger mixing ratios of cloud ice and snow were located immediately to the east of these other maxima.

As noted above, there were three regions of high flash density in the storm at 23:21 UTC, but the structure of flashes in one of them was different from the structure in the other two and had a larger maximum in VHF source density. That region also was characterized by small flashes, and a detailed examination of these flashes revealed a large number of channels in a compact space (including channels moving vertically

between charge regions) and highly curved/tortuous structures. Thus, the highly tortuous nature of these small flashes resulted in many more VHF sources emitted in a more compact space than anywhere else in the storm. In the other two flash-dense regions, the flashes tended to propagate in the horizontal more than in the vertical and had larger footprints. These flashes, although large, contained smaller VHF source densities than the smaller flashes observed in the updraft region, so we infer that they likely had lower tortuosity.

An analysis of several flashes in the updraft region southwest of the BWLR indicated that the flashes involved a layer of negative charge at ~11-12 km and a layer of positive charge at ~8-9 km (e.g., Fig. 22a). The sources penetrating positive charge were distributed in an amorphous cloud in which linear channels could not be readily discerned, a distribution suggesting there were many channels traversing the charge region. Normally, because negative leaders are more impulsive than positive leaders and so tend to produce many more VHF sources than positive leaders, VHF sources tend to be much denser from channels propagating outward through positive charge. However, several of the flashes considered in this analysis had higher densities of VHF sources in a region of negative charge, as negative recoil streamers within the negative charge propagated back toward the positive charge. On the other hand, each flash tended to have a larger total number of VHF sources in positive charge, but these sources were distributed over a larger horizontal region, and so produced smaller densities than produced by the VHF sources in negative charge.

On the northeast side of the BWLR, a negative region was inferred at ~11-12 km, with a positive region beneath it (e.g., Fig. 22b). Negative leaders sometimes

51
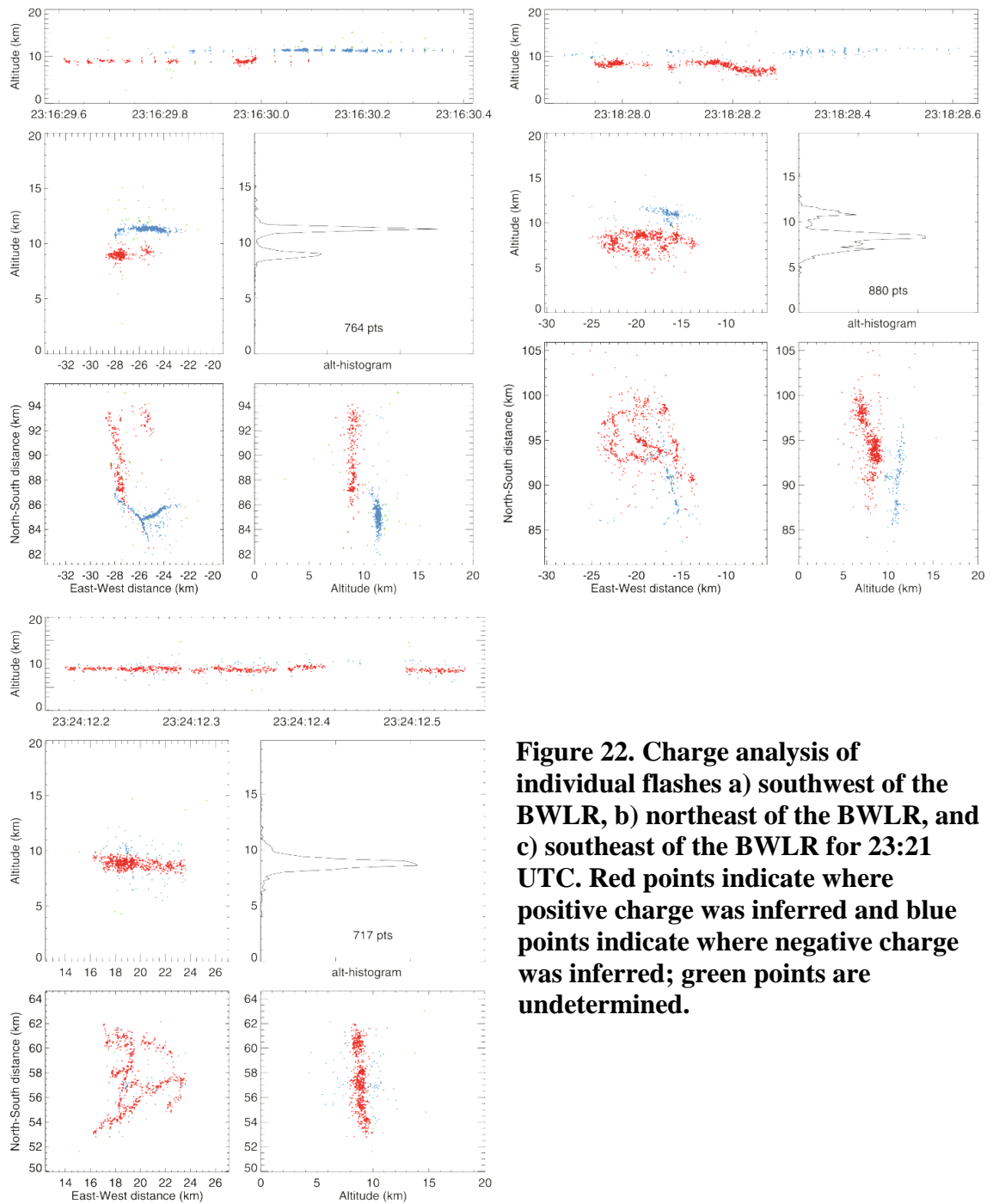
Figure 22. Charge analysis of individual flashes a) southwest of the BWLR, b) northeast of the BWLR, and c) southeast of the BWLR for 23:21 UTC. Red points indicate where positive charge was inferred and blue points indicate where negative charge was inferred; green points are undetermined.

sloped down towards ~ 6 km in altitude when the lightning channels propagated north. In some cases, it appeared that negative leaders actually propagated horizontally, upward, and then curved around to propagate in a direction opposite the original propagation, thus creating C-shaped flash signatures in both the vertical and horizontal, as demonstrated in Fig. 23a. This combined with sometimes-sloped negative channels may indicate a deep positive charge layer from approximately 6-10 km and northeast of the BWLR.

Some flashes, which initiated immediately southeast of the BWLR, propagated north and then west, thus circumventing the BWLR, most likely because there was deficient charge within it (e.g., Fig. 23b); having smaller or fewer hydrometeors in that area, as indicated by the BWER, supports this conclusion. Ziegler et al. (2014) analyzed electrification, lightning, and BWLRs in a simulated supercell, showing that the individual hydrometeor space charge densities were approximately zero in the simulated BWLR even outside the simulated BWER where simulated precipitation contents and reflectivity were large. In the far southeast region of the storm, flash structures were primarily horizontal. There was a layer of positive charge at ~8-10 km in this part of the storm (e.g., Fig. 22c), which appeared to be deeper or sloped downward near the BWLR (e.g., Fig. 23b) and toward the northern and eastern flanks of the storm. Southeast beyond this region, in the anvil, there appeared to be a negative charge region which descended eastward from ~8 km down to ~5 km, possibly adjacent to the aforementioned positive region.

The presence of graupel, ice crystals, and supercooled water in the flash-dense region southwest of the BWLR suggests that non-inductive charging was occurring
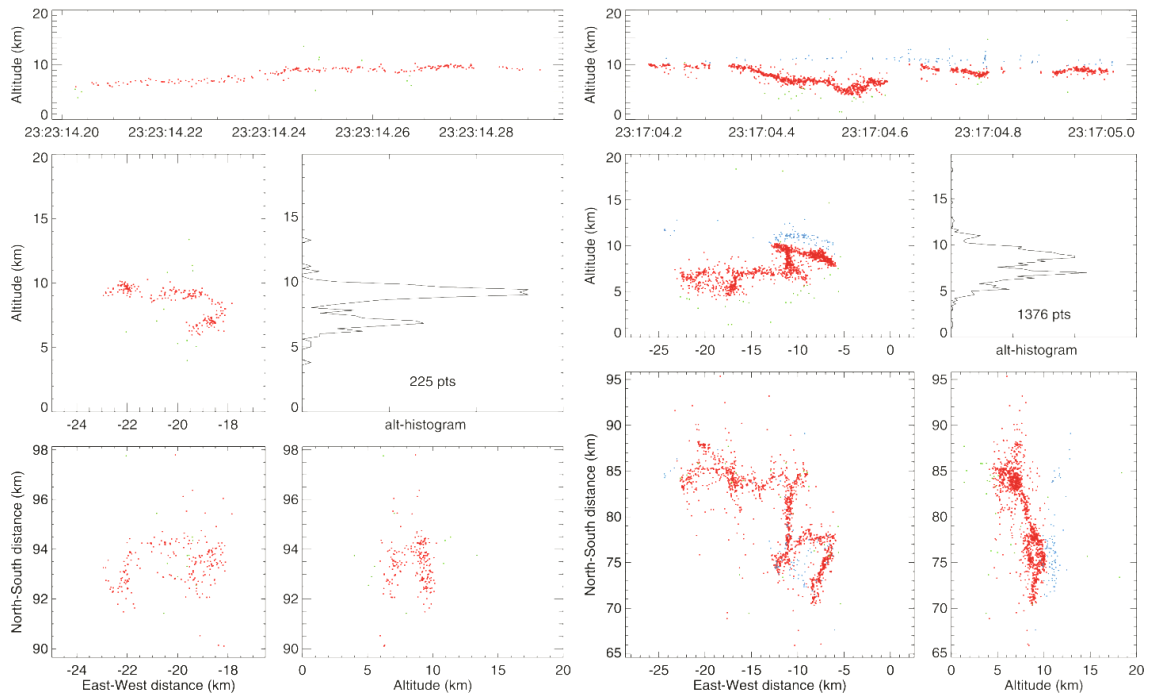
Figure 23. Charge analysis of individual flashes a) northeast of the BWLR, and c) immediately southeast of the BWLR for 23:21 UTC. Red points indicate where positive charge was inferred and blue points indicate where negative charge was inferred; green points are undetermined.

there, enhanced and macroscopically separated by the convective motions of the updraft. The low supercooled cloud water content combined with the very low ice crystal mixing ratios could indicate that charge separation was occurring by a mechanism observed by Takahashi (1978), in which riming ice pellets become positively charged and small amounts of ice crystals, which break off of the riming graupel, become negatively charged. Such a process would account for the inferred upper negative charge region and lower positive charge region. It is also possible that the inferred charge structure at this time could have resulted from size-sorted graupel carrying charge through the vertical. There were reports of 2.75" and 3" hail produced by the storm ~20 min prior to this analysis time; hail growth processes would have resulted in a range of sizes of graupel/ice pellets in the updraft. If riming graupel in the

54

updraft core became positively charged by the noninductive mechanism in either large or very low cloud liquid water content conditions (e.g., Takahashi 1978), then the larger graupel/hail contents could have increased the vertical extent of positive charge within the sides of the updraft as graupel/hail diverged and descended through the storm. In support of the latter process, Ziegler et al. (2014) obtained positively (negatively)-charged graupel and negatively (positively)-charged ice and snow crystals in presence of high (low) cloud liquid water contents in different locations in the main updraft of a simulated supercell. The latter charge distribution hypothetically may have accounted for the wider, more diffuse appearance of negative leaders within the positive charge, and for the vertical extents of flashes in this region being much larger than the horizontal extents.

Northeast of the BWLR and updraft, there was slightly more cloud water and ice crystal content but far less graupel content, suggesting that non-inductive charging may have been occurring but was not directly a source of charge in this region. The regions northeast and southwest of the BWLR were kinematically and microphysically different from each other in spite of having similar charge structures: in addition to the differing hydrometeor mixing ratios, the updraft was much weaker northeast of the BWLR when it was present at all. However, there were also southwesterly horizontal winds in the mid-to-upper levels of the storm. There was likely sedimentation of charge on the outer edges of the updraft, where hydrometeors may have been removed from the updraft via a fountaining effect, or possibly a centrifuge effect, and some horizontal charge advection affecting the distribution of charge in the northern part of the storm. The

presence of downdrafts on the extreme northern edge of it could have accounted for the vertical stretching of charge layers in that area.

In the anvil region far to the southeast of the BWLR, there was no cloud water and almost no ice crystal content diagnosed through all vertical levels, though there were small graupel mixing ratios throughout the region, and the horizontal winds (veering from southeasterly to westerly in the upper levels) did not support the possibility of large amounts of charge being advected from the updraft region. However, there was certainly charge advection from the updraft region into the region immediately southeast of the updraft. The horizontally stratified layers of charge in the southeast anvil region, which reflect the lack of updraft or other turbulent motions, could be partially the result of screening layer charges forming at the cloud boundaries in addition to the combination of some local non-inductive and inductive charging mechanisms.

3.2.2 Radar and lightning analyses and DLA (23:39 UTC)

Between the 23:21 and 23:39 UTC analysis times, one of the three high-flash-density regions persisted, one strengthened, and one weakened. The BWLR was still distinct at 23:39, and maintained approximately the same storm-relative position. The area of high flash density that was to the southwest of the BWLR at 23:21 persisted, shifting east when the storm shifted southeast, so it was situated on the western side of the BWLR at 23:39. The flash-dense region in the anvil strengthened and shifted southward, making it a more flash-dense region than the one north of the BWLR; the latter weakened substantially. On its east and southern sides, the BWLR was bounded by flash densities of 1, with a few cells containing 2-3 flashes. The flash densities
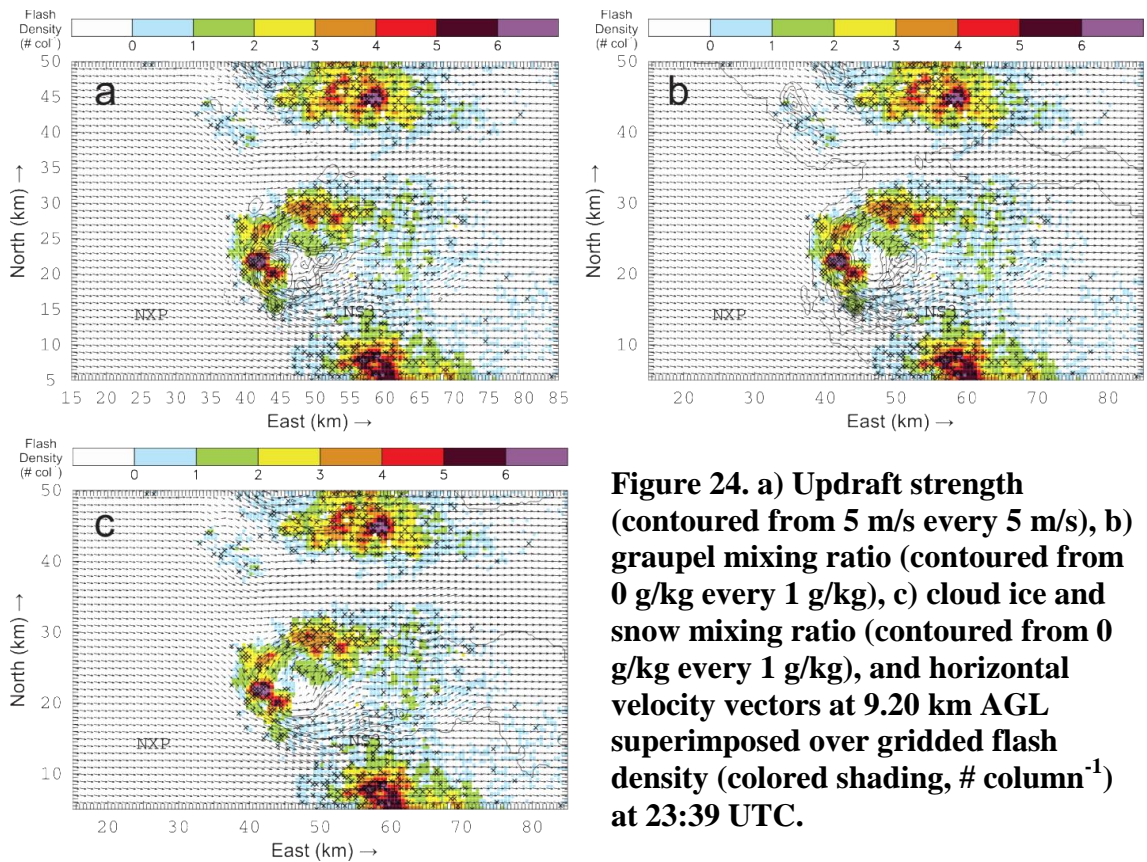
Figure 24. a) Updraft strength (contoured from 5 m/s every 5 m/s), b) graupel mixing ratio (contoured from 0 g/kg every 1 g/kg), c) cloud ice and snow mixing ratio (contoured from 0 g/kg every 1 g/kg), and horizontal velocity vectors at 9.20 km AGL superimposed over gridded flash density (colored shading, # column^{-1}) at 23:39 UTC.

across most of the storm decreased overall, with far fewer cells than at 23:21 containing more than one flash (compare Figs. 14 a-c, 24a-c). At 9.2 km, there was one main updraft core (45 m s^{-1} ≤ w < 50 m s^{-1}) with a few secondary cores surrounding it (Fig. 24a). The main updraft core was just inside the eastern edge of the high flash density region west of the BWLR; a strong gradient in updraft speed existed through that flash-dense area. There were also relatively high graupel mixing ratios in that region (7.0 g kg^{-1} ≤ q$_g$ < 8.0 g kg^{-1} in the center of the high densities in Fig. 24b). Mixing ratios of cloud ice and snow were spread fairly uniformly across the storm core and into the eastern anvil at 9.2 km, though there was no ice crystal content within the mesocyclone or the western half of the BWLR at this level (Fig. 24c).
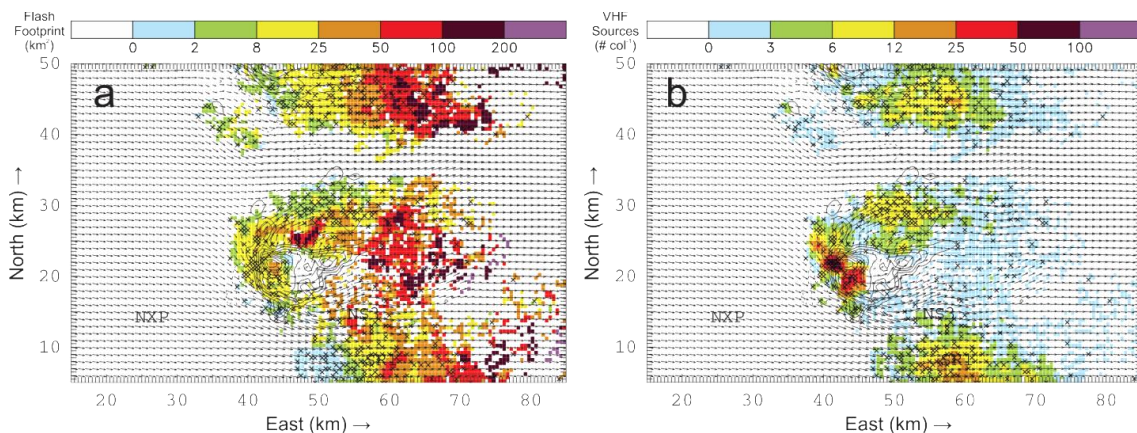
Figure 25. Updraft strength (contoured from 5 m/s every 5 m/s) and horizontal velocity vectors at 9.20 km AGL superimposed over a) gridded flash footprint area (colored shading, km^2 column^{-1}) and b) VHF source density (colored shading, # column^{-1}) at 23:39 UTC.

The flash footprints at 23:39 were also smaller than at 23:21 (compare Figs. 15a, 25a). At 23:39, flash footprints of < 25 km^2 dominated, whereas at 23:21 most flashes were ≥ 50 km^2 in size. A small cluster of flash footprints ≥ 50 km^2 still existed on the northern side of the BWLR, but otherwise those flash sizes were confined to the east and southeast anvil regions. Most of the flashes ≥ 25 km^2 were also in the anvil. Around the BWLR, the dominant flash footprints were 2-25 km^2, with a cluster of flashes with footprints < 2 km^2 south of the storm core.

Grid cells containing flash initiation points were clustered together in the previously noted regions of large flash density and small flash footprint (e.g., Figs, 24, 25a). At 23:39, flash initiations were far denser in the anvil than at 23:21, consistent with the increased flash densities in that region. Flash initiations were sparse in the central area of the storm, which was taken up largely by the BWLR and by flash densities of 1-2 flashes per grid column outside the BWLR.

The same pattern seen in the locations of VHF source maxima at the 23:21 analysis time was evident at the 23:39 analysis time (Fig. 25b). VHF sources were typically most dense where flashes were most dense, but the primary source density maximum (≥ 50 column^{-1}) was collocated with a region of both high flash densities and small flash footprints. This maximum in VHF source density was located on the western side of the BWLR.

The BWER was still present at 23:39, but was less prominent than at 23:21 (Fig. 26a-d). The lower boundary of the BWER was at 4.7 km AGL, situated between two updraft cores, one to its north and one to its south, on the western edge of the storm. At that altitude, however, it was not fully bounded, but instead was shaped as an oblong notch in the western edge of the storm's reflectivity signature. Above 4.7 km, the BWER became more distinct and more completely bounded, reflecting an eastward tilt in the pair of updraft cores. Beginning at 7.7 km, it began to widen, take on an irregular shape, with somewhat weaker bounding reflectivities, although it was still a central region of a minimum in reflectivity. Only above 8.7 km did the central region of weak Z, which was aligned approximately with the BWER at lower altitudes, also become aligned with the BWLR (the BWLR was not clearly defined at lower altitudes, where lightning densities were less overall). These two features remained aligned until all signs of the BWER disappeared at 11.7 km.

The lowest level at which graupel was evident at 23:39 UTC was at 0.2 km, though the values were < 1.0 g kg^{-1}. Multiple signatures resembling hail cores were visible as low as 0.7 km and extended up to above the freezing layer, at which point the distribution of q_g became less compact (e.g. Fig. 27a-e). The maximum q_g reached in
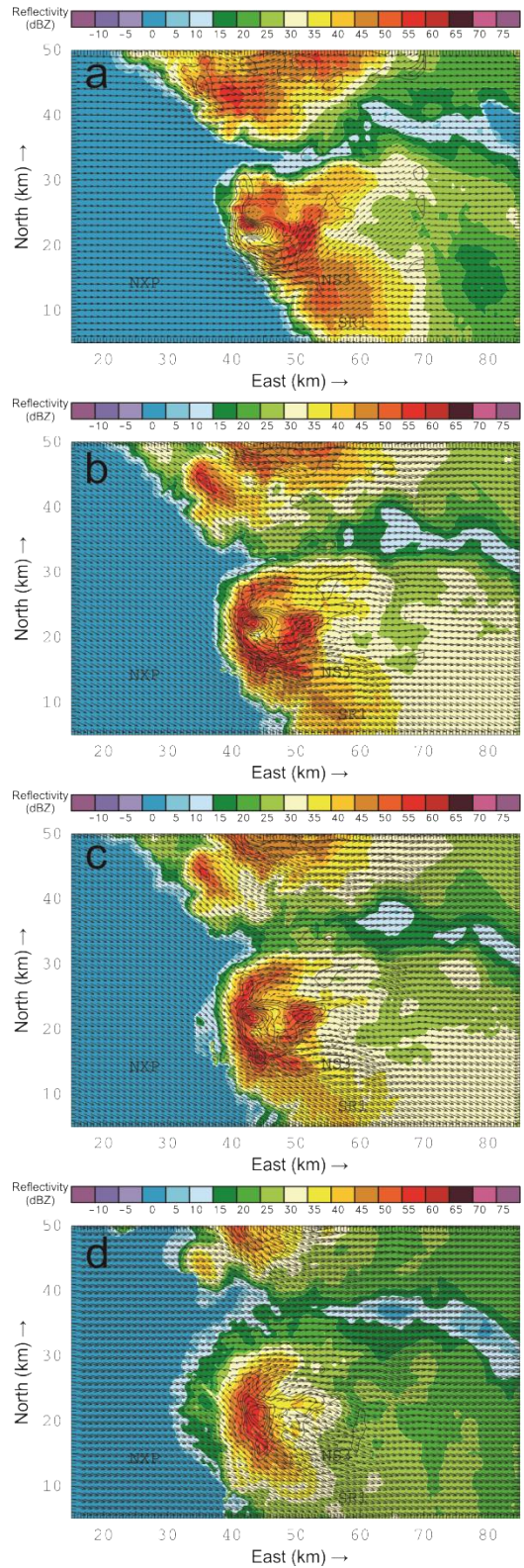
Figure 26. Reflectivity (color shading), updraft strength (contoured from 5 m/s every 5 m/s), and horizontal velocity vectors at a) 5.20 km AGL, b) 8.20 km AGL, c) 9.20 km AGL, and d) 11.70 km AGL at 23:39 UTC.

the hail cores was 10.0 g kg^{-1}, in the central core at an altitude of 1.2 km — the largest

q_g in a secondary core at this altitude, located on the storm's northwest flank, was

delineated by the contour for 6.0 g kg$^{-1} \leq q_g < 7.0$ g kg^{-1}. q_g began to increase again

above the 4.7 km level; the maxima at 4.7 km were concentrated in roughly the same

regions as the hail cores observed at lower altitudes and were within the BWLR and

updraft cores. The highest values of q_g observed above the freezing level were 9.0 g kg^{-1}

at 8.2-8.7 km, just south of the region of high flash density west of the BWLR and the

main updraft core.

The lowest altitude at which cloud ice and snow were detected at this analysis

time (e.g. Figure 28a-e) was 6.2 km, in a small area east of the BLWR, in the region of

lightning dominated by low flash densities and large flash footprints. By the 7.7 km

level, low values of q_x had spread through the eastern anvil and were beginning to

appear in the southern part of the anvil. The maximum q_x values in the main storm core

were 8.0 g kg$^{-1} \leq q_x < 9.0$ g kg^{-1} from 11.7 to 12.7 km, and were concentrated within the

BWLR. The maximum q_x values in the entire domain were 9.0 g kg$^{-1} \leq q_x < 10.0$ g kg^{-1}

from 12.2 km to 13.2 km and were concentrated in the anvil east of the BWLR. The two

flash-dense regions near the BWLR had at least some ice content through most of the

mid-to-upper levels of the storm, but the flash-dense region in the south of the anvil had

no visible ice content except a few pockets of $q_x < 1.0$ g kg^{-1} from 11.7 km to 12.7 km,

which were aligned with the largest flash footprints in that region rather than with the

highest flash densities. The last analysis level containing any ice content was 15.7 km,

where a few pockets of ice were in the storm core (e.g. covering most of the BWLR)

and east of the northern flash-dense region.
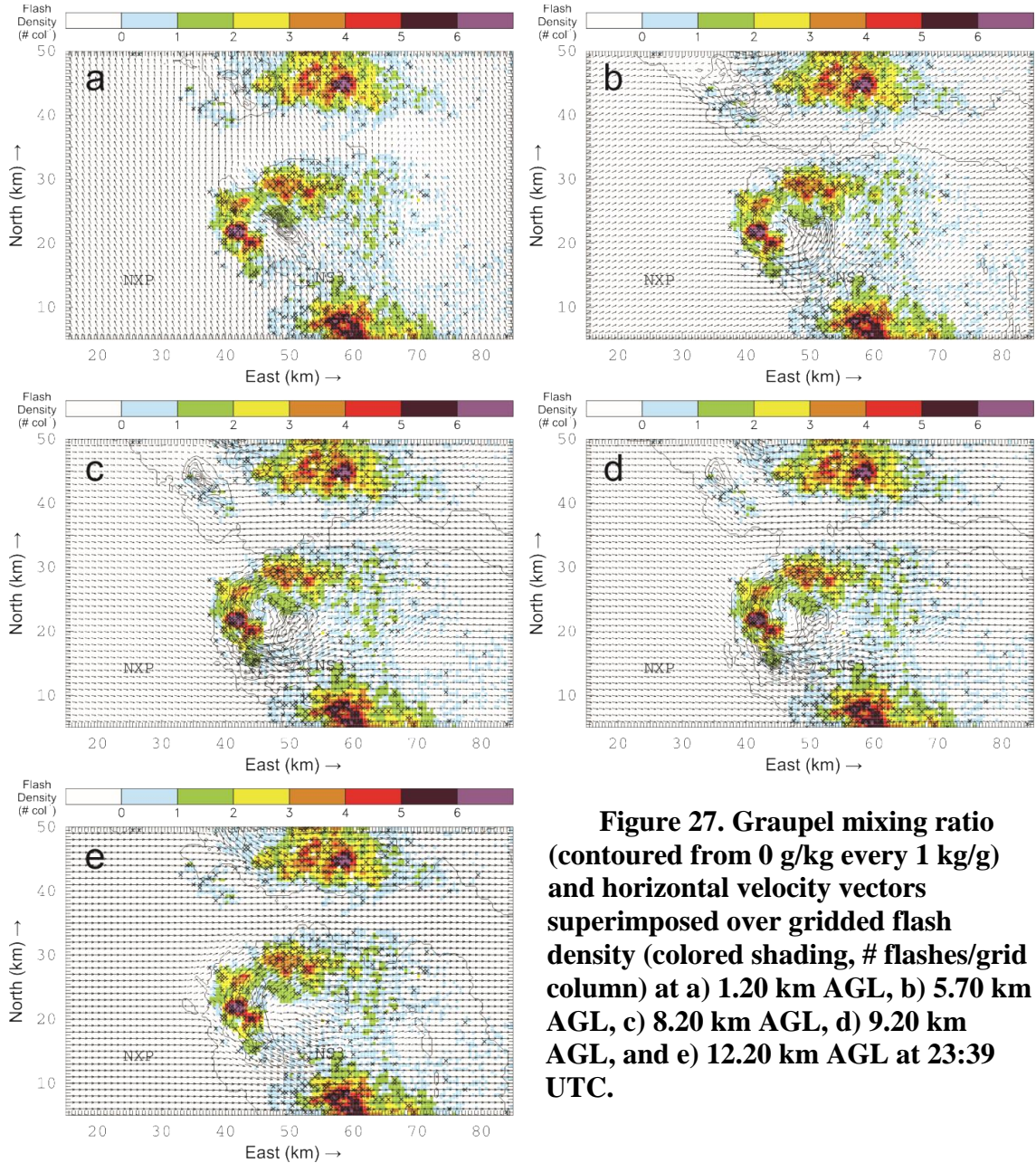
Figure 27. Graupel mixing ratio (contoured from 0 g/kg every 1 kg/g) and horizontal velocity vectors superimposed over gridded flash density (colored shading, # flashes/grid column) at a) 1.20 km AGL, b) 5.70 km AGL, c) 8.20 km AGL, d) 9.20 km AGL, and e) 12.20 km AGL at 23:39 UTC.

Cloud water and rain water existed in every analysis level through 7.2 km (e.g.,

Figs. 29a-c and 30a-c, respectively). Above the freezing level, maximum values of 9.0 g

$kg^{-1} \leq q_c < 10.0$ g kg^{-1} were centered on the western edge of the BWLR at 7.2 km,

coincident with the updraft (e.g., Fig. 32a). At and above 6.2 km, a secondary maximum

in q_c formed east of the BWLR, and extended toward the anvil. The q_r above the

freezing level was found in and west of the BWLR, with a maximum coincident with

62
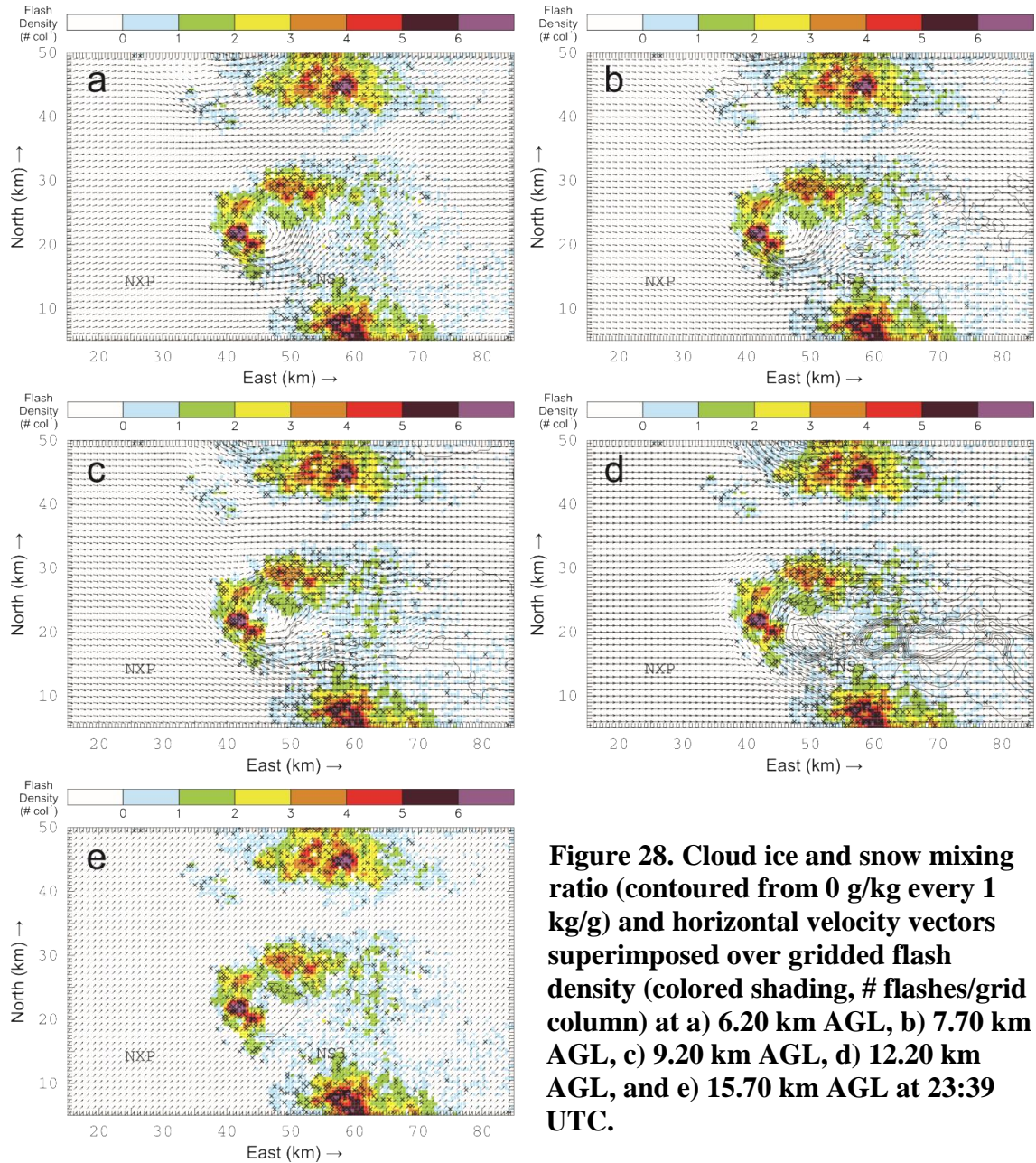
Figure 28. Cloud ice and snow mixing ratio (contoured from 0 g/kg every 1 kg/g) and horizontal velocity vectors superimposed over gridded flash density (colored shading, # flashes/grid column) at a) 6.20 km AGL, b) 7.70 km AGL, c) 9.20 km AGL, d) 12.20 km AGL, and e) 15.70 km AGL at 23:39 UTC.

the updraft from 4.7-6.2 km, with $4.0 \text{ g kg}^{-1} \leq q_r < 5.0 \text{ g kg}^{-1}$ (e.g., Fig. 30a-c). The

presence of so much supercooled liquid water and graupel in the BWLR suggests wet

hail growth processes were occurring there at this analysis time, and wet growth has

been shown to cause BWLRs to form by reducing rebounding collisions and thereby

inhibiting non-inductive charging processes (e.g., Emersic et al. 2011). Since the

mesocyclone was only partially collocated with the BWLR, part of the BWLR's

63
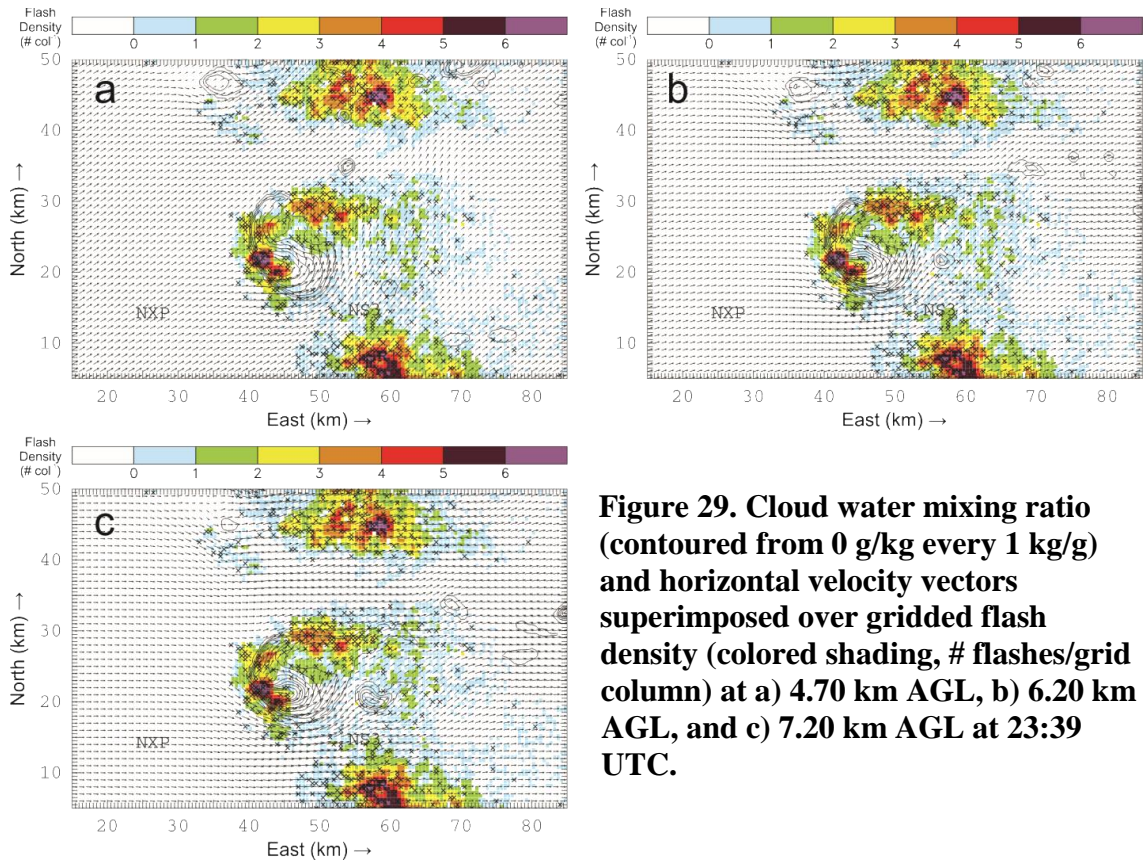
Figure 29. Cloud water mixing ratio (contoured from 0 g/kg every 1 kg/g) and horizontal velocity vectors superimposed over gridded flash density (colored shading, # flashes/grid column) at a) 4.70 km AGL, b) 6.20 km AGL, and c) 7.20 km AGL at 23:39 UTC.

persistence in time probably should be attributed to wet hail growth processes.

West of the BWLR at the 2339 analysis time, the region of highest flash density and VHF source density was within the updraft core (which peaked at $50 \text{ m s}^{-1} \le w < 55 \text{ m s}^{-1}$ from 5.7-8.7 km, e.g., Fig. 31a-b), and flash footprints were small. The inferred charge structure was approximately the same as during the last analysis time: there was a layer of positive charge at ~8-9 km and a layer of negative charge at ~11-12 km (e.g., Fig. 32a). Near the 5-6 km level, there were flashes with odd propagation patterns, with a vertical C-shape similar to what was seen northeast of the BWLR in the 23:21 analysis. The small flashes and portions of flashes propagating through the negative charge at ~12 km tended to be more vertical in extent than horizontal. As with the flashes viewed in the 23:21 analysis time, the relative densities of VHF sources in positive and negative
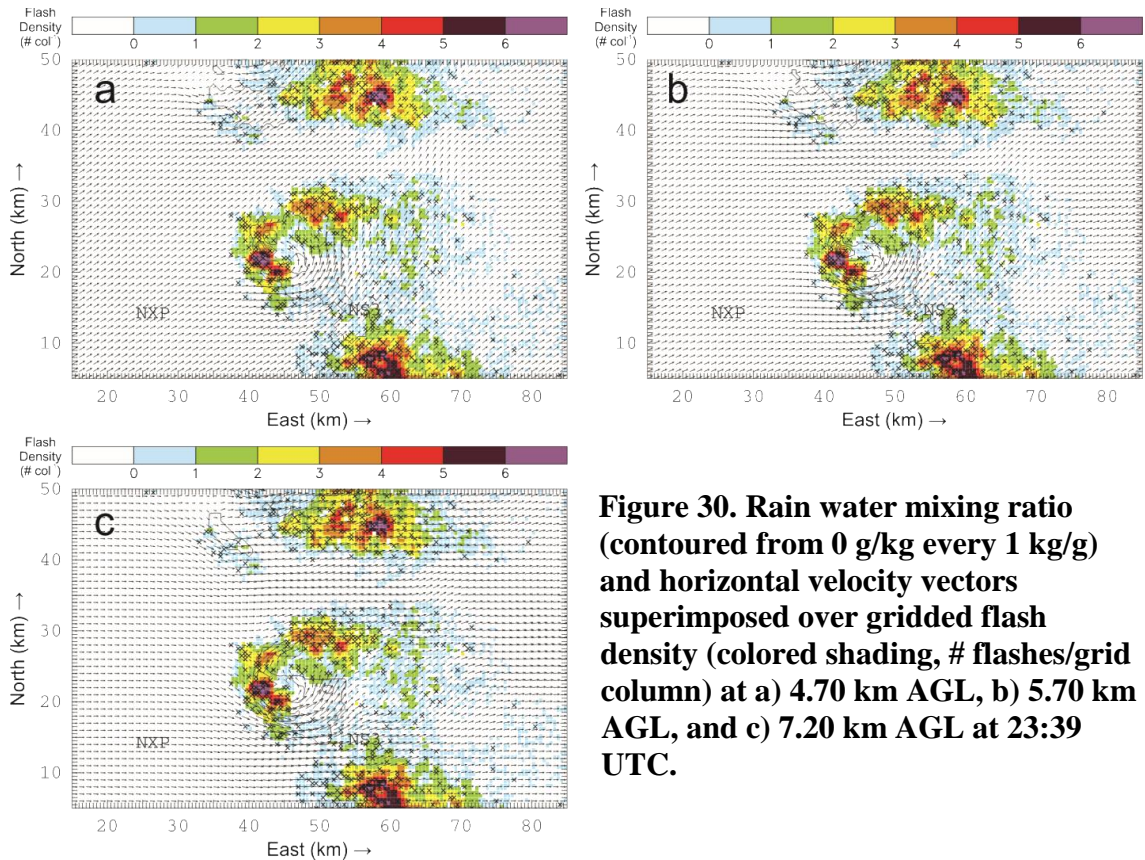
Figure 30. Rain water mixing ratio (contoured from 0 g/kg every 1 kg/g) and horizontal velocity vectors superimposed over gridded flash density (colored shading, # flashes/grid column) at a) 4.70 km AGL, b) 5.70 km AGL, and c) 7.20 km AGL at 23:39 UTC.

charge regions was different from what is usually observed, as the greatest densities were inferred to be in a region of negative charge. The large densities in negative charge were due to recoil streamers propagating back toward positive charge through a compact region of charge. The largely vertical extent of the flashes in this region in particular was due to the presence of the updraft core and the strong updraft gradient surrounding it, as relatively small mapped flashes propagated vertically through relatively small regions of charge near and inside the region of large updraft gradients.

Northeast of the BWLR and updraft, where the flash density maximum had weakened and flash footprints decreased slightly, a positive charge layer was inferred at ~7-9 km closest to the updraft and sloped downward to ~5-6 km toward the north and east; a negative charge layer was inferred at ~10-11 km (e.g., Fig. 32b). Though large
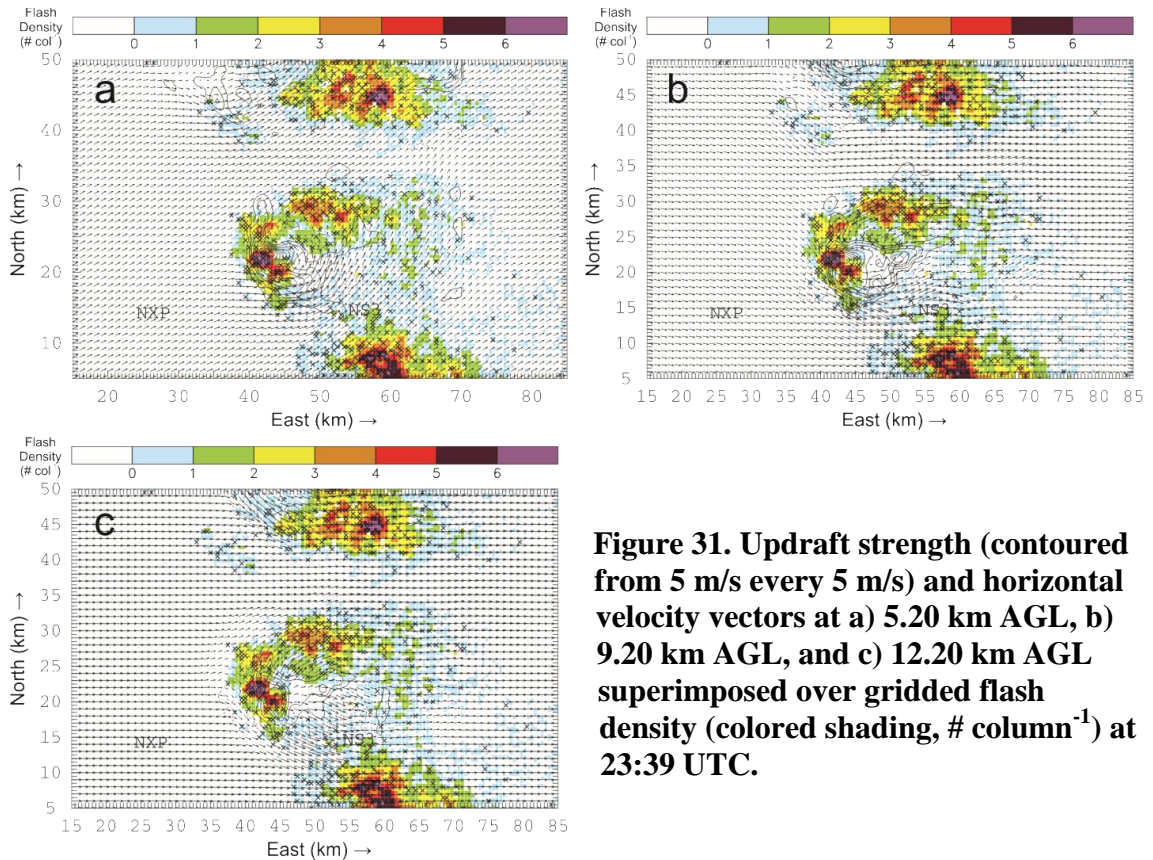
Figure 31. Updraft strength (contoured from 5 m/s every 5 m/s) and horizontal velocity vectors at a) 5.20 km AGL, b) 9.20 km AGL, and c) 12.20 km AGL superimposed over gridded flash density (colored shading, # column^{-1}) at 23:39 UTC.

flashes in this region were very extensive horizontally and were less tortuous (inferred from VHF source densities being relatively small), the flash density maximum also included a region of small flashes with varying propagation patterns. This variation in flash size and behavior was reflected in the variety of footprint sizes seen in Fig. 25a. At the 23:39 analysis time, the charge structure in the anvil remained the same as at the 23:21 analysis time: charge inferred from a vertically bi-layered anvil flash, shown and discussed in more detail in the next section, included a sloped negative charge layer which began at ~8 km and descended to ~5 km to the east, and a positive layer which began at ~12 km and descended to ~10 km as the flash propagated eastward through the anvil.
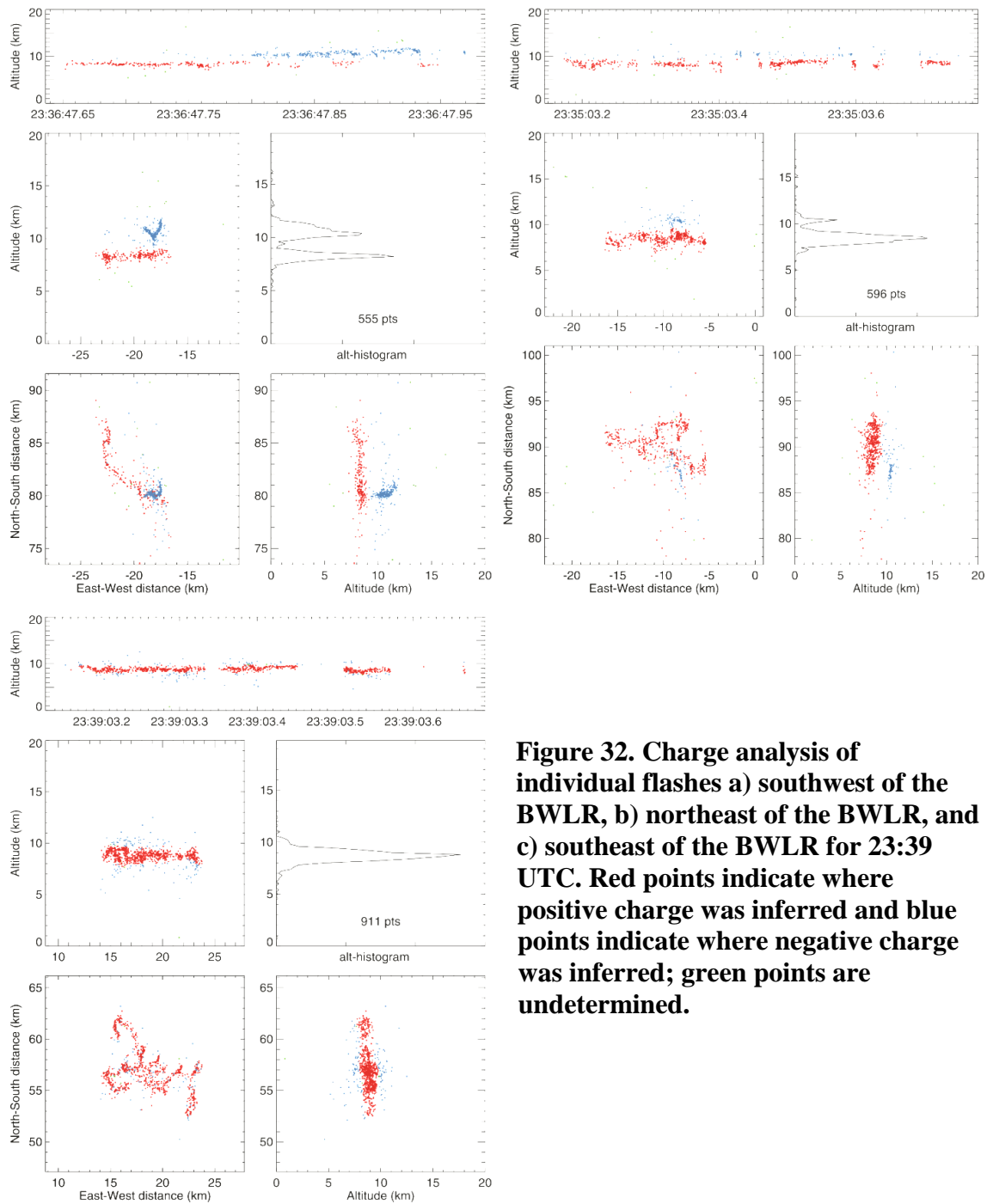
Figure 32. Charge analysis of individual flashes a) southwest of the BWLR, b) northeast of the BWLR, and c) southeast of the BWLR for 23:39 UTC. Red points indicate where positive charge was inferred and blue points indicate where negative charge was inferred; green points are undetermined.

From flashes southeast of the storm core but not in the anvil (where a maximum in flash density at this time was located), a positive charge layer at ~9-10 km (Fig. 32c) and a negative layer at ~12-13 km were inferred. The horizontal areas of flashes in this region were typically extensive and much greater than their vertical extent. As with the 23:21 analysis time, some flashes formed immediately southeast of the BWLR and propagated north and west around it. Overall, the charge layers were far more horizontally extensive in this region of the storm than in and around the updraft.

Another source of information about the storm's charge structure is the vertical distribution of charge density estimated from the balloon-borne EFM data (Fig. 33); of the three DLA analyses, the 23:39 time corresponds most closely to this analysis time. The balloon flew through the eastern flank of the storm, and at least four charge regions were detected: negative charge at and immediately below 6 km; positive charge at ~ 6-6.5 km; a layer of smaller, negative charge density at ~ 7-7.5 km; and more positive charge beginning at ~7.5 km. The balloon was struck by lightning at ~8 km, so no EFM data were available higher than that, though the balloon appeared to move into negative charge as it was struck. These results corroborate some of the charge layers inferred from lightning east and northeast of the BWLR, which were the regions closest to the balloon track. The intrusion of a weak negative layer between two positive layers noted in some of the more complex flash structures appears consistent with the shallow negative layer inferred just above 7 km from the EFM sounding. Note that there were substantial horizontal components to the electric field in this storm (Figure 34), which means that the sounding was at the side of the center of the charge region at that level and the 1-D approximation of Gauss's Law used for charge density calculations is likely
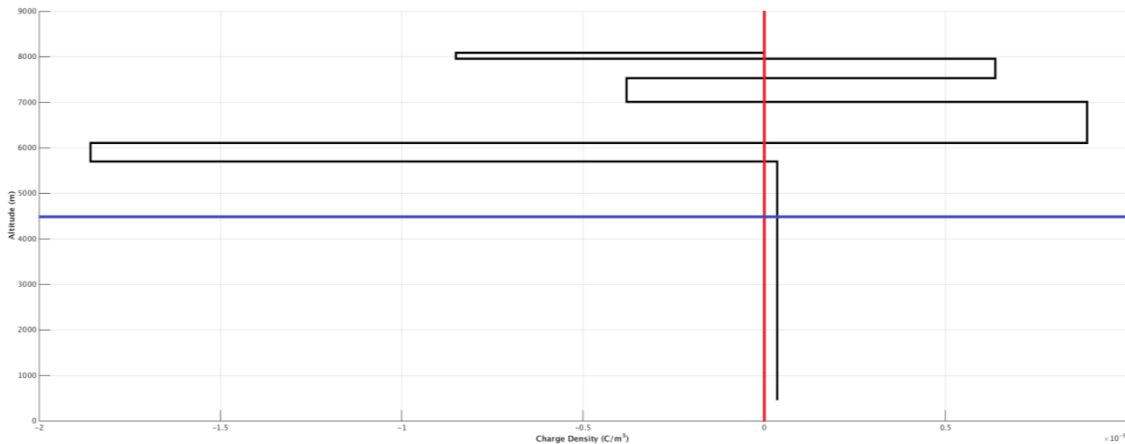
Figure 33. Charge density calculated from the in-situ EFM sounding. The red line denotes the zero line and the blue line denotes the freezing level.

violated (the approximation requires that $\partial E_x/\partial x + \partial E_y/\partial y$ be zero).

It is possible, therefore, that a charge region inferred from some region of electric field gradients was due to approaching or moving away from small localized charge regions, but this source of error becomes increasingly unlikely as the horizontal extent of a charge region increases (Stolzenburg and Marshall 1994). Furthermore, nonzero horizontal electric field components typically have a negligible effect on charge density values when the balloon is actually within a charge region.

As with the 23:21 analysis time, most of the storm's graupel content was concentrated in the updraft region in and southwest of the BWLR, extending from the middle to upper levels of the storm (Fig. 27). There was much more cloud water concentrated in this region at the 23:39 analysis time, although inferred ice crystal content was still minimal; these circumstances, combined with the similarity in flash structure and behavior, suggest that the charging mechanisms at work and the resultant charge separation patterns were much the same as at 23:21.
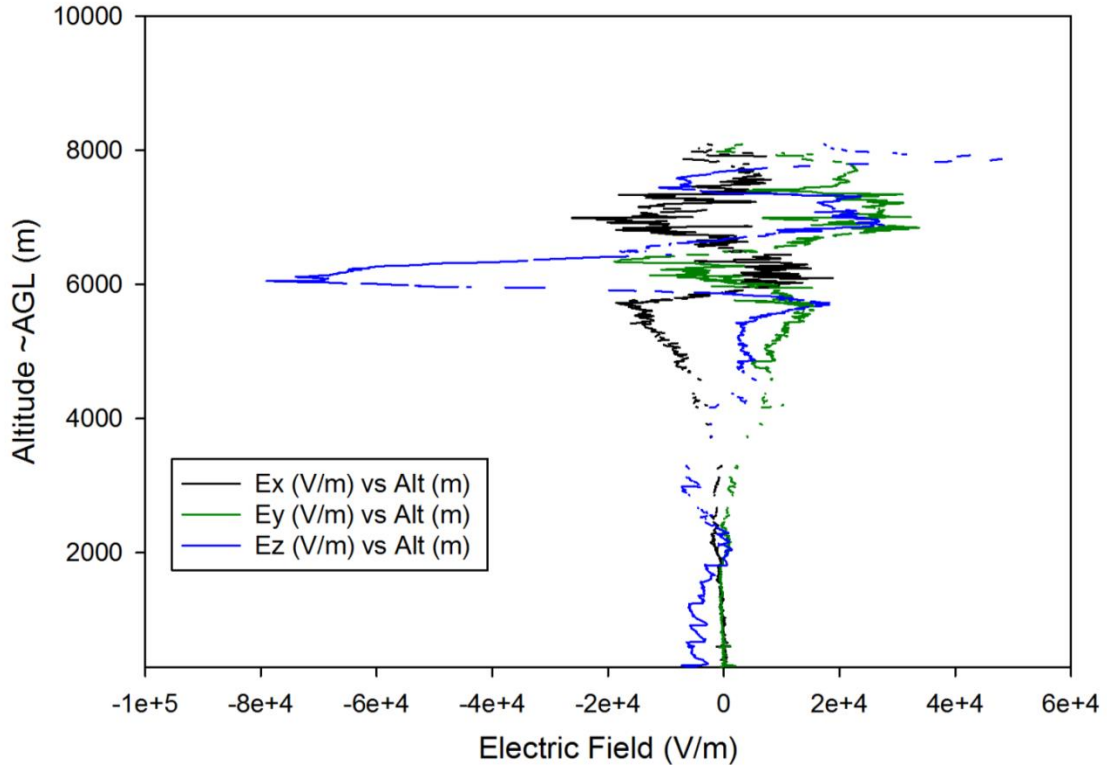
Figure 34. Horizontal and vertical components of electric field as measured by the in-situ EFM sounding launched at 23:23 UTC.

Northeast of the BWLR, the appearance of more small, tortuous flashes indicates that the region's general charge structure had changed somewhat from the structure inferred at 23:21. The microphysical and kinematic structure of this part of the storm also changed from 23:21 to 23:39 (compare Figs. 17-20 and 27-30): the ice crystal and cloud water contents both decreased, and a downdraft region developed adjacent to very weak pockets of updraft (weaker than the updraft present at 23:21). The location of the downdraft, on the northern and western edge of the high flash densities in this region, was also the primary location of the smaller, more vertically extensive flashes having higher VHF source densities (probably due to greater channel tortuosity), whereas the larger, more horizontally extensive flashes occurred slightly farther south and east. This gradient in horizontal extent was also evident in the mean flash footprints

70

across the region at this time. There may have been a small amount of active noninductive charging, given the presence of weak updrafts, but the weak updrafts and small ice crystal and cloud water contents here mean most of the charge was likely centrifuged, fountained, and/or advected into this region from the main updraft core, and separated via sedimentation.

At the 23:39 analysis time, as with 23:21, the DLA diagnosed little graupel content, less ice crystal content, and no cloud water content in the mid-to-upper levels of the southeast portion of the storm in spite of enough reflectivity to indicate that there were many hydrometeors present (see Figs. 16-19 and 26-29). Those hydrometeors were most likely ice crystals and snow, however. The inferred charge structure and the types of flashes evident in this region of the storm were unchanged from 23:21, implying that the sources of charge are also unchanged.

3.2.3 Radar and lightning analyses and DLA (00:00 UTC)

The cluster of high flash densities on the western edge of the BWLR had dissipated somewhat by 00:00 UTC, while the region of high flash densities on the northern edge of the storm had regenerated (Figs. 35a-c). The BWLR was larger and less distinct at this time than previously. The southern and eastern anvil regions of the storm had moved out of the analysis domain by this time, so there was no distinctive area of high flash densities in the anvil. The storm was dominated by flash densities of 1-2 flashes per grid column at this analysis time. At 9.2 km, there were three updraft cores; the strongest had an oblong shape and was located in the remnants of high flash densities on the west side of the BWLR. Its maximum speed through the whole vertical extent of the storm was $50 \text{ m s}^{-1} \leq w < 55 \text{ m s}^{-1}$, and that updraft speed was sustained
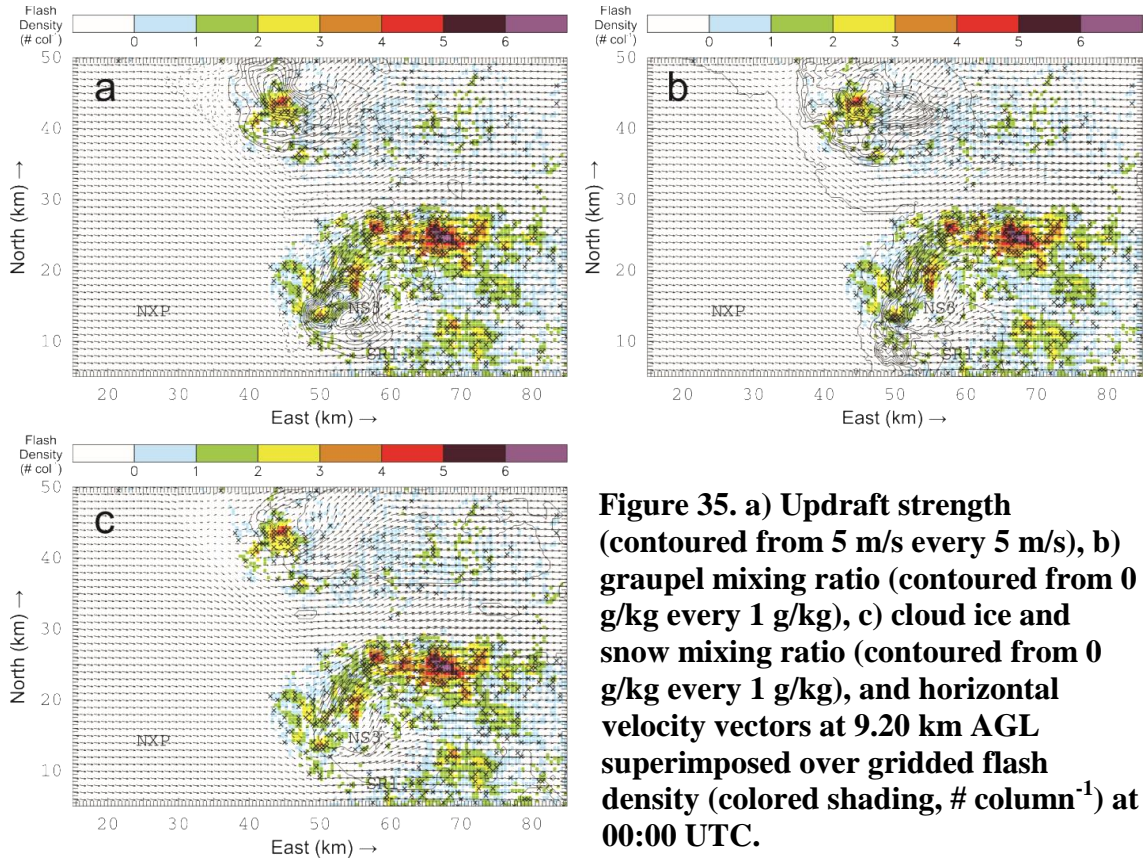
Figure 35. a) Updraft strength (contoured from 5 m/s every 5 m/s), b) graupel mixing ratio (contoured from 0 g/kg every 1 g/kg), c) cloud ice and snow mixing ratio (contoured from 0 g/kg every 1 g/kg), and horizontal velocity vectors at 9.20 km AGL superimposed over gridded flash density (colored shading, # column^{-1}) at 00:00 UTC.

from 7.2 to 9.2 km (e.g., Figs. 35a, 36b). At altitudes between 0.7 km and 11.2 km there were multiple updraft cores, sometimes as many as four, of varying strengths (e.g., Fig. 36a-b), though above 11.2 km the updraft narrowed into one core (Fig. 36c). The two secondary updraft cores at 9.2 km with a maximum of 30 m s$^{-1} \leq$ w $<$ 35 m s^{-1} were collocated with the western half of the BWLR and contained a few flashes. Note also that at this time, the horizontal updraft gradients were larger than at previous times. Almost the entire storm had diagnosed graupel content at 9.2 km, but all values $\geq$ 1.0 g kg^{-1} were west of the BWLR, with a maximum 10.0 g kg$^{-1} \leq$ q$_g <$ 11.0 g kg^{-1} centered on a small cluster of relatively high flash densities (4 flashes/grid cell; see Fig. 36b). Snow and cloud ice mixing ratios were low (q$_x <$ 1.0 g kg^{-1}) at this altitude, but covered most of the northern flash-dense region and covered parts of the storm east and west of

Figure 36. Updraft strength (contoured from 5 m/s every 5 m/s) and horizontal velocity vectors at a) 4.20 km AGL, b) 7.20 km AGL, and c) 12.20 km AGL superimposed over gridded flash density (colored shading, # column^{-1}) at 00:00 UTC.

the BWLR (Fig. 36c).

The 00:00 UTC analysis time had small flash footprints (< 25 km^2) distributed throughout all parts of the storm within the domain (Fig. 37a). Within the updraft cores and on the edges of the storm, flash footprints were very small (< 8 km^2), but elsewhere they were larger, primarily ≥ 8 km^2 with scattered areas ≥ 25 km^2. The previously noted area of maximum q_g at 9.2 km was collocated with the region of small flash footprints. The region of highest flash density on the northern edge of the storm contained flashes that were all ≥ 8 km^2, approximately half of which were ≥ 25 km^2. Some of the flashes in that region had footprints ≥ 50 km^2; these larger sizes were also seen scattered through the small portion of anvil visible in this analysis. A single square of footprint size ≥ 200 km^2 existed in the bottom-rightmost grid cell of the analysis domain, which
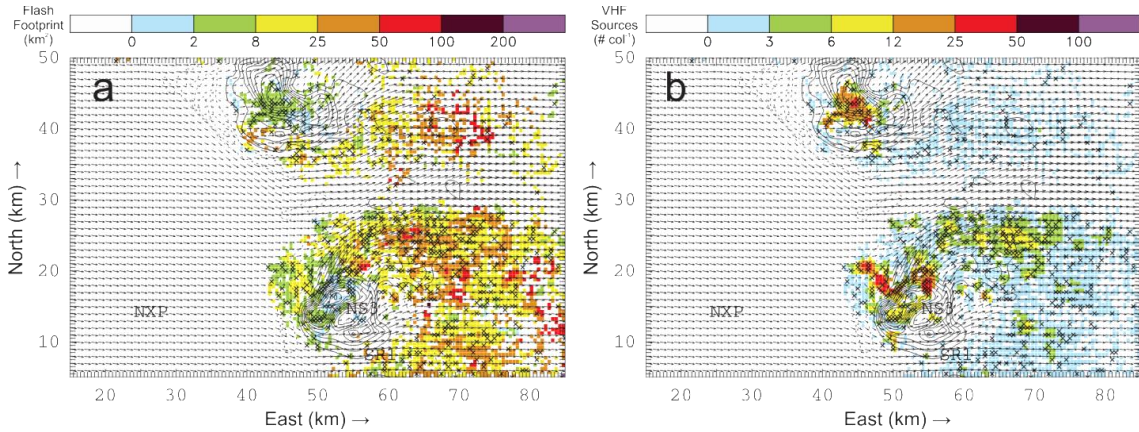
Figure 37. Updraft strength (contoured from 5 m/s every 5 m/s) and horizontal velocity vectors at 9.20 km AGL superimposed over a) gridded flash footprint area (colored shading, km^2 column^{-1}) and b) VHF source density (colored shading, # column^{-1}) at 00:00 UTC.

suggested that the largest flashes to be found in the storm at this time were anvil flashes mostly outside the domain.

As observed in the other two analysis times, flash initiations tended to cluster in the regions of high flash densities at 00:00 UTC (Figs. 35 and 36). There were many initiations throughout the flash density maximum north of the BWLR and in pockets throughout the eastern part of the storm. The most compact clusters of flash initiations, however, were in the pockets of higher flash densities west of the BWLR, in and around the primary updraft core and q_g maxima at 9.2 km.

The VHF source densities at 00:00 UTC were < 10 sources per grid cell over most of the storm's horizontal extent (Fig. 37b), with many grid cells throughout the storm having < 5 sources per grid cell. The flash-dense region on the northern edge of the storm had a relative maximum of up to 20 sources per grid cell. The maximum VHF source densities were located near the updraft, where there were pockets of ≥ 30 sources per grid cell collocated with relatively high flash densities and smaller mean flash footprints than in the rest of the storm.

74

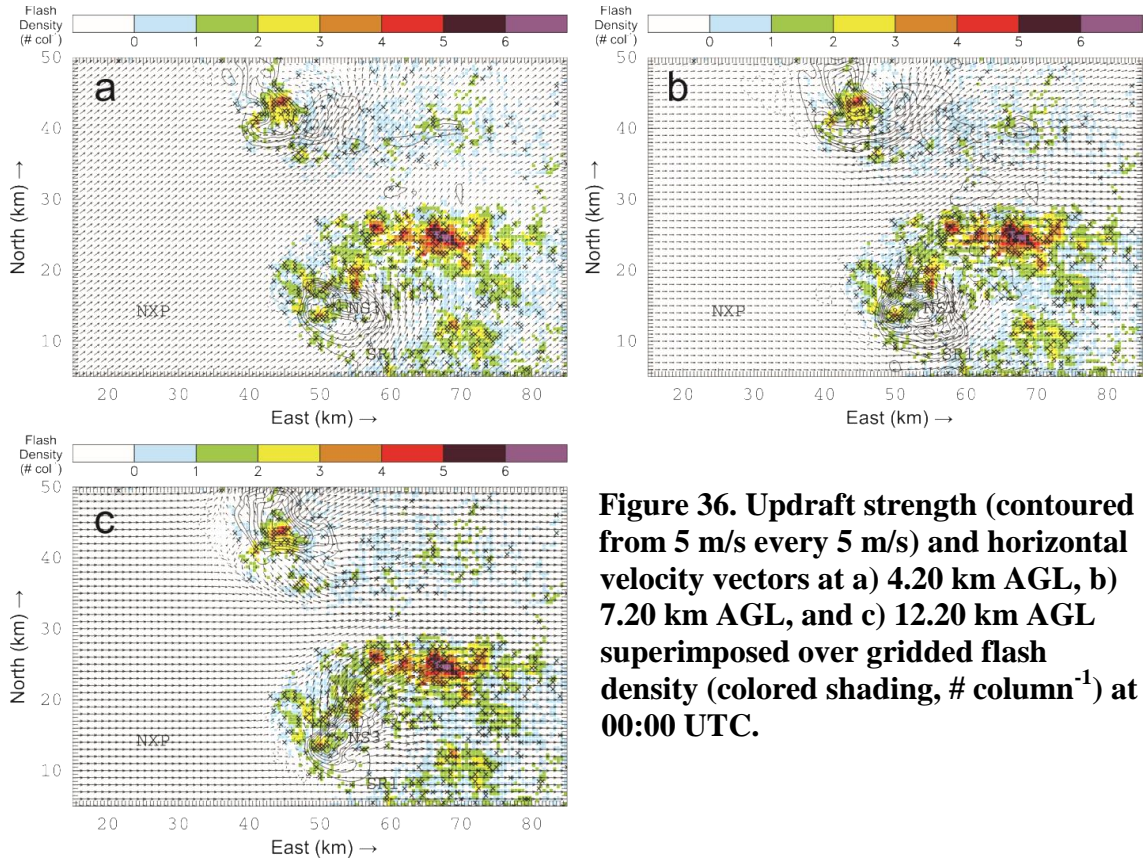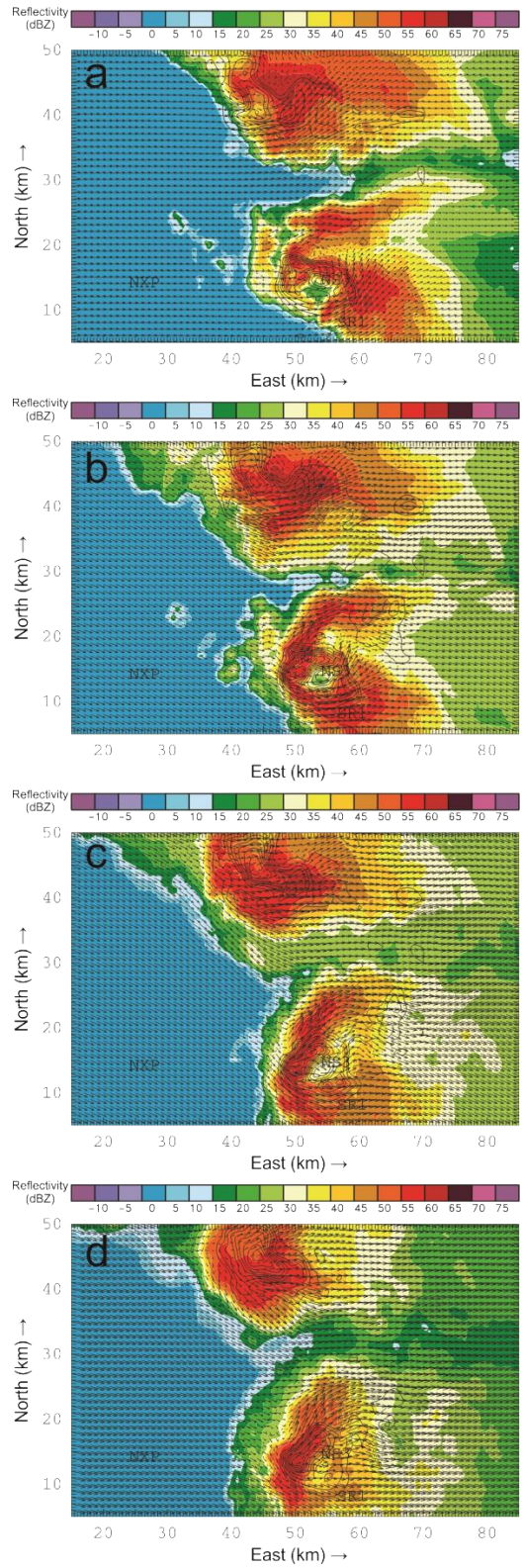**Figure 38. Reflectivity (color shading), updraft strength (contoured from 5 m/s every 5 m/s), and horizontal velocity vectors at a) 4.70 km AGL, b) 7.20 km AGL, c) 9.20 km AGL, and d) 11.20 km AGL at 23:39 UTC.**

At 00:00 UTC, the lowest altitude at which some of the bounding reflectivities of a BWER were apparent was 3.7 km. By 4.7 km, the BWER was completely bounded and had tilted slightly northward (Fig. 38a). The BWER was coincident with the western portion of the BWLR and with an updraft core (Fig. 38b-c) through much of the depth of the storm until it could no longer be detected at 11.2 km (Fig. 38d).

Graupel mixing ratios persisted through 00:00 UTC from 0.2 km (with a small low-level maximum $q_g \geq 4.0$ g kg^{-1}) through 1.2 km near the storm's western flank which likely indicates a hail core (Fig. 39a). Graupel mixing ratios again exceeded 4.0 g kg^{-1} at 4.2 km, and continued to increase with height above the freezing level through 4.50 km (Fig. 39b-e). Graupel was diagnosed throughout the storm above the freezing level, although the highest values for q_g were diagnosed within, west, and northwest of the BWLR. The maximum value of q_g was 11.0 g kg^{-1} $\leq q_g < 12.0$ g kg^{-1} at an altitude of 7.2 km (approximately the -20°C level) to the northwest of the BWLR. The maximum value at 9.2 – 9.7 km was 10.0 g kg^{-1} $\leq q_g < 11.0$ g kg^{-1}, slightly to the south of the 7.2 km maximum. The highest analysis level at which the DLA estimated appreciable graupel mixing ratios was 15.7 km.

As in the 23:39 analysis, the lowest altitude at which q_x was found at 00:00 UTC was 6.2 km AGL in a small pocket east of the northern flash density maximum (Fig. 40a). The areal extent of q_x expanded with increasing altitude and predominantly low q_x values eventually spanned most of the grid cells containing the Kingfisher storm's lightning (Fig. 40b-e). The eastern edges of the contours extended beyond the analysis domain, consistent with ice content pervading the broader eastern anvil. The maximum q_x at any altitude was 6.0 g kg^{-1} $\leq q_x < 7.0$ g kg^{-1} at 11.2-11.7 km, and the maximum
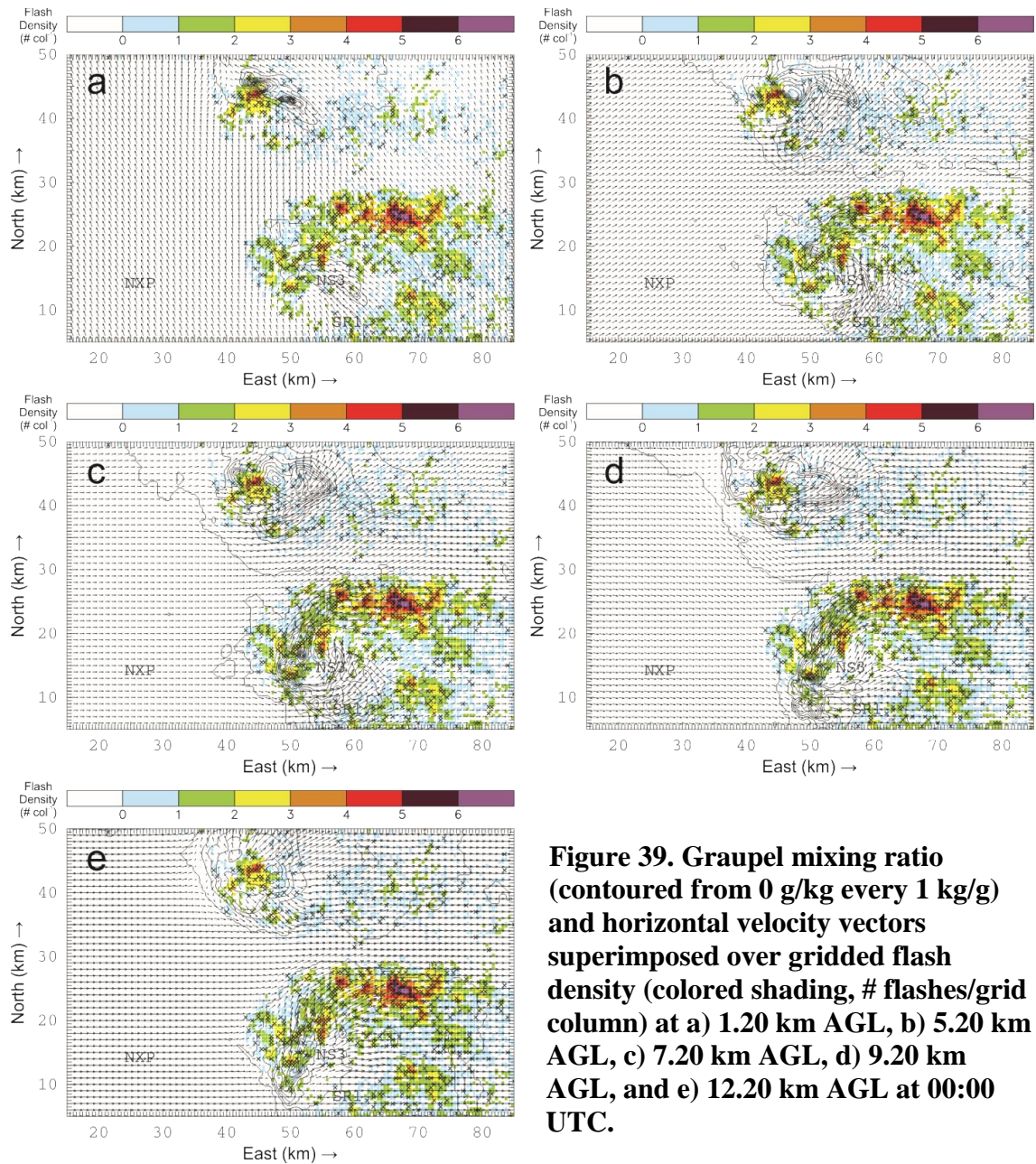
Figure 39. Graupel mixing ratio (contoured from 0 g/kg every 1 kg/g) and horizontal velocity vectors superimposed over gridded flash density (colored shading, # flashes/grid column) at a) 1.20 km AGL, b) 5.20 km AGL, c) 7.20 km AGL, d) 9.20 km AGL, and e) 12.20 km AGL at 00:00 UTC.

was collocated with the BWLR at this level. The maximum altitude with any quantity of ice was 16.2 km due to the overshooting top. For the most part, the ice was concentrated on the eastern side of the storm core and (presumably) into the anvil.

Cloud water and rain water content was persistently analyzed from the surface through 7.2 km in the Kingfisher storm (Fig. 41a-c and 42a-c, respectively). There was
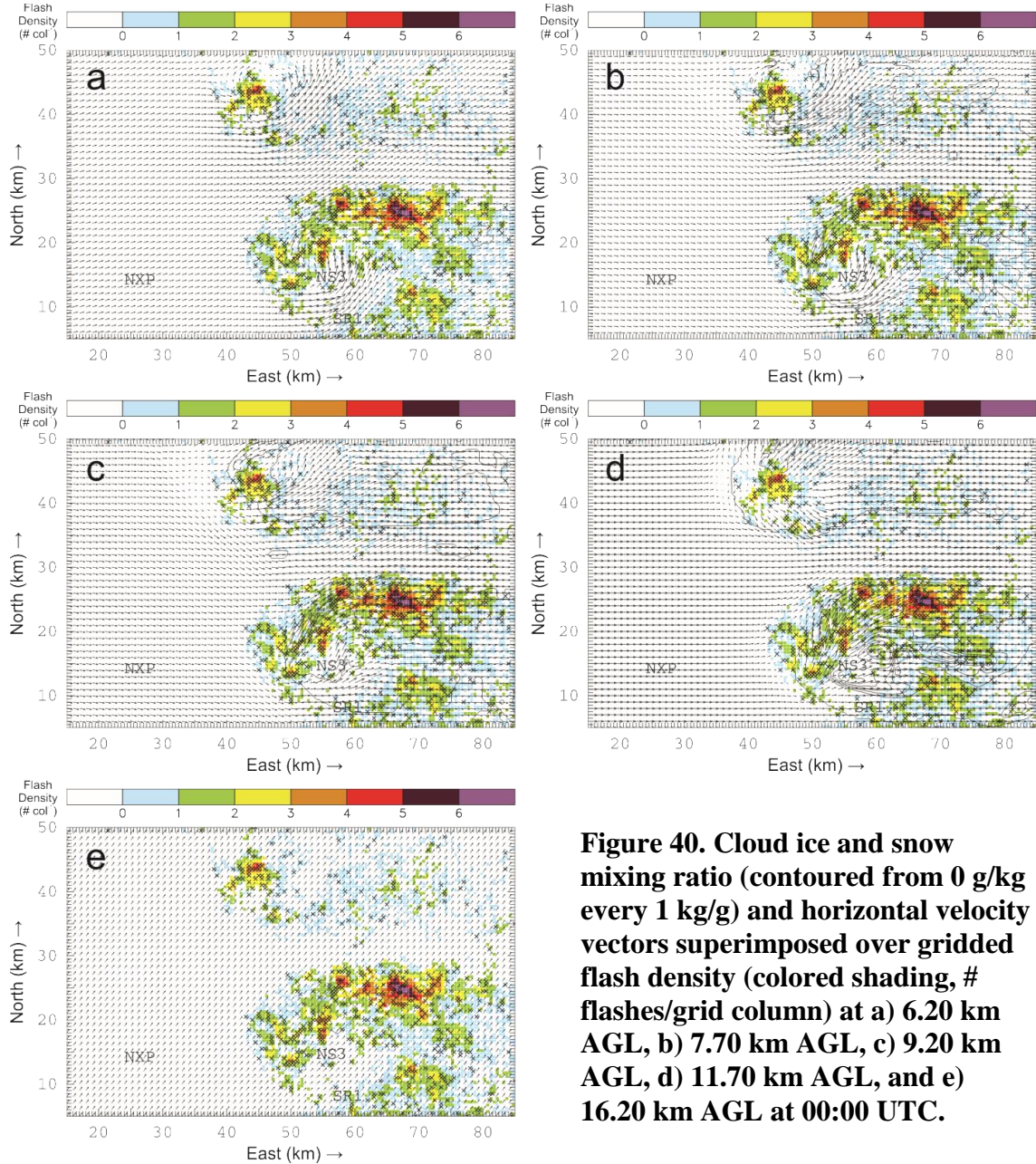
Figure 40. Cloud ice and snow mixing ratio (contoured from 0 g/kg every 1 kg/g) and horizontal velocity vectors superimposed over gridded flash density (colored shading, # flashes/grid column) at a) 6.20 km AGL, b) 7.70 km AGL, c) 9.20 km AGL, d) 11.70 km AGL, and e) 16.20 km AGL at 00:00 UTC.

a maximum q_r of 5.0 g kg^{-1} $\leq q_r < 6.0$ g kg^{-1} from 4.2-5.7 km that was composed partially of supercooled liquid (the freezing level ranged from ~4.1 km to ~ 5.2 km; e.g., Fig. 5). Above the freezing level, most of the supercooled rain water was confined within the main updraft region of relatively high flash densities and small flash footprints west of and within the BWLR. The maximum cloud water content was 10.0 g
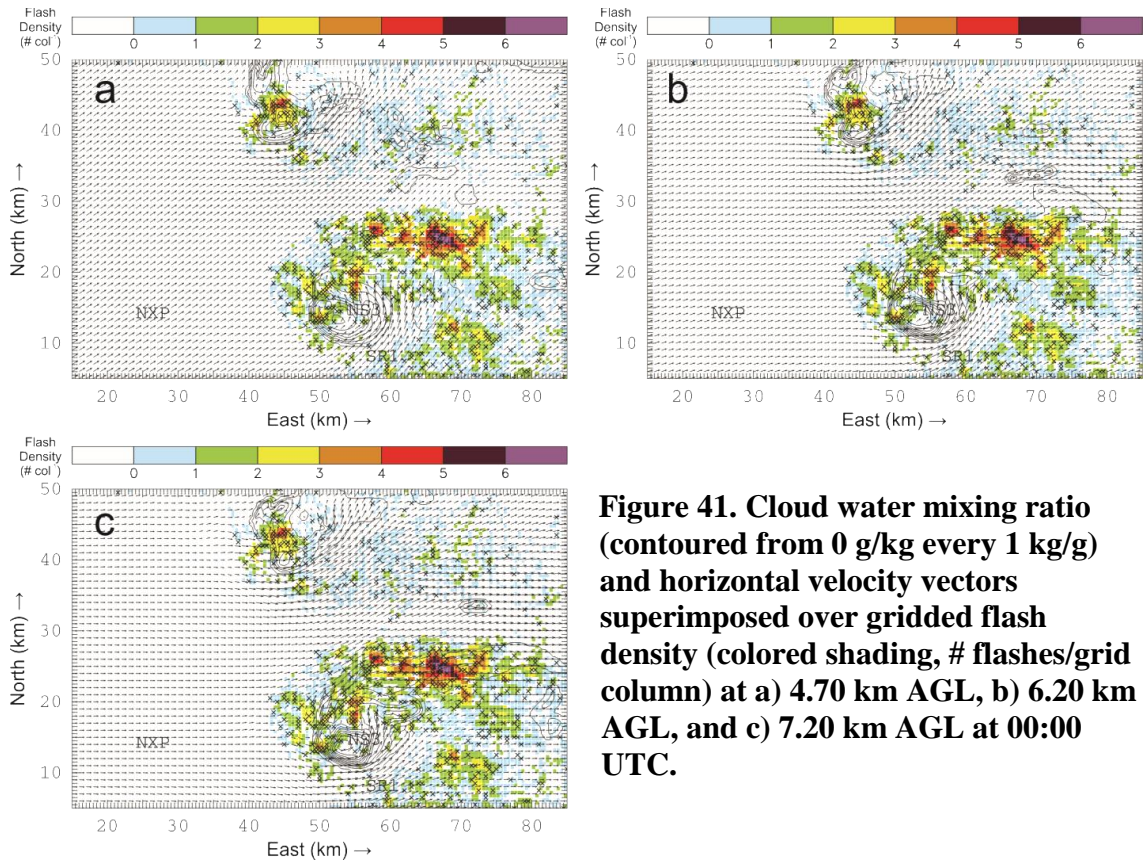
Figure 41. Cloud water mixing ratio (contoured from 0 g/kg every 1 kg/g) and horizontal velocity vectors superimposed over gridded flash density (colored shading, # flashes/grid column) at a) 4.70 km AGL, b) 6.20 km AGL, and c) 7.20 km AGL at 00:00 UTC.

kg^{-1} ≤ q$_c$ < 11.0 g kg^{-1}, between 6.7-7.2 km. Most of the cloud water content was

contained within the BWLR and the region of small flashes on its western flank, within

the updraft. There was little rain water content coincident with the flash density

maximum on the northern edge of the storm, though cloud liquid water does extend into

that region throughout most analysis heights through -20°C or 7.2 km, at which the

maximum value of q$_c$ was 1.0 g kg^{-1} ≤ q$_c$ < 2.0 g kg^{-1}.

At the 00:00 UTC analysis time, the flash density signatures were quite different

than those in the other two analysis times. However, the VHF source density maximum

remained close to its original storm-relative location, having shifted from southwest of

the BWLR to west of it. The maximum VHF source density was just outside updraft

cores and near large horizontal gradients in updraft speeds (Fig. 37b). Layers of positive

79
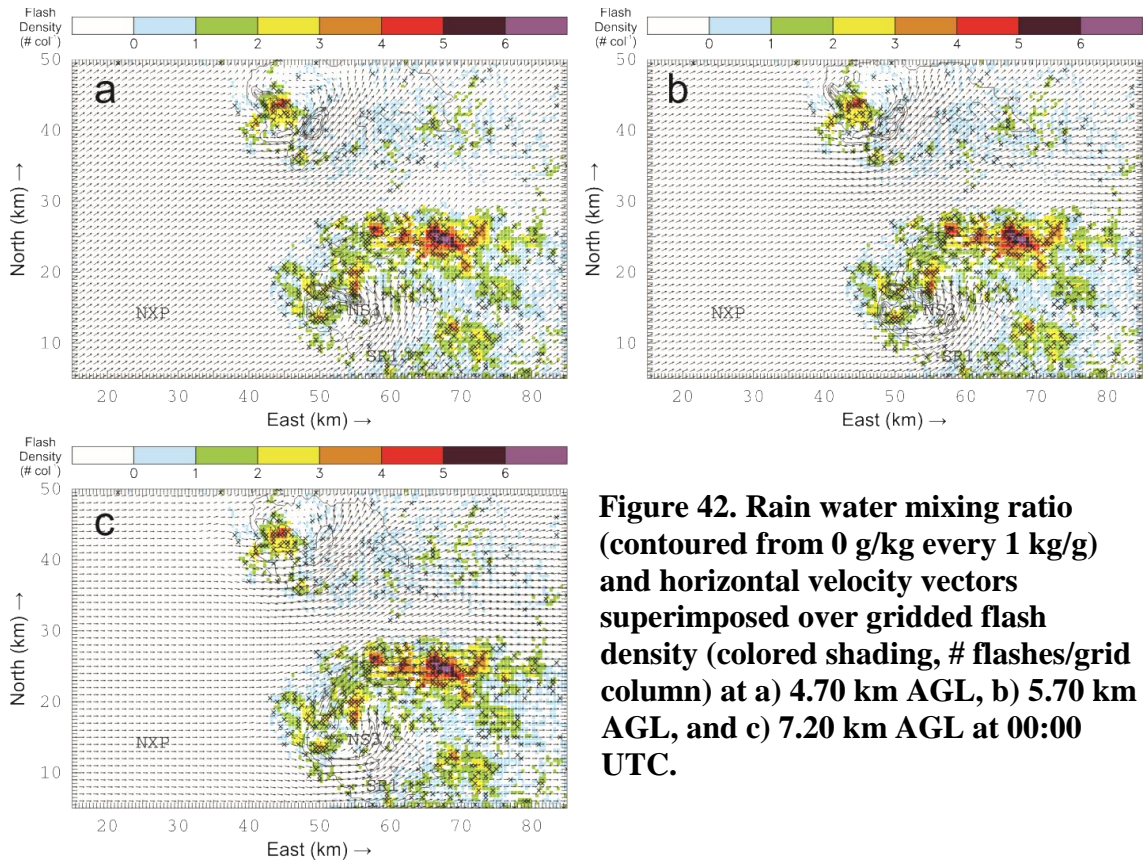
Figure 42. Rain water mixing ratio (contoured from 0 g/kg every 1 kg/g) and horizontal velocity vectors superimposed over gridded flash density (colored shading, # flashes/grid column) at a) 4.70 km AGL, b) 5.70 km AGL, and c) 7.20 km AGL at 00:00 UTC.

charge were inferred at ~ 4-6 km and ~ 8-10 km from lightning flashes in this part of the storm (west of the BWLR), possibly with a small layer of negative charge between them (not shown), and a negative region was inferred at ~11-12 km (e.g., Fig. 43a). The positive charge region located at ~ 8-10 km west of the BWLR sloped downward to ~ 6-7 km as flashes propagated south of the BWLR, and some of the flashes south of the BWLR were inferred to have involved a pocket of negative charge above that layer, at ~ 9-10 km. Analyses of flashes propagating from the southeast to the south of the BWLR also indicated downward sloping negatively charged layers and corroborated the existence of positive charge at ~ 6-7 km and negative charge above it.

Additionally, in the region having a maximum in VHF source density maximum west of the BWLR in the gridded data, an elevated region of continual point discharges

(up to ~15-16 km within the overshooting top) became easily distinguishable in the raw LMA data beginning at ~ 00:03 UTC (e.g., Fig. 11). These discharges did not form any distinct flashes themselves, nor were they linked with lightning flashes occurring at lower altitudes. Lightning discharges in the overshooting tops of thunderstorms have been discussed in other studies (e.g., Lhermitte and Krehbiel 1979; Krehbiel et al. 2000; Bruning et al. 2010; Emersic et al. 2011). The present 29-30 May DC3 case most resembles that described by Emersic et al. (2011) and Calhoun et al. (2013), since it was a region of continuous point discharges rather than very high-altitude flashes. Calhoun et al. (2013) pointed out that a contributing factor for these discharges may have been that the rapidly decreasing threshold of electric field strength required for flash initiation with altitude (e.g., Marshall et al. 1995, 2005) due to the decreasing density of air (Calhoun et al. 2013). This elevated maximum in VHF source density was above and west of the BWLR and BWER, rather than directly above them as found by Calhoun et al. (2013), but it was coincident with the storm's updraft according to the triple-Doppler analysis at 00:00 UTC.

Given the lack of flash structure in the point discharges, it was impossible to directly infer from mapped lightning the polarity of charge transported into the overshooting top from below. The conceptual model of storm electrification (e.g., MacGorman and Rust 1998) is that charge produced by non-inductive processes in the updraft would be lofted to upper regions of the storm, in this case into the overshooting top as high as 15-16 km. Very small graupel and ice crystal mixing ratios were present in the overshooting top according to the DLA, and they were likely the charge carriers from the updraft. Because negative leaders radiate more strongly than positive leaders

81
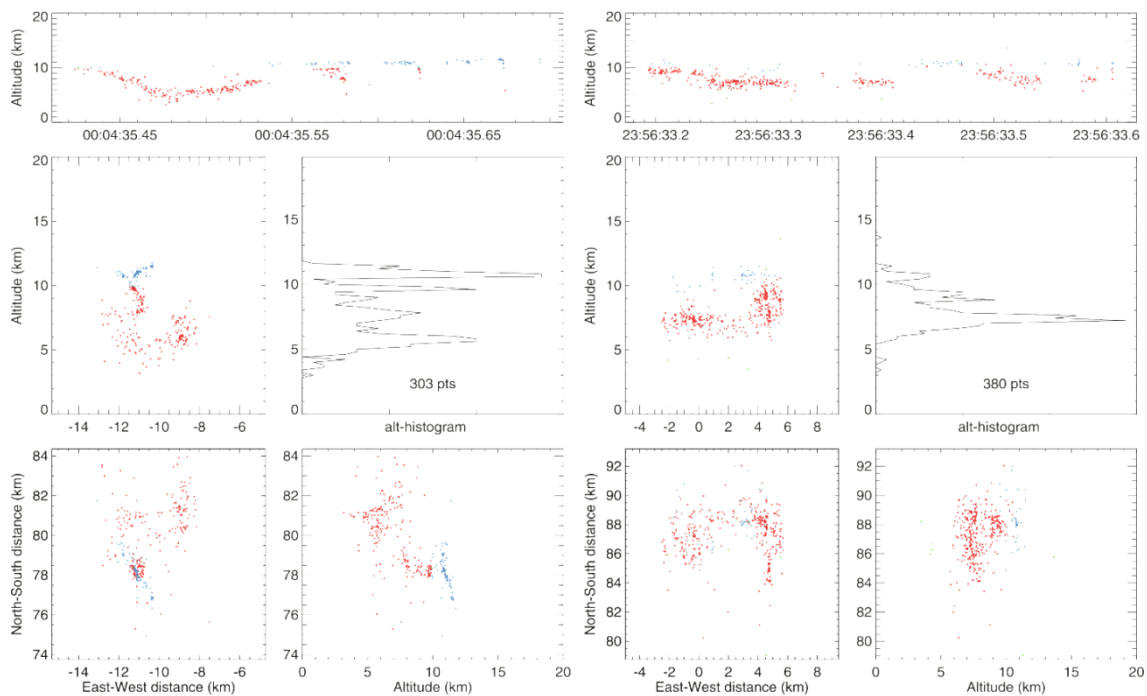
Figure 43. Charge analysis of individual flashes a) southwest of the BWLR and b) northeast of the BWLR for 00:00 UTC. Red points indicate where positive charge was inferred and blue points indicate where negative charge was inferred; green points are undetermined.

and tend to propagate in positive charge, the existence of VHF sources suggests that positive charge was likely involved in the flashes, but negative charge would likely also have been needed nearby to create the electric field magnitudes necessary to initiate discharges, although the signals radiated in the negative charge regions probably were usually too weak to be detected.

Emersic et al. (2011) and Calhoun et al. (2013) suggested that the lofted particles carried positive charge from the large positive charge region typically found in upper regions of storms, and this positive charge then interacted with charge from a negative screening layer which formed at the cloud boundary to produce the discharges. The uppermost polarity of charge inferred from lightning near the updraft core of the

Kingfisher storm suggests an alternative possibility: The charge produced on cloud ice particles interacting with graupel in strong updrafts, where liquid water concentrations would have been large, appears from the lightning structure to have been negative, consistent with the results of laboratory experiments studying non-inductive charging in the presence of large liquid water contents. The polarity of charge lofted into the overshooting top then would be negative, with the screening layer charge being positive.

North and northeast of the BWLR, where the flash density maximum was at this time, flash structures were still a mixture of large, horizontally extensive flashes and small, vertically extensive flashes. A positive charge region was inferred at ~ 6-10 km and a negative charge region at ~10-12 km (Fig. 43b). The positive charge region also sloped downward toward the north, and there may have been another negative charge region beneath it. Smaller, more vertically extensive flashes corroborated the charge structure inferred from more horizontally extensive flashes.

Though the southeast part of the storm was outside the DLA domain at this time, the existence of frequent and extensive lightning in that region implies that localized charge separation was occurring there. However, cloud ice mixing ratios less than 1 g kg^{-1} and graupel mixing ratios much greater than 1 g kg^{-1} were analyzed in the southeastern anvil along the southern edge of the DLA domain (Figs. 39-40). Given likely horizontal hydrometeor advection out of the DLA domain with diverging anvil outflow, the in situ charge separation process may thus have been influenced by horizontal charge advection from the convective region combined with gradual differential sedimentation of opposite-sign cloud ice and graupel charges (e.g., Ziegler
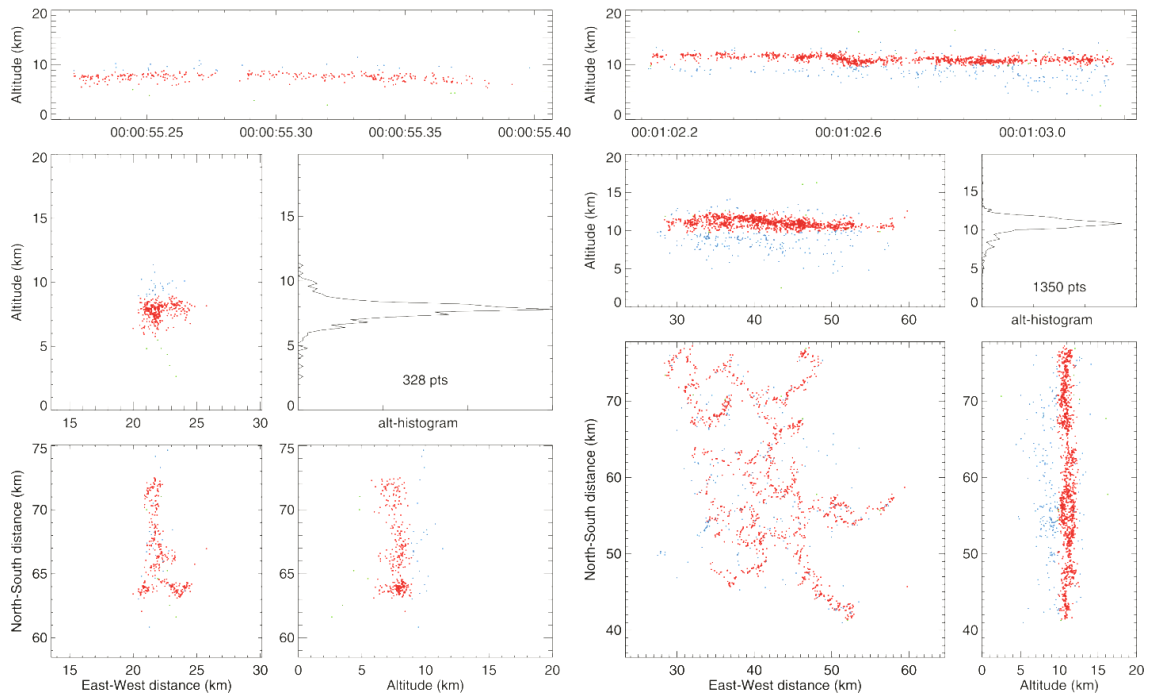
Figure 44. Charge analysis of two adjacent flashes southeast of the BWLR at 00:00 UTC: (a) depicts the more western flash and (b) depicts the more eastern flash, which extends partly into the anvil. Red points indicate where positive charge was inferred and blue points indicate where negative charge was inferred; green points are undetermined.

and MacGorman 1994; Byrne et al. 1989). The analysis of the southeast region's lightning structure indicates that it had several charge layers. Flashes closer to the storm reflectivity core depicted a layer of positive charge at ~ 6-8 km and a negative layer at ~ 9-11 km (e.g., Fig. 44a), whereas flashes in an adjacent region slightly farther to the east were inferred to have negative charge at ~ 6-9 km, with positive charge at ~10-12 km, and another small negative layer (possibly a screening layer) at ~13 km (e.g., Fig. 44b). Thus, the charge layers in the southeastern portion of the storm did not extend horizontally across that whole area.

West of the BWLR, where the VHF source density maximum and small flash footprints were seen in the gridded data, the updraft core was adjacent to weak downdrafts, thereby creating a strong horizontal gradient in vertical velocities. These

84

kinematic features were the cause of the largely vertical flash structures and the vertical stack of multiple layers in this part of the storm. The negative sloping of charge layers to the south of the BWLR was caused by the weaker updraft values, which would still support charge separation but would not separate charge in the same vertical levels as within the main updraft core. Graupel maxima and some ice crystals and water content existed throughout much of the vertical extent of the updraft region, which suggests that the same form of non-inductive charging described for the previous two analysis times was still at work in this region at 00:00.

Weak updrafts pervaded the region of large flash densities to the north and northeast of the BWLR at 00:00 UTC. The fact that flash structures were more complex and flash footprint sizes varied more than observed previously in this region (from which more complex charge structure was inferred to exist at 00:00) probably was caused at least in part by the larger horizontal gradients in updraft speeds observed north of the BWLR at this time. Due north of the BWLR, where updraft gradients were largest, the dominant flash structures were vertical and tortuous. Farther east, where vertical velocities were weak but flash densities were largest, large, horizontally extensive flashes were dominant. Small ice crystal and cloud water mixing ratios were present at 9.2 km throughout the region north and northeast of the storm. Graupel mixing ratios tended to be larger where there were smaller, more vertical flashes, while graupel content was rather small where there were larger, more horizontal flashes. As in the earlier analysis times, the horizontal winds through the mid and upper levels of the storm suggest that some charge was advected from west to east in the vicinity of the

BWLR and updraft, which at least partially accounts for the more laminar structure east of regions of significant vertical winds.

3.3 Anvil lightning and secondary convection in the anvil

Once the Kingfisher storm began intensifying after 23:00 UTC, there were several instances of anvil flashes. Here we define anvil flashes as flashes that begin or propagate more than 30 km downshear of the 30 dBZ contour of a storm, as done by Kuhlman et al. (2009). Instances of cloud-to-ground strikes resulting from anvil flashes have been documented (e.g., Kuhlman et al. 2009, Weiss et al. 2012), and they pose a great danger to the general public given a false believe they are safe from lightning at a distance of 30-100 km from a storm's rainfall. The Kingfisher storm produced copious anvil lightning within the range of the 3-D OK LMA and the KTLX radar, which provided the data for the analysis in this section. Additionally, at least 6 of these flashes appeared to be related to the onset and development of secondary convection within the anvil of the Kingfisher storm. The study of these anvil flashes and the anvil convection is confined to 23:00-23:50 UTC.

The first anvil flash to occur during the Kingfisher storm's lifetime was initiated at 23:12:07 UTC near the southeast edge of the cell. It propagated 47 km eastward at an altitude of approximately 7 km. At 23:12:11, the WDSS-II cluster tracking and identification algorithm (w2segmotionll) detected convection initiation (CI) at the location to which the flash propagated. At this time at the lowest radar tilt (0.5^o), the detected convection was visible only as the southernmost tip of a thin line of very weak (~18 dBZ) reflectivity (Fig. 45a). Reflectivity values >18 dBZ were visible in the thin line at the 1.80^o tilt. A vertical cross section of the KTLX reflectivity data from the

23:11:15 volume scan revealed a layer of 18-30 dBZ reflectivity 4-5 km in depth and extending horizontally ~ 75 km through the anvil of the Kingfisher storm (Fig. 45b). At the location of CI detected by WDSS-II in the anvil, there was a downward bulge in the ≥18 dBZ reflectivity contour. The lower bound of the anvil reflectivity signature was 7 km near the parent storm, but descended in a slight bulge to 5 km where CI was detected, and then rose again to 7 km east of that location.

Five subsequent anvil flashes behaved similarly to the first in that they were initiated in the same region of the storm and propagated along roughly the same path in the anvil. The second was initiated at 23:23:26 and propagated at an altitude of 9 km. Its path was the most curved of the six, and it began farthest north, but it still reached over 40 km into the anvil and propagated to approximately the same end point as its predecessor. The third anvil flash was initiated at 23:24:38 and propagated from an altitude of 7 km down to 5 km over a distance of 45 km. Its end point was more distant than the first and second flashes, but it still made contact with the southern tip of the line of developing convection in the anvil. The fourth anvil flash, which was initiated at 23:34:27, was almost 60 km in length and began about 20 km ESE of the parent storm's 30 dBZ echo. The fourth flash also propagated eastward into the anvil convection, but its structure in the anvil had two distinct layers whereas the previous anvil flashes had only one. One layer was along the lowest edge of the anvil reflectivity (~ 5 km) and one was along the upper edge (~ 12 km), but they were connected through a vertical channel at the flash initiation point. The fifth flash was initiated at 23:40:12 and propagated over 50 km eastward to connect with the anvil convection. The final flash examined in detail in this study (and the first to occur after a flash was initiated well within the anvil)
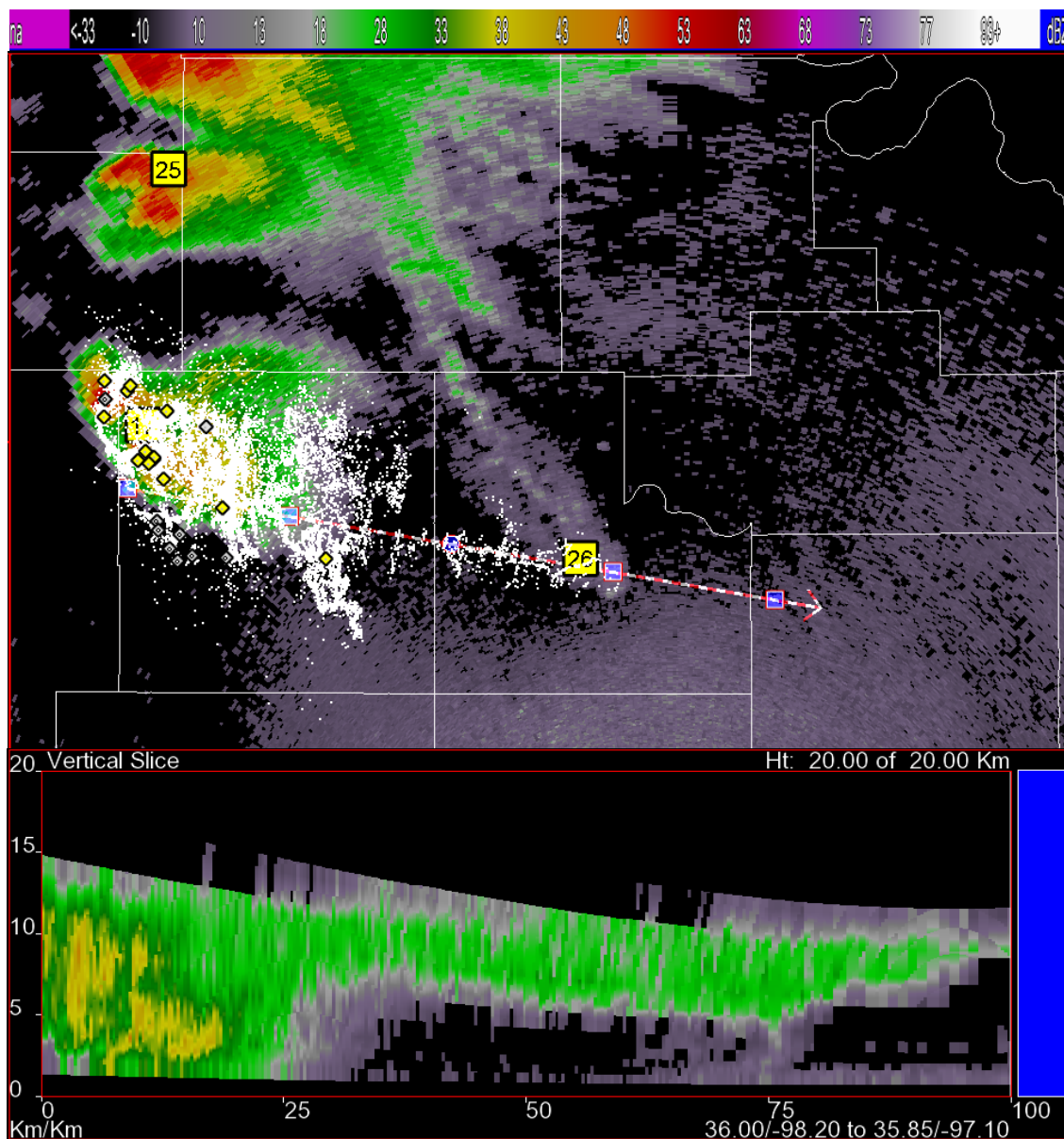
Figure 45. a) (above) A snapshot of the Kingfisher storm's KTLX reflectivity, flash initiation points (diamonds), convection detected by WDSS-II (yellow numbered squares), and VHF source points (white dots) at the time of the first anvil flash (which occurred at 23:12:07—reflectivity image is behind by about a minute). The vector drawn from the Kingfisher storm through the anvil convection denotes the location of the vertical cross section of reflectivity shown in (b) (below).

occurred at 23:47:33 and had two layers as in the fourth flash, though its lower layer propagated near 8 km in altitude rather than 5 km. Anvil flashes continued to be initiated in the parent storm, but they are not documented here because the focus of this analysis is the developmental stage of the secondary convection and the lightning it produced, which will now be discussed.

A few pixels of reflectivity greater than 18 dBZ at the 0.5 degree tilt were visible in the long, thin line of very low reflectivity beginning at 23:15:33 UTC, but more substantial precipitation did not develop within the anvil convection until after 23:30 UTC. By 23:37:02 UTC, the band of precipitation had grown to include reflectivity > 40 dBZ in several places. At 23:41:16, this band of convection initiated a lightning flash locally for the first time, and the flash had extensive horizontal structure along the line in the anvil (see Figs. 46, 47b). The anvil convection continued to strengthen while initiating its own lightning, and soon became fully independent of the Kingfisher storm as it propagated eastward out of the anvil.

From the structure of the anvil flashes initiated within the anvil, a layer of negative charge was inferred at ~ 5-8 km, a layer of positive charge was inferred at ~ 10-12 km, and a layer of negative charge was inferred just above the positive charge (Fig. 47a). Note that the altitude of charge layers inferred from the first flash initiated by the secondary anvil convection (depicted in Fig. 47b) approximately match those initiated near the parent storm, except that the flash initiated in the secondary convection also includes an upper negative layer. However, the polarity of layers indicated by the anvil flash which occurred at 23:34 UTC (Fig. 47a) were opposite to
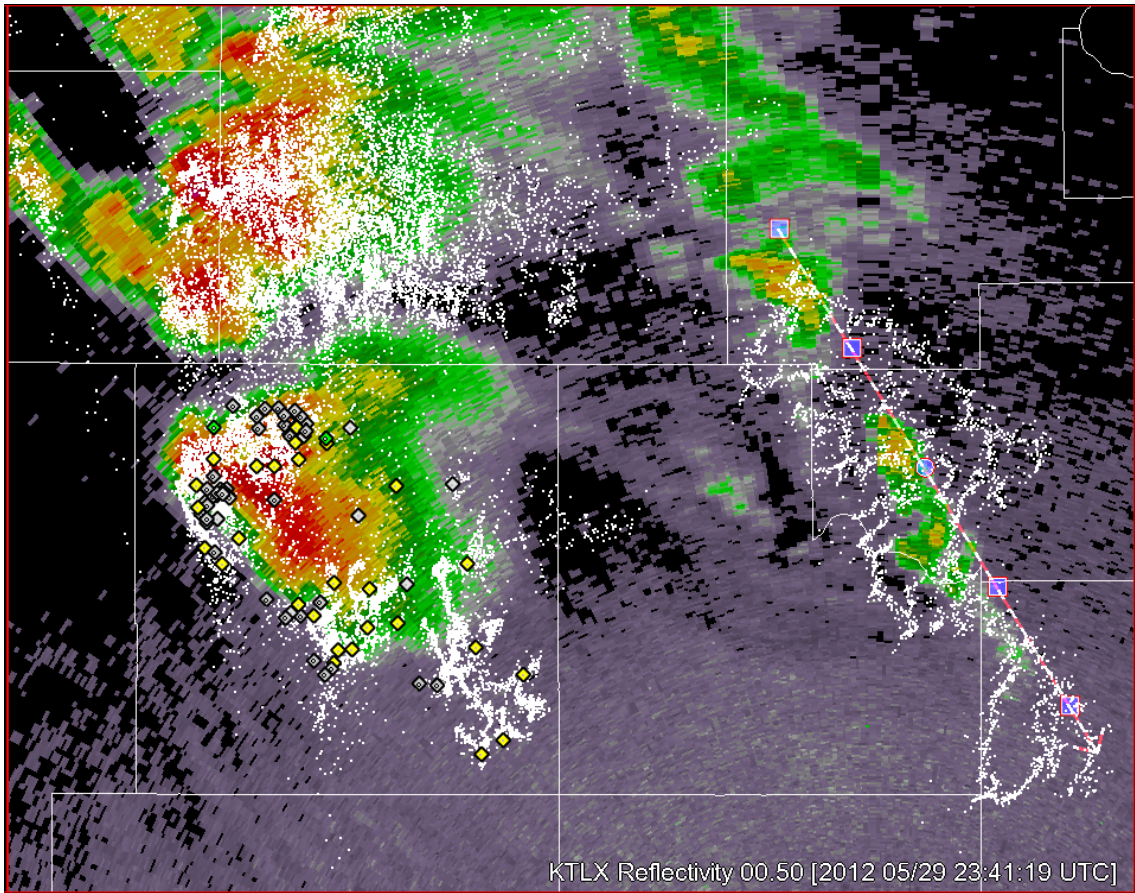
Figure 46. A snapshot of the Kingfisher storm's KTLX reflectivity, flash initiation points (diamonds) and VHF source points (white dots) at the time of the first flash produced by the secondary anvil convection. The vertical cross section indicated by the vector is not shown.

the polarity of corresponding layers of charge for flashes contained within the

east/southeastern region of the storm.

Past studies (Dye and Willett 2007; Marshall et al. 1989) have found substantial

electric fields in anvils, consistent with the existence of lightning there. Byrne et al.

(1989), Dye et al. (2007), Kuhlman et al. (2009), and Weiss et al. (2012) suggest that

from the charge in anvils probably results from some combination of charge advection

the main storm, local charge generation, and macroscopic separation of the charge

reservoir via differential sedimentation within the storm. Although the horizontal winds
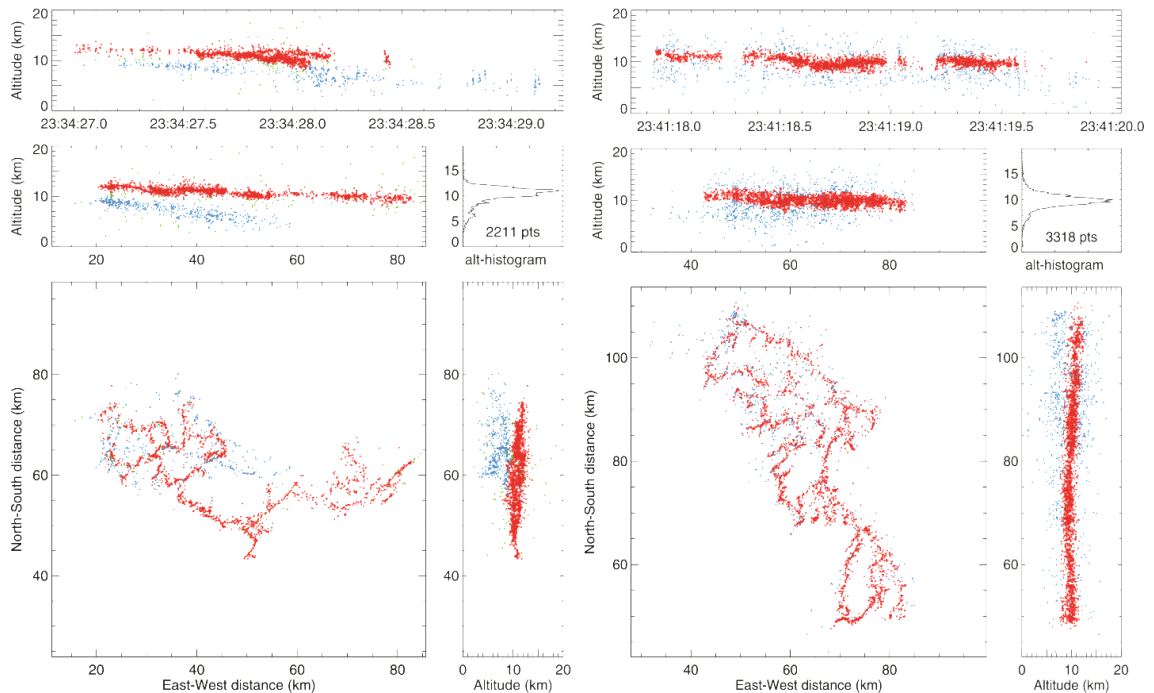
Figure 47. Charge analysis of anvil flashes, a) one propagating east from the parent storm to the secondary anvil convection, and b) the first flash produced by the secondary anvil convection, propagating north to south. Red points indicate where positive charge was inferred and blue points indicate where negative charge was inferred; green points are undetermined.

and the altitude of charge layers in the anvil support this and both sources probably apply to some regions of the anvil, the incongruity in the polarity of charge in corresponding layers from flashes in some adjacent regions suggests that the charge in at least part of the anvil likely was the result of localized charging mechanisms combined with differential sedimentation effects.

The development of secondary convection associated with a downward descending reflectivity feature in the anvil suggests that some local updrafts developed by the Findeisen-Knight CI mechanism described by Knight et al. (2004), in which the mid-level cooling from sublimation and melting as the precipitation descended amplifies and leads to release of local convective instability. It is hypothesized that the resulting localized updrafts and ice content were sufficient to produce strong

91

noninductive charging. Though the DLA domain was west of the secondary convection and it cannot be stated at this time whether or not mixed-phase hydrometeor contents existed in the anvil, it is noted that even very low cloud water content would be sufficient to initiate noninductive charging given presence of a mixture of variably-sized ice particles (e.g., Takahashi 1978). Since the KTLX reflectivity signature descended almost as low as the melting level and since CI leads to convective updrafts sufficiently strong to form and loft hydrometeors, it is not unreasonable to hypothesize that there was some liquid water content enabling noninductive charging in the anvil cloud. It is also possible that some inductive charging occurred in the descending precipitation beneath the anvil, or that charge was contributed from the formation of screening layers at the cloud boundaries.

Chapter 4: Conclusions and Future Work

The well-sampled 29-30 May 2012 Kingfisher supercell provided the unique opportunity to analyze and study the interrelationships between its kinematic, microphysical, and lightning structure. The overall growth to very large sustained total flash rates in this storm (maximizing at nearly 500 min^{-1}) related well to the increasing overall intensity of the storm. Total flash rates increased concurrently with increasing updraft strength. Maxima in flash density tended to be just outside the strongest updraft cores, as expected, but maxima in VHF source density, which is much easier to process in real time, also indicated some regions of updraft, and increases in source density and in the height of VHF sources were often associated with the growth of updrafts. Furthermore, time-height plots of VHF source density depicted elevated bursts of VHF sources in the overshooting top that were indicative of updraft pulses lofting charged particles above the equilibrium level. Variations in the 95th percentile height of VHF sources also were related to the formation and dissipation of updraft pulses and of the variations in the maximum height of various reflectivity values.

These lightning parameters may be useful to supplement radar data and help forecasters diagnose cycles of updraft intensification and dissipation. Horizontal plots of VHF source density are already available in the WDSS-II platform used to develop applications for National Weather Service. Furthermore, the lightning jump algorithm developed by Schultz et al (2009) to identify increasing severe weather probabilities by using criteria for increasing flash rates is being tested with some later refinements to determine how well it performs in a broad range of storm types and locations. Because these algorithms are not concerned with the height of lightning, they are being

93

examined for possible use with optical detections of lightning from the Geosynchronous Lightning Mapper planned for launch on the GOES-R weather satellite (e.g., Schultz et al. 2011; Stano et al. 2014). In the Kingfisher storm, incidents of severe hail reports were well-represented by sudden increases in total flash rates. Although lightning jumps preceded the tornado produced by the Kingfisher storm by ~10 minutes, the jump was related to interactions that occurred during merger with another supercell storm, rather than being related to the intensifying updrafts envisioned in the conceptual model for the lightning jumps.

In regions with coverage by mapping systems that included lightning height information, it would be possible similarly to produce time-height plots of storms or cells to supplement the information about updraft evolution that can be inferred from radar, although no such algorithms are available yet for use in operations in real time. One reason is that three-dimensional total lightning mapping data are available in only select regions. Note, too, that a major problem in automatically producing tendencies in all kinds of storm properties is the difficulty in tracking particular cells or storms from one period to another in real time.

CG lightning flash rates were not related as well as total flash rates to changes in updraft intensity and to increasing probability of severe hail reports. However, the potential relationships between CG flash rates and storm merger processes will be a subject of future work, as CG flash rates did increase markedly as the two supercell storms merged. Unfortunately, the merger process took place after most of the mobile radars had ceased scanning, and the geometric distribution of the remaining mobile radars with respect to KTLX and to the two supercell storms was not conducive to

multi-Doppler analysis. However, more research will be performed on the Kingfisher storm in the near future. One study planned for the near future is a comparison of the DLA hydrometeor mixing ratios against the inferences of hydrometeor classification schemes based on the data of two polarimetric radars. Additionally, the DLA variable fields may be spatially interpolated to the initiation and source locations of individual and cumulative lightning flashes to provide detailed microphysical context for helping interpret both bulk lightning physics and inferred leader polarities. Analysis of polarimetric data will also be extended from the early portion of the storm's lifetime to the merger process.

The distribution of negative and positive CG flashes observed in the Kingfisher storm provided an initial indication that the storm's charge structure was complex and variable in space and time, an observation examined in much more depth by analyzing the in-cloud structure of several flashes. This analysis showed that the inferred charge layers varied in altitude, depth, and polarity from one region to another across the storm. Such variations included the ascent and descent of charge layers in the presence of updrafts and downdrafts, as well as adjacent regions of charge having opposite polarities at the same altitude. Within the updraft, the inferred pockets of charge were small in horizontal extent, which resulted in more vertically extensive flashes than those farther from the updraft core. Some charge advection from the updraft region to the region north–northeast of the updraft and BWLR probably was what caused similar flash structures to be observed there at the later DLA analysis times, in spite of a lack of strong updrafts and/or downdrafts in that region. Because the triple-Doppler and Lagrangian analyses indicated this region was kinematically and microphysically so

different from the region in and near the updraft that it seems unlikely the charge

structures would have been so similar without being strongly driven by advection, and

the horizontal winds appeared suitable for advecting the charge.

The hydrometeor types diagnosed by the DLA across the Kingfisher storm were

suitable for electrifying the storm by the non-inductive mechanism. Note, however, that

maxima in diagnosed mixing ratios for graupel, cloud ice, and supercooled water

occurred in different regions and, therefore, likely produced differing amounts of charge

and even different polarities from one region to another. The BWLR, which persisted

for almost 2 hours, appeared to be caused by a combination of three factors: (1) wet hail

growth (as inferred from the presence of high graupel and cloud water mixing ratios in

the BWLR), which inhibits the separation of charge during rebounding particle

collisions, (2) centrifuging of charged particles out of that area by the mesocyclone, and

(3) the very short time allowed by the very large updraft speeds for charge exchange

and for macroscale separation of oppositely charged particles by sedimentation and

wind shear.

The source of anvil charge likely included a local contribution, as has been

noted by studies of other storms, and in at least some regions, the local contribution

appears to dominate, because the vertical distribution of charge observed in the storm

core was inconsistent with the charge structure observed in adjoining parts of the anvil.

Furthermore, the initiation and intensification of convection within the anvil indicates

that there were sufficient updrafts to produce electrification, most likely by non-

inductive charging, in that part of the storm. The tendency of many anvil flashes to

propagate near the boundaries of the anvil reflectivity echoes suggests that there may

also have been one or more screening charge layers caused by the discontinuity in electrical conductivity across cloud boundaries.

The relationships found between mean flash sizes and storm kinematics include that small, tortuous flashes (greater tortuosity being inferred from the large density of VHF sources) were observed where updrafts and horizontal wind shear were relatively strong, whereas flashes were large and horizontally extensive where updrafts were weak or absent. The regions containing flashes having the smallest horizontal extent also tended to have the highest concentration of flash initiations. The mean flash footprints observed in the updraft region at the 23:21 UTC analysis time were generally larger than those observed at the 23:39 UTC time, and the mean flash footprints observed in the updraft region at the 23:39 UTC analysis time were generally larger than those observed at the 00:00 UTC analysis time. Additionally, at each time, smaller flashes were typically observed in the presence of high graupel mixing ratios, while larger flashes typically occurred where ice crystal mixing ratios were much larger than graupel mixing ratios. Mean flash sizes in regions of the storm with a mixture of particle types and weak horizontal shear in the vertical wind could vary considerably from one small group of grid cells to the next. Overall, the flash footprints grew smaller with time.

As previously stated, future work on this case will involve a dual-polarimetric analysis of the storm from the time this analysis began through the time the merger process was completed and the merged storm began dissipating. One goal is a detailed analysis of the merger process. Furthermore, most of the same analyses performed on the Kingfisher will be performed on three to five more cases from DC3 as part of the author's Ph.D dissertation, the overall objective being to examine the impact of

different storm morphologies (especially differences in the characteristics of updrafts

and microphysics) on storm electrification and lightning properties.

References

Biggerstaff, M. I., and Coauthors, 2005: The Shared Mobile Atmospheric Research and Teaching Radar: A Collaboration to Enhance Research and Teaching. *Bull. Am. Meteorol. Soc.*, **86**, 1263–1274, doi:10.1175/BAMS-86-9-1263. http://dx.doi.org/10.1175/BAMS-86-9-1263.

Boccippio, D. J., K. L. Cummins, H. J. Christian, and S. J. Goodman, 2001: Combined Satellite- and Surface-Based Estimation of the Intracloud–Cloud-to-Ground Lightning Ratio over the Continental United States. *Mon. Wea. Rev.*, **129**, 108–122, doi:10.1175/1520-0493(2001)129<0108:CSASBE>2.0.CO;2. http://dx.doi.org/10.1175/1520-0493(2001)129<0108:CSASBE>2.0.CO.

Bruning, E. C., and D. R. MacGorman, 2013: Theory and Observations of Controls on Lightning Flash Size Spectra. *J. Atmos. Sci.*, **70**, 4012–4029, doi:10.1175/JAS-D-12-0289.1. http://dx.doi.org/10.1175/JAS-D-12-0289.1.

——, 2012: The West Texas LMA. *GLM Science Team Meeting*, Huntsville, AL.

——, W. D. Rust, T. J. Schuur, D. R. MacGorman, P. R. Krehbiel, and W. Rison, 2007: Electrical and Polarimetric Radar Observations of a Multicell Storm in TELEX. *Mon. Wea. Rev.*, **135**, 2525–2544, doi:10.1175/MWR3421.1. http://dx.doi.org/10.1175/MWR3421.1.

——, ——, D. R. MacGorman, M. I. Biggerstaff, and T. J. Schuur, 2010: Formation of Charge Structures in a Supercell. *Mon. Wea. Rev.*, **138**, 3740–3761, doi:10.1175/2010MWR3160.1. http://dx.doi.org/10.1175/2010MWR3160.1.

Bunkers, M. J., M. R. Hjelmfelt, and P. L. Smith, 2006: An Observational Examination of Long-Lived Supercells. Part I: Characteristics, Evolution, and Demise. *Wea. Forecast.*, **21**, 673–688, doi:10.1175/WAF949.1. http://dx.doi.org/10.1175/WAF949.1.

Byrne, G. J., A. A. Few, and M. F. Stewart, 1989: Electric field measurements within a severe thunderstorm anvil. *J. Geophys. Res.*, **94**, 6297–6307.

Calhoun, K. M., D. R. MacGorman, C. L. Ziegler, and M. I. Biggerstaff, 2013: Evolution of Lightning Activity and Storm Charge Relative to Dual-Doppler Analysis of a High-Precipitation Supercell Storm. *Mon. Wea. Rev.*, **141**, 2199–2223, doi:10.1175/MWR-D-12-00258.1. http://dx.doi.org/10.1175/MWR-D-12-00258.1.

Carey, L., and S. Rutledge, 1996: A multiparameter radar case study of the microphysical and kinematic evolution of a lightning producing storm. *Meteorol.*

Atmos. Phys., **59**, 33–64. http://link.springer.com/article/10.1007/BF01032000 (Accessed October 24, 2014).

Crum, T. D., and R. L. Alberty, 1993: The WSR-88D and the WSR-88D Operational Support Facility. *Bull. Am. Meteorol. Soc.*, **74**, 1669–1687, doi:10.1175/1520-0477(1993)074<1669:TWATWO>2.0.CO;2. http://dx.doi.org/10.1175/1520-0477(1993)074<1669:TWATWO>2.0.CO.

Cummins, K. L., and M. J. Murphy, 2009: An Overview of Lightning Locating Systems: History, Techniques, and Data Uses, With an In-Depth Look at the U.S. NLDN. *Electromagn. Compat. IEEE Trans.*, **51**, 499–518, doi:10.1109/TEMC.2009.2023450.

Dye, J. E., and J. C. Willett, 2007: Observed Enhancement of Reflectivity and the Electric Field in Long-Lived Florida Anvils. *Mon. Weather Rev.*, **135**, 3362–3380, doi:10.1175/MWR3484.1. http://dx.doi.org/10.1175/MWR3484.1.

Emersic, C., P. L. Heinselman, D. R. MacGorman, and E. C. Bruning, 2011: Lightning Activity in a Hail-Producing Storm Observed with Phased-Array Radar. *Mon. Weather Rev.*, **139**, 1809–1825, doi:10.1175/2010MWR3574.1. http://dx.doi.org/10.1175/2010MWR3574.1.

Herzog, B. S., 2013: Total lightning information in a 5-year thunderstorm climatology. M.S. thesis, School of Meteorology, The University of Oklahoma, 114 pp.

Kasemir, H. W., 1960: A contribution to the electrostatic theory of a lightning discharge. *J. Geophys. Res.*, **65**, 1873–1878, doi:10.1029/JZ065i007p01873. http://dx.doi.org/10.1029/JZ065i007p01873.

Knight, C. A., L. Jay Miller, and W. D. Hall, 2004: Deep Convection and "First Echoes" within Anvil Precipitation. *Mon. Weather Rev.*, **132**, 1877–1890, doi:10.1175/1520-0493(2004)132<1877:DCAFEW>2.0.CO;2. http://dx.doi.org/10.1175/1520-0493(2004)132<1877:DCAFEW>2.0.CO.

Krehbiel, P. R., R. J. Thomas, W. Rison, T. Hamlin, J. Harlin, and M. Davis, 2000: GPS-based mapping system reveals lightning inside storms. *Eos, Trans. Am. Geophys. Union*, **81**, 21–25, doi:10.1029/00EO00014. http://dx.doi.org/10.1029/00EO00014.

Kuhlman, K. M., C. L. Ziegler, E. R. Mansell, D. R. MacGorman, and J. M. Straka, 2006: Numerically Simulated Electrification and Lightning of the 29 June 2000 STEPS Supercell Storm. *Mon. Weather Rev.*, **134**, 2734–2757, doi:10.1175/MWR3217.1. http://dx.doi.org/10.1175/MWR3217.1.

——, D. R. MacGorman, M. I. Biggerstaff, and P. R. Krehbiel, 2009: Lightning initiation in the anvils of two supercell storms. *Geophys. Res. Lett.*, **36**, L07802, doi:10.1029/2008GL036650. http://dx.doi.org/10.1029/2008GL036650.

Lakshmanan, V., T. Smith, G. Stumpf, and K. Hondl, 2007: The Warning Decision Support System–Integrated Information. *Weather Forecast.*, **22**, 596–612, doi:10.1175/WAF1009.1. http://dx.doi.org/10.1175/WAF1009.1.

Lang, T. J., and Coauthors, 2004: The Severe Thunderstorm Electrification and Precipitation Study. *Bull. Am. Meteorol. Soc.*, **85**, 1107–1125, doi:10.1175/BAMS-85-8-1107. http://dx.doi.org/10.1175/BAMS-85-8-1107.

Lhermitte, R., and P. R. Krehbeil, 1979: Doppler radar and radio observations of thunderstorms. *IEEE Trans. Geosci. Electron.*, **17**, 162-171.

Lund, N. R., D. R. MacGorman, T. J. Schuur, M. I. Biggerstaff, and W. D. Rust, 2009: Relationships between Lightning Location and Polarimetric Radar Signatures in a Small Mesoscale Convective System. *Mon. Weather Rev.*, **137**, 4151–4170, doi:10.1175/2009MWR2860.1. http://dx.doi.org/10.1175/2009MWR2860.1.

MacGorman, D. R., A. A. Few, and T. L. Teer, 1981: Layered Lightning Activity. *J. Geophys. Res.*, **86**, 9900–9910.

——, J. M. Straka, and C. L. Ziegler, 2001: A Lightning Parameterization for Numerical Cloud Models. *J. Appl. Meteorol.*, **40**, 459–478, doi:10.1175/1520-0450(2001)040<0459:ALPFNC>2.0.CO;2. http://dx.doi.org/10.1175/1520-0450(2001)040<0459:ALPFNC>2.0.CO.

——, W. D. Rust, 1998: *The Electrical Nature of Storms*. Oxford University Press.

——, ——, P. Krehbiel, W. Rison, E. Bruning, and K. Wiens, 2005: The Electrical Structure of Two Supercell Storms during STEPS. *Mon. Weather Rev.*, **133**, 2583–2607, doi:10.1175/MWR2994.1. http://dx.doi.org/10.1175/MWR2994.1.

——, and Coauthors, 2008: TELEX The Thunderstorm Electrification and Lightning Experiment. *Bull. Am. Meteorol. Soc.*, **89**, 997–1013, doi:10.1175/2007BAMS2352.1. http://dx.doi.org/10.1175/2007BAMS2352.1.

——, I. R. Apostolakopoulos, N. R. Lund, N. W. S. Demetriades, M. J. Murphy, and P. R. Krehbiel, 2011: The Timing of Cloud-to-Ground Lightning Relative to Total Lightning Activity. *Mon. Weather Rev.*, **139**, 3871–3886, doi:10.1175/MWR-D-11-00047.1. http://dx.doi.org/10.1175/MWR-D-11-00047.1.

Majcen, M., P. Markowski, Y. Richardson, D. Dowell, and J. Wurman, 2008: Multipass Objective Analyses of Doppler Radar Data. *J. Atmos. Ocean. Technol.*, **25**, 1845–

1858, doi:10.1175/2008JTECHA1089.1.
http://dx.doi.org/10.1175/2008JTECHA1089.1.

Mansell, E. R., D. R. MacGorman, C. L. Ziegler, and J. M. Straka, 2002: Simulated three-dimensional branched lightning in a numerical thunderstorm model. *J. Geophys. Res. Atmos.*, **107**, ACL 2–1–ACL 2–12, doi:10.1029/2000JD000244. http://dx.doi.org/10.1029/2000JD000244.

——, C. L. Ziegler, and E. C. Bruning, 2010: Simulated electrification of a small thunderstorm with two-moment bulk microphysics. *J. Atmos. Sci.*, **67**, 171–194, doi:10.1175/2009JAS2965.1. http://dx.doi.org/10.1175/2009JAS2965.1.

Markowski, P. M., 2002: Hook Echoes and Rear-Flank Downdrafts: A Review. *Mon. Weather Rev.*, **130**, 852–876, doi:10.1175/1520-0493(2002)130<0852:HEARFD>2.0.CO;2. http://dx.doi.org/10.1175/1520-0493(2002)130<0852:HEARFD>2.0.CO.

Marshall, T. C., and W. D. Rust, 1991: Electric field soundings through thunderstorms. *J. Geophys. Res. Atmos.*, **96**, 22297–22306, doi:10.1029/91JD02486. http://dx.doi.org/10.1029/91JD02486.

——, ——, W. P. Winn, and K. E. Gilbert, 1989: Electrical structure in two thunderstorm anvil clouds. *J. Geophys. Res. Atmos.*, **94**, 2171–2181, doi:10.1029/JD094iD02p02171. http://dx.doi.org/10.1029/JD094iD02p02171.

——, M. P. McCarthy, and W. D. Rust, 1995: Electric field magnitudes and lightning initiation in thunderstorms. *J. Geophys. Res. Atmos.*, **100**, 7097–7103, doi:10.1029/95JD00020. http://dx.doi.org/10.1029/95JD00020.

——, M. Stolzenburg, C. R. Maggio, L. M. Coleman, P. R. Krehbiel, T. Hamlin, R. J. Thomas, and W. Rison, 2005: Observed electric fields associated with lightning initiation. *Geophys. Res. Lett.*, **32**, L03813, doi:10.1029/2004GL021802. http://dx.doi.org/10.1029/2004GL021802.

Mazur, V., 1989: A physical model of lightning initiation on aircraft in thunderstorms. *J. Geophys. Res. Atmos.*, **94**, 3326–3340, doi:10.1029/JD094iD03p03326. http://dx.doi.org/10.1029/JD094iD03p03326.

Oye, R., C. Mueller, and S. Smith, 1995: Software for the radar translation, visualization, editing, and interpolation. Preprints, *27th Conf. on Radar Meteorology*, Vail, CO, Amer. Meteor. Soc., 359-361.

Potvin, C. K., L. J. Wicker, and A. Shapiro, 2012: Assessing Errors in Variational Dual-Doppler Wind Syntheses of Supercell Thunderstorms Observed by Storm-Scale Mobile Radars. *J. Atmos. Ocean. Technol.*, **29**, 1009–1025, doi:10.1175/JTECH-D-11-00177.1. http://dx.doi.org/10.1175/JTECH-D-11-00177.1.

Ray, P. S., K. K. Wagner, K. W. Johnson, J. J. Stephens, W. C. Bumgarner, and E. A. Mueller, 1978: Triple-Doppler observations of a convective storm. *J. Appl. Meteor.*, **17**, 1201–1212.

——, D. R. Macgorman, W. D. Rust, W. L. Taylor, and L. W. Rasmussen, 1987: Lightning location relative to storm structure in a supercell storm and a multicell storm. *J. Geophys. Res. Atmos.*, **92**, 5713–5724, doi:10.1029/JD092iD05p05713. http://dx.doi.org/10.1029/JD092iD05p05713.

Rison, W., R. J. Thomas, P. R. Krehbiel, T. Hamlin, and J. Harlin, 1999: A GPS-based three-dimensional lightning mapping system: Initial observations in central New Mexico. *Geophys. Res. Lett.*, **26**, 3573–3576, doi:10.1029/1999GL010856. http://dx.doi.org/10.1029/1999GL010856.

Rust, W. D., and D. R. MacGorman, 2002: Possibly inverted-polarity electrical structures in thunderstorms during STEPS. *Geophys. Res. Lett.*, **29**, 12–13, doi:10.1029/2001GL014303. http://dx.doi.org/10.1029/2001GL014303.

Sasaki, Y., 1970: Some basic formalisms in numerical variational analysis. *Mon. Wea. Rev.*, **98**, 875–883, doi:10.1175/1520-0493(1970)098<0875:SBFINV>2.3.CO;2. http://dx.doi.org/10.1175/1520-0493(1970)098<0875:SBFINV>2.3.CO.

Saunders, C. P. R., 1993: A Review of Thunderstorm Electrification Processes. *J. Appl. Meteorol.*, **32**, 642–655, doi:10.1175/1520-0450(1993)032<0642:AROTEP>2.0.CO;2. http://dx.doi.org/10.1175/1520-0450(1993)032<0642:AROTEP>2.0.CO.

——, H. Bax-norman, C. Emersic, E. E. Avila, and N. E. Castellano, 2006: Laboratory studies of the effect of cloud conditions on graupel/crystal charge transfer in thunderstorm electrification. *Q. J. R. Meteorol. Soc.*, **132**, 2653–2673, doi:10.1256/qj.05.218. http://dx.doi.org/10.1256/qj.05.218.

Schultz, C. J., W. A. Petersen, and L. D. Carey, 2009: Preliminary Development and Evaluation of Lightning Jump Algorithms for the Real-Time Detection of Severe Weather. *J. Appl. Meteorol. Climatol.*, **48**, 2543–2563, doi:10.1175/2009JAMC2237.1. http://dx.doi.org/10.1175/2009JAMC2237.1.

——, ——, and ——, 2011: Lightning and Severe Weather: A Comparison between Total and Cloud-to-Ground Lightning Trends. *Wea. Forecast.*, **26**, 744–755, doi:10.1175/WAF-D-10-05026.1. http://dx.doi.org/10.1175/WAF-D-10-05026.1.

Simpson, G., and F. J. Scrase, 1937: The distribution of electricity in thunderclouds. *Proc. Roy. Soc. Lond.*, *A*, **161**, 309-352, doi:10.2307/96788, Article Type: research-article / Full publication date: Aug. 3, 1937 / Copyright © 1937 The Royal Society.

——, and G. D. Robinson, 1941: The distribution of electricity in thunderclouds, II. *Proc. Roy. Soc. Lond.*, *A*, **177**, 281-329, doi:10.2307/97591, Article Type: research-article / Full publication date: Feb. 24, 1941 / Copyright © 1941 The Royal Society.

Stano, G. T., C. J. Schultz, L. D. Carey, D. R. MacGorman, and K. M. Calhoun, 2014: Total lightning observations and tools for the 20 May 2013 Moore, Oklahoma, tornadic supercell. *J. Operational Meteor.*, **2** (7), 71–88.

Steiger, S. M., R. E. Orville, and L. D. Carey, 2007: Total Lightning Signatures of Thunderstorm Intensity over North Texas. Part I: Supercells. *Mon. Weather Rev.*, **135**, 3281–3302, doi:10.1175/MWR3472.1. http://dx.doi.org/10.1175/MWR3472.1.

Stolzenburg, M., W. D. Rust, and T. C. Marshall, 1998: Electrical structure in thunderstorm convective regions: 3. Synthesis. *J. Geophys. Res. Atmos.*, **103**, 14097–14108, doi:10.1029/97JD03545. http://dx.doi.org/10.1029/97JD03545.

——, and T. C. Marshall, 1994: Testing models of thunderstorm charge distributions with Coulomb's law. *J. Geophys. Res. Atmos.*, **99**, 25921–25932, doi:10.1029/94JD02332. http://dx.doi.org/10.1029/94JD02332.

Takahashi, T., 1978: Riming Electrification as a Charge Generation Mechanism in Thunderstorms. *J. Atmos. Sci.*, **35**, 1536–1548, doi:10.1175/1520-0469(1978)035<1536:REAACG>2.0.CO;2. http://dx.doi.org/10.1175/1520-0469(1978)035<1536:REAACG>2.0.CO.

——, and K. Miyawaki, 2002: Reexamination of Riming Electrification in a Wind Tunnel. *J. Atmos. Sci.*, **59**, 1018–1025, doi:10.1175/1520-0469(2002)059<1018:ROREIA>2.0.CO;2. http://dx.doi.org/10.1175/1520-0469(2002)059<1018:ROREIA>2.0.CO.

Tessendorf, S. A., S. A. Rutledge, and K. C. Wiens, 2007a: Radar and Lightning Observations of Normal and Inverted Polarity Multicellular Storms from STEPS. *Mon. Weather Rev.*, **135**, 3682–3706, doi:10.1175/2007MWR1954.1. http://dx.doi.org/10.1175/2007MWR1954.1.

——, K. C. Wiens, and S. A. Rutledge, 2007b: Radar and Lightning Observations of the 3 June 2000 Electrically Inverted Storm from STEPS. *Mon. Weather Rev.*, **135**, 3665–3681, doi:10.1175/2006MWR1953.1. http://dx.doi.org/10.1175/2006MWR1953.1.

Testud, J., E. Le Bouar, E. Obligis, and M. Ali-Mehenni, 2000: The Rain Profiling Algorithm Applied to Polarimetric Weather Radar. *J. Atmos. Ocean. Technol.*, **17**, 332–356, doi:10.1175/1520-0426(2000)017<0332:TRPAAT>2.0.CO;2. http://dx.doi.org/10.1175/1520-0426(2000)017<0332:TRPAAT>2.0.CO.

Thomas, R. J., P. R. Krehbiel, W. Rison, S. J. Hunyady, W. P. Winn, T. Hamlin, and J. Harlin, 2004: Accuracy of the Lightning Mapping Array. *J. Geophys. Res. Atmos.*, **109**, D14207, doi:10.1029/2004JD004549. http://dx.doi.org/10.1029/2004JD004549.

Vaisala, cited 2014: Technical specifications. http://www.vaisala.com/en/products/thunderstormandlightningdetectionsystems/Pages/NLDN.aspx

Weiss, S. A., W. D. Rust, D. R. MacGorman, E. C. Bruning, and P. R. Krehbiel, 2008: Evolving Complex Electrical Structures of the STEPS 25 June 2000 Multicell Storm. *Mon. Weather Rev.*, **136**, 741–756, doi:10.1175/2007MWR2023.1. http://dx.doi.org/10.1175/2007MWR2023.1.

——, D. R. MacGorman, and K. M. Calhoun, 2012: Lightning in the Anvils of Supercell Thunderstorms. *Mon. Weather Rev.*, **140**, 2064–2079, doi:10.1175/MWR-D-11-00312.1. http://dx.doi.org/10.1175/MWR-D-11-00312.1.

Wiens, K. C., S. A. Rutledge, and S. A. Tessendorf, 2005: The 29 June 2000 Supercell Observed during STEPS. Part II: Lightning and Charge Structure. *J. Atmos. Sci.*, **62**, 4151–4177, doi:10.1175/JAS3615.1. http://dx.doi.org/10.1175/JAS3615.1.

Williams, E. R., 1989: The tripole structure of thunderstorms. *J. Geophys. Res. Atmos.*, **94**, 13151–13167, doi:10.1029/JD094iD11p13151. http://dx.doi.org/10.1029/JD094iD11p13151.

Wilson, C. T. R., 1916: On some determinations of the sign and magnitude of electric discharges in lightning flashes. *Proc. Roy. Soc. Lond., A*, **92**, 555-574.

——, 1925: The electric field of a thundercloud and some of its effects. *Proc. Roy. Soc. Lond., A*, **37**, 32D, doi:10.1088/1478/37/1/314.

Ziegler, C. L., and D. R. MacGorman, 1994: Observed lightning morphology relative to modeled space charge and electric field distributions in a tornadic storm. *J. Atmos. Sci.*, **51**, 833–851.

——, 2013a: A diabatic Lagrangian technique for the analysis of convective storms. Part I: Description and validation via an Observing System Simulation Experiment. *J. Atmos. Ocean. Technol.*, **30**, 2248–2265, doi:10.1175/JTECH-D-12-00194.1. http://dx.doi.org/10.1175/JTECH-D-12-00194.1.

——, 2013b: A diabatic Lagrangian technique for the analysis of convective storms. Part II: Application to a radar-observed storm. *J. Atmos. Ocean. Technol.*, **30**, 2266–2280, doi:10.1175/JTECH-D-13-00036.1. http://dx.doi.org/10.1175/JTECH-D-13-00036.1.

——, E. R. Mansell, K. M. Calhoun, and D. R. MacGorman, 2014: Impact of
    kinematics, microphysics, and electrification on the formation of lightning-weak
    holes in a simulated supercell storm. *Preprints*, XVth Intl. Conf. on Atmos. Elec.,
    Norman, OK, 16 pp.[available at
    http://www.nssl.noaa.gov/users/mansell/icae2014/preprints/Ziegler_324.pdf]